From Surface Science to Heterogeneous Catalysis: Insights from First Principles Modeling

By
Carrie A. Farberow

A dissertation submitted in partial fulfillment of
the requirements for the degree of

Doctor of Philosophy
(Chemical Engineering)

at the
University of Wisconsin-Madison
2014

Date of final oral examination: July 30, 2014

The dissertation is approved by the following members of the Final Oral Committee:
Manos Mavrikakis, Professor, Chemical & Biological Engineering
James A. Dumesic, Professor, Chemical & Biological Engineering
George W. Huber, Professor, Chemical & Biological Engineering
Christos T. Maravelias, Associate Professor, Chemical & Biological Engineering
Izabela Szlufarska, Associate Professor, Materials Science & Engineering

From Surface Science to Heterogeneous Catalysis: Insights from First Principles Modeling

Carrie A. Farberow

Under the supervision of Prof. Manos Mavrikakis and Prof. James A. Dumesic
at the University of Wisconsin–Madison

The design of improved heterogeneous catalysts requires a detailed understanding of the governing surface chemistry. Significant advances over the past two decades in electronic structure calculation algorithms and high performance computing have made theoretical tools indispensable in the quest to understand catalysis at the atomic scale. In this dissertation, first principles electronic structure calculations based on density functional theory (DFT) and microkinetic modeling are combined with experimental studies, including surface science, electrocatalysis and reaction kinetics, to elucidate reaction mechanisms and design improved catalysts for a variety of reactions important to energy and environmental applications.

Chapters 3 and 4 of this dissertation focus on the fundamental end of the catalysis research spectrum. In this work, experimental surface science studies, using high-resolution, high-speed scanning tunneling microscopy are combined with periodic, self-consistent DFT calculations to improve our understanding of two important processes, hydrogen diffusion and water adsorption, on a metal oxide thin film. In Chapter 5, first principles calculations are utilized to study the vapor phase reaction between hydrogen and oxygen on a homogeneous bimetallic PdAg alloy surface.

A successful example of catalyst design for an electrocatalytic application is demonstrated in Chapter 6 using a combined theoretical and experimental approach. A core-shell alloy, composed of an Ir-Re core and Pt and Pd shell layers, is shown to be an effective low cost electocatalyst for the oxygen reduction reaction. Finally, in Chapters 7 and 8 of this dissertation, DFT calculations are combined with experimental reaction kinetic studies using a microkinetic model to bridge the pressure and materials gap, in a study of nitric oxide reduction by hydrogen on a platinum catalyst. In this work, we show the impact of nitric oxide surface coverage on the reaction energetics and elucidate the reaction pathways governing the activity and selectivity of the reaction on Pt under realistic reaction conditions.

Acknowledgements

First, I would like to express my gratitude to my advisors Prof. James Dumesic and Prof. Manos Mavrikakis. I have greatly benefited from their technical expertise and professional guidance throughout my studies and will carry what I have learned from them with me throughout my career. Their enthusiasm for solving challenging and interesting research problems has been contagious and motivated the persistence requisite for successful academic research. I thank Prof. George Huber, Prof. Christos Maravelias, and Prof. Izabela Szulfarska for serving on my PhD defense committee and Prof. Tom Kuech and Prof. John Yin for serving on my preliminary exam committee.

I would also like to thank all of the members, both past and present, of the Dumesic and Mavrikakis research groups for enhancing my education as teachers and my morale as friends. Because of the wonderful undergraduate students, graduate students and post-docs I have been surrounded with, my days at "work" rarely felt like work. In particular, I benefited from fruitful collaborations and scientific discussions with Dr. Guowen Peng, Brandon O'Neill, Tom Schwartz and Yunhai Bai. I appreciate the prompt and detailed responses to my many e-mailed questions and various friendly interactions with Prof. Jeff Greeley (Purdue University) and Prof. Ye Xu (Louisiana State University). I am grateful to have had Prof. Lars Grabow (University of Houston) as a collaborator, mentor and friend.

I am appreciative of the opportunity, afforded to me by Prof. Jens Nørskov and the NSF – Partnerships for International Research and Education program, to study for a summer at the Center for Atomic Scale Materials Deign at the Technical University of Denmark. The technical

support from Todd Ninman, Mary Heimbecker, Eric Codner and Joel Lord in various capacities has been incredibly helpful and I thank all of the staff in the Department of Chemical & Biological Engineering. In particular, I greatly appreciate the administrative support, friendly conversations and delicious baked goods provided by Judy Lewison

Much of the research presented in this dissertation resulted from collaborations with exceptional scientists and engineers at external institutions including Andres Godinez-Garcia, Dr. Juan Francisco Perez-Robles, Dr. Omar Solorza-Feria (Cinvestav-IPN), Dr. Radoslav Adzic, Dr. Kotaro Sasaki, Dr. Kurian Kuttiyiel (Brookhaven National Laboratory), Prof. Hiroko Karan (Medgar Evers College), Prof. Flemming Besenbacher, Dr. Lindsay Merte, Prof. Erik Lægsgaard**,** Ralf Bechstein, Felix Rieboldt, Jan Knudsen, Helene Zeuthen, Wilhelmine Kudernatsch, and Stefan Wendt (Aarhus University). I acknowledge funding from the Department of Energy, Basic Energy Sciences and a graduate research fellowship from the National Science Foundation. Supercomputing time used at the following institutions is also gratefully acknowledged: National Energy Research Scientific Computing Center, Pacific Northwest National Laboratory, Oak Ridge National Laboratory, and Argonne National Laboratory.

I am certain that I would not have embarked on this journey if not for the education and encouragement I received from many of the teachers I encountered prior to graduate school. In particular, I want to thank Jackie Schornick, my high school AP chemistry teacher who made the challenges of chemistry interesting and fun thereby piquing my interest in the subject. I am a proud graduate of the Chemical, Biological and Materials Engineering Department at the

University of Oklahoma, and am grateful for the education and mentoring provided by Prof. Lance Lobban and many other professors in the department there.

I am lucky to have a handful of truly invaluable friendships for which I am profoundly grateful. Tackling graduate school course work was much less painful working with Joe Samaniuk and it was a treat to get to know Madison and its many wonderful live music venues together. I am thankful for Erin Henderson, who has supported my academic endeavors as my best friend and editor extraordinaire.

A massive thank you to Stephen Saye, who has listened to my day-to-day graduate student frustrations, provided essential support and encouragement, and planned and accompanied me on numerous rejuvenating breaks for fun and laughter. Madison has truly felt like home with you and I am elated for everything we have to look forward to in Colorado and beyond. I am grateful to have had the entire Saye family in my corner, cheering me on, particularly throughout the home stretch of this journey.

Lastly, I would like to thank my family. The unconditional love provided by my grandfather, Pap, my parents, Jeff and Kathy, and my sister, Brittney, inspired my confidence to attempt a graduate degree, and furthermore, carried me to its completion. Thank you for your certainty that I could achieve anything I set my mind to and for reminding me of that frequently. My personal and professional successes are thanks to the lessons and learning opportunities you all provided. Lastly, I would like to thank my mother, for being a wonderful example of a strong woman throughout my life and for instilling in me a love for music that has provided a refuge during graduate school's many ups and downs.

Table of Contents

Abstract……..……..i

Acknowledgements……iii

Table of Contents……...vi

List of Figures…….……ix

List of Tables……xvi

Chapter 1 Introduction 1

1.1 Reaction Mechanisms 3

1.2 Catalyst Design 4

1.3 Dissertation Scope 5

Chapter 2 Methods 8

2.1 Theoretical Foundations 8

2.2 Density Functional Theory 9

2.3 Applications of Density Functional Theory to Surface Chemistry 11

2.3.1 Thermochemistry and Binding Energies 12

2.3.2 Vibrational Frequencies 13

2.3.3 Transition State Energies 14

2.3.4 Potential Energy Surfaces 14

Chapter 3 Water-mediated Proton Hopping on an Iron Oxide Surface 16

3.1 Introduction 16

3.2 Methods and Materials 17

3.2.1 Experimental Methods 17

3.2.2 Computational Methods 20

3.3 Results and Discussion 21

3.4 Conclusions 30

Chapter 4 Water Clustering on Nanostructured FeO Films 31

4.1 Introduction 31

4.2 Methods 33

4.3 Results 34

4.3.1 Hydroxylation of FeO with Atomic Hydrogen 34

4.3.2 Effect of Hydroxylation on Water Clustering 36

4.3.3 DFT Calculations of Water Clusters on FeO 41

4.3.4 Desorption Kinetics 48

4.4 Conclusion 52

Chapter 5 Mechanistic Studies of Oxygen Reduction by Hydrogen on PdAg(110) 54

5.1 Introduction 54

5.2 Methods 57

5.3 Results 60
5.3.1 Adsorption of Reactants and Intermediates 60
5.3.2 Elementary Steps 65
5.3.3 Potential Energy Surfaces 72

5.4 Conclusions 83

Chapter 6 Catalytic Activity of Platinum Monolayer on Iridium and Rhenium Alloy Nanoparticles for the Oxygen Reduction Reaction 86

6.1 Introduction 86

6.2 Methods 88
6.2.1 Experimental 88
6.2.2 Catalyst Synthesis and Characterization 90
6.2.3 Density Functional Theory Calculations 91

6.3 Results and Discussion 92
6.3.1 Characterization of Ir-Re Alloy Nanoparticles 92
6.3.2 Pt (Pd) Monolayer Deposition on Ir-Re Nanoparticles 93
6.3.3 Oxygen Reduction 95
6.3.4 Density Functional Theory Calculations 100
6.3.5 Stability of the Catalysts 102

6.4 Conclusions 103

Chapter 7 Density Functional Theory Calculations and Analysis of Reaction Pathways for Reduction of Nitric Oxide by Hydrogen on Pt(111) 105

7.1 Introduction 105

7.2 Methods 106

7.3 Results 109
7.3.1 Nitric Oxide Surface Coverage 109
7.3.2 Adsorption 111
7.3.3 Elementary Steps: Reaction Energies and Activation Energy Barriers 113
7.3.4 Maximum Rate Analysis 124

7.4 Conclusions 141

Chapter 8 Microkinetic Analysis of Nitric Oxide Reduction by Hydrogen on Platinum 143

8.1 Introduction 143

8.2 Methods 144
8.2.1 Density Functional Theory Calculations 144
8.2.2 Experiments 145
8.2.3 Microkinetic Model 146

8.3 Results 150

8.3.1 Optimized Reaction Mechanism on High NO Coverage Pt(111) 151
8.3.2 Alternative Mechanism I: N-O Activation via HNOH* + * → NH* + OH* 158
8.3.3 Alternative Mechanism II: Product Formation via N* 159
8.3.4 Rate Determining and Selectivity Determining Steps 161
8.3.5 On the Nature of the Active Site 163
8.4 Conclusions 164

Chapter 9 References 166

List of Figures

Figure 1.1 Model projected global average surface temperature for a business-as-usual emissions scenario (red) and aggressive emission reductions scenario (blue). Black is the modelled estimate of past warming. Solid lines represent the average of different model runs, and the shaded areas provide a measure of the spread (one standard deviation) between the temperature changes projected by the different models. All data are relative to a reference period (set to zero) of 1986-2005. Figure from National Academy of Sciences.[2] 2

Figure 1.2 Models of the (111) facet of various bimetallic alloy structures. Blue spheres represent a metal, A, and gold spheres represent a different metal, B. 5

Figure 2.1 Schematic flow diagram of the key steps in density functional theory calculations. Adapted from Morgan.[32] 11

Figure 2.2 Potential energy surface (PES) for the reaction $AB_{(g)} \rightarrow A^* + B^*$, in which gas phase AB adsorbs and then dissociates to form the surface adsorbates A* and B*. The activation energy barrier and reaction energy indicated are for the surface reaction AB* → A* + B*. 15

Figure 3.1 (A) An atomically-resolved STM image of the bare FeO film, showing its moiré-structure and protrusions due to individual Fe and O atoms. (B-G) Series of scanning tunneling microscopy (STM) images of the hydrogenated FeO film on Pt(111) at 105 K. The hydrogen atoms (bright spots) diffuse rapidly in the presence of a water molecule which hops from one domain to the next until it leaves the scanning area. The rapid movement of H atoms in the presence of the water molecule manifests itself as irregular streaks in the STM image, marked with circles. (H) The difference image, obtained by subtracting the first image from the last, shows the changes in H atom positions along the path of the water molecule. Scale bars in all images correspond to 2 nm. 22

Figure 3.2 (A) Time-resolved STM measurements of hydrogen atoms on FeO(111)/Pt(111) at room temperature. The first frame shows a single 180×180 Å STM image of the FeO film showing H atoms as bright protrusions. The remaining frames are sequential difference images showing the changes in H atom positions between frames. (B) The hopping rate extracted from a room-temperature STM movie in terms of the number of hopping events observed per frame. (C) Histogram of hopping events from (B) compared with that expected for independent diffusion events. (D) Hopping rate extracted from STM movies acquired at 160 K before and after exposure to a small amount of water. 23

Figure 3.3 Excerpt from a room-temperature STM movie recorded on a 650 × 650 $Å^2$ area of a hydrogenated FeO/Pt(111) thin film. Each frame shown is the difference between two consecutively-acquired STM topographs, and black lines mark the positions of mono-atomic step edges (the steps are 2.25 Å in height, ascending from lower left to upper right) in the Pt(111) substrate. Red/blue pairs in the difference images represent single H atom diffusion events. The collective nature of the diffusion events is clear in these large-scale images. The non-uniformity of the 'swarms' of events is a result of the random

diffusion paths of water molecules on the surface. Note further the tendency of these swarms to avoid crossing step edges. 25

Figure 3.4 Isotope exchange between adsorbed D atoms and dosed H_2O. (A) Example of a TPD measurement where H_2O was dosed onto a D-covered surface. The peaks at 180 K due to HDO (m/z = 19), and D_2O (m/z = 20), in addition to that of H_2O (m/z = 18), arise from proton exchange with the surface. (B) Fraction of each isotopologue and of total deuterium in the desorbing water, from a series of TPD measurements where the sample was re-cooled after each measurement and exposed again to H_2O. Formation of HDO and D_2O depletes the deuterium fraction, which decays exponentially with the number of measurements. 26

Figure 3.5 Energy profile for hydrogen atom diffusion on FeO/Pt(111): H_2O-mediated (blue solid line) and intrinsic (red dashed line); insets provide cross-section views of the initial (IS), transition (TS), and final state (FS) for the H_2O-mediated diffusion 27

Figure 3.6 Energy profile for water diffusion on FeO/Pt(111) with a local H overlayer in a $(\sqrt{3}\times\sqrt{3})R30°$ pattern: (i) $\rightarrow$ (ii) $\rightarrow$ (iii) rotation of the water molecule around the surface OH [see the green curved arrow in inset (i) and (ii)]; (i) $\rightarrow$ (iv) flipping of the H_2O molecule from one OH group to another [see the pink dashed arrow in inset (i)]; corresponding top views of atomic structures are shown by insets (i)—(iv). 29

Figure 4.1 (a) STM image of the bare FeO/Pt(111) film (65 mV, 3 nA). The moiré unit cell and high symmetry domains are indicated. Circle, square, and triangle are used to denote TOP, FCC, and HCP domains respectively. (b) Ball model of the FeO/Pt(111) film. The ~25Å moiré unit cell is indicated as are the three high-symmetry domains. OH groups are shown (with white dots for H atoms) in the preferred FCC domain of the moiré unit cell in their preferred $\sqrt{3}\times\sqrt{3}R30°$ arrangement. (c) STM image (0.7 V, 0.4 nA) of the hydroxylated FeO film with an OH coverage of 0.05 ML, acquired at 160 K after additionally dosing ~0.02 ML water (not visible). (d) Pair correlation function for OH groups showing peaks at the 2^{nd} nearest neighbour and 5^{th} nearest neighbour positions, indicating local $\sqrt{3}\times\sqrt{3}R30°$ ordering. Inset: Distribution of OH groups within the moiré cell, showing the preference for occupation of FCC domains. 36

Figure 4.2 (a) STM image of water adsorbed on the bare FeO/Pt(111) film, acquired at 110 K. The moiré unit cell is indicated in blue and the positions of TOP domains in the vicinity of three H_2O islands are indicated with gray dots. The rectangular area shows enhanced contrast of the bare FeO film, where bright spots are seen corresponding to the TOP domains. The image shows two terraces (higher terrace in the upper right) separated by a single-atomic height step in the Pt(111) substrate. A cyclic colour scale is used to improve contrast. (b) High magnification STM image of a H_2O island on the bare FeO film. This image is the average of four successive STM measurements at 110 K. The grid marks the moiré unit cells, and the different domains are labelled as in Figure 4.1b. Scale bar: 20 Å. (c) The same STM image as in (b) after subtraction of the long-range height variations. Arrows indicate some of the 4-5 Å pores observed in the structure. Scale bar: 20 Å. 38

Figure 4.3 (a) STM image of water adsorbed on a hydroxylated FeO film with an OH coverage of 0.05 ML, acquired at 110 K. The moiré unit cell is indicated in blue. The image shows two terraces (higher terrace in the upper left) separated by a single-atomic height step in the Pt(111) substrate. A cyclic colour scale is used to improve contrast. (b) High-magnification images of H_2O clusters on hydroxylated FeO showing a hexagonal ring structure. Scale bars: 10 Å. (c) Schematic model of the hexagonal ring structure on hydroxylated FeO inferred from STM measurements; upper section gives a cross-section view; bottom an atop view. 40

Figure 4.4 Top (a) and side (b) views of the optimized structure of a S_6 cyclic water hexamer in the gas phase. Dashed lines indicate hydrogen bonds. In the S_6 structure, all hydrogen bond lengths are 1.65 Å. H and O atoms are indicated by yellow and green spheres, respectively. 42

Figure 4.5 Tilted side (a,c,e) and top (b,d,f) views of three cyclic water hexamers, differing in the orientations of the molecules, adsorbed on the hydroxylated FeO film as determined by DFT+U calculations. All numerical values for bond lengths are in Å. Green (white) dashed lines in (a,c,e) indicate hydrogen bonds between the hexamer and the surface where the water acts as a hydrogen bond acceptor (donor). Green (white) dashed lines in (b,d,f) indicate hydrogen bonds where the parallel water is accepting (donating) a hydrogen bond. Note the transfer of one H^+ ion from the surface to one water molecule, forming a hydronium (H_3O^+) ion, in the C_s structure, highlighted by dashed white ovals in (c,d). Blue, purple, red, and white spheres indicate Pt, Fe, O, and H atoms, respectively. H and O atoms in H_2O are highlighted by yellow and green spheres, respectively. 43

Figure 4.6 Tilted side (a) and top (b) view of the lowest-energy structure of a C_3 cyclic water hexamer adsorbed on bare FeO/Pt(111), i.e. *without* pre-adsorbed H, as determined by DFT+U calculations. All lengths are given in Å. White dashed lines in (a) indicate hydrogen bonds between the hexamer and the surface. Green (white) dashed lines in (b) indicate hydrogen bonds where the parallel water is accepting (donating) a hydrogen bond. Blue, purple, red, and white spheres indicate Pt, Fe, O, and H atoms, respectively. H and O atoms in H_2O are shown by yellow and green spheres, respectively. 44

Figure 4.7 TPD measurements (2 K/s linear ramp) of H_2O from (a) bare FeO/Pt(111), and hydroxylated FeO films with OH coverages of (b) 0.05 ML, (c) 0.09 ML, (d) 0.12 ML, (e) 0.18 ML. Dashed lines indicate primary desorption features (see text); traces obtained with an initial H_2O coverage of 0.44 ML are plotted in red for easy comparison. (f) Plot of the peak temperature of the highest-temperature desorption feature (α for bare FeO, β for hydroxylated FeO) for various OH coverages and H_2O exposures. 48

Figure 4.8 STM images of H_2O adsorbed on hydroxylated FeO with various OH coverages and H_2O exposures. (a) 0.1 ML H_2O, 0.12 ML OH, (b) 0.25 ML H_2O, 0.05 ML OH, (c) 0.1 ML H_2O, 0.05 ML OH. Insets in (a) and (b) are high-resolution images of H_2O clusters on the respective surfaces, showing the different structures at HCP domains with and without OH groups. Scale bars: 10 Å. 51

Figure 5.1 a) The optimized rhombohedral unit cell for bulk $L1_1$ PdAg. b) Top-view of the (110) facet of the $L1_1$ phase of PdAg. First letter of the adsorption site name indicates the geometry of the site: f = fcc, h = hcp, t = top, b = bridge; the surface atoms to which an adsorbate at the respective site is coordinated are listed inside the parenthesis, Pd (green spheres) and Ag (grey spheres); Dotted black line indicates the 2 x 2 surface unit cell. . 59

Figure 5.2 Minimum energy adsorption modes (cross section, left panel; and top view, right panel) for the individual adsorbates on PdAg(110). 63

Figure 5.3 The configurations of the calculated initial state (IS), transition state (TS) and final state (FS) of the elementary steps on PdAg(110). IS and FS depict the state used in the NEB calculation. Yellow, red, grey and green spheres represent H, O, Ag and Pd, respectively. 70

Figure 5.4 The 2D Potential energy surface diagram of the hydrogen-oxygen reaction via the dissociative, peroxyl and peroxide mechanisms on PdAg(110). Zero-energy corresponds to the energy of two H_2 and one O_2 in the gas phase. All non-gas-phase states are adsorbed, but the * is omitted for brevity. Adsorbates connected by "+" are co-adsorbed; those connected by "|" are at infinite separation. 74

Figure 5.5 The 2D potential energy surface for the selectivity determining steps along the two associative pathways: peroxide path (red) and peroxyl path leading to water (blue). The value reported in green indicates the difference between the transition state energy for peroxyl hydrogenation to peroxide and peroxyl dissociation to O+OH. All species indicated are adsorbed on the metal surface. Adsorbates connected by "+" are co-adsorbed; those connected by "|" are at infinite separation. 77

Figure 5.6 The 2D Potential energy surface for the oxygen reduction reaction on PdAg(110), Pd(111) and Ag(111) via the a) dissociative b) peroxyl and c) peroxide path. The potential energy surfaces include only the section along the reaction coordinate in Figure 5.4 that determines selectivity. All species indicated are adsorbed on the metal surface. Adsorbates connected by "+" are co-adsorbed; those connected by "|" are at infinite separation. 78

Figure 5.7 The (110) facet of PdAg: Pd (green spheres) and Ag (grey spheres). The regions shaded in red indicate the 1D arrays of active sites on the bimetallic surface..... 82

Figure 6.1 XRD pattern of carbon supported (a) IrRe and (b) Ir_3Re_1 nanoparticles synthesized by annealing at 673K in H_2 atmosphere for 1 h. 93

Figure 6.2 XAS results of Re L3 edge (10535 eV) and Ir L3 edge (11215 eV) from (a) Ir_1Re_1/C and (b) Ir_7Re_3/C catalysts prepared by hydrogen reduction of the metal chloride mixtures at 673 K. (c) TEM images of Ir_7Re_3/C catalyst. The average size of the catalyst particle is 2.2-4.4 nm. 94

Figure 6.3 Voltammetry curves for (a) Ir_7Re_3/C and (b) Ir_1Re_1/C alloy nanoparticles (dotted red lines) and the same nanoparticles after deposition of two layers of Pd and Pt monolayer (solid blue lines) in deaerated 0.1 M $HClO_4$. Sweep rate: 10 mV/s. 95

Figure 6.4 Rotating disk electrode measurements of ORR on $Pt_{ML}/Ir_2Re_1/C$, $Pt_{ML}/Pd_{ML}/Ir_2Re_1/C$ and $Pt_{ML}/Pd_{2ML}/Ir_2Re_1/C$ catalysts at 1600 rpm in O_2-saturated 0.1 M $HClO_4$. Sweep rate: 10 mV/s. 96

Figure 6.5 (a) RDE measurements of the ORR on $Pt_{ML}/Ir_2Re_1/C$ catalyst as a function of rotation rate. (b) Koutecky–Levich plot (I^{-1} vs $\omega^{-1/2}$) for $Pt_{ML}/Ir_2Re_1/C$ at potentials 0.90 V (■) and 0.85 V (o) based on the data obtained in Figure 6.5a in an O_2-saturated 0.1 M $HClO_4$. Sweep rate: 10 mV/s. 98

Figure 6.6 (a) RDE measurements of ORR on $Pt_{ML}/Pd_{ML}/Ir_2Re_1/C$ catalyst as a function of rotation rate. (b) Koutecky–Levich plot for $Pt_{ML}/Pd_{ML}/Ir_2Re_1/C$ at potentials 0.90 V (■) and 0.85 V (o) based on the data obtained in Figure 6.6a in an O_2-saturated 0.1 M $HClO_4$. Sweep rate: 10 mV/s. 98

Figure 6.7 Comparison of Pt mass activities for an Ir_2Re_1/C core with different shells (Pt_{ML}, Pt_{ML} and Pd_{ML}, and Pt_{ML} and Pd_{2ML}). Corresponding models of cross sections of nanoparticles are given. 99

Figure 6.8 Specific activities of the Pt_{ML}/Pd_{ML}/Ir-Re alloy catalysts plotted against the calculated OH binding energy. The labels indicate the Ir-Re alloy composition of each data point. 101

Figure 6.9 Accelerated stability test for $Pt_{ML}/Pd_{ML}/Ir_2Re_1$: the ORR polarization curves on a RDE in oxygen saturated 0.1 M $HClO_4$ at 1600 rpm before and after 30,000 potential cycles from 0.6 to 1.0 V. 103

Figure 7.1 Minimum energy geometries for NO adsorption at varying coverages on the 2 x 2 unit cell of Pt(111); cross-section and top views shown in upper and lower panels, respectively. The periodic unit cell in the x and y direction is indicated by the black line. Red, blue and gray spheres represent O, N, and Pt, respectively. 110

Figure 7.2 Phase diagram for NO coverage on Pt(111) (a) as a function of NO pressure at 400 K and (b) as a function of temperature at an NO pressure of 0.005 atm. The most stable state at a given pressure corresponds to the NO coverage with the most negative value for the grand potential, Ω. 111

Figure 7.3 Binding energies, site preference and top views of the minimum energy adsorption modes for the adsorbates on clean Pt(111) (low coverage) and on Pt(111) with 0.5 ML NO co-adsorbed (high coverage). For the high NO coverage systems, the site of the adsorbate is reported first, followed by the preferred sites of the two co-adsorbed NO molecules, all in the minimum energy configuration. All results are calculated in a 2 x 2 surface unit cell. Yellow, red, blue and gray spheres represent H, O, N, and Pt, respectively. 113

Figure 7.4 Transition state (TS) configurations of elementary steps on clean Pt(111) (low coverage) and on Pt(111) with 0.5 ML NO co-adsorbates (high coverage). 'NS' indicates an elementary step that was not studied on the listed surface and '—' indicates a step for

which a direct path was not found on the listed surface. Yellow, red, blue and gray spheres represent H, O, N, and Pt, respectively. 123

Figure 7.5 Reaction mechanisms for N-O bond activation in NO reduction by H_2. Labels with red numbers correspond to mechanisms in Table 2. DFT calculations showed that NO* + H* → NOH* + * does not occur as an elementary step on Pt(111) at high NO coverage. Mechanisms 4, 5 and 6 could all occur via step (i) HNO* + H* → HNOH* + * or step (ii) HNO* + H* → NOH* + H* → HNOH*. Because the maximum rates for the elementary steps in (i) are larger than those in (ii), we only consider path (i) in the analysis of mechanisms 4-6, although we do not exclude the possibility that NOH* could participate. 126

Figure 7.6 Free energy surface for N_2O formation via direct NO dissociation (mechanism 1) on clean Pt(111). The solid green line shows the PES constructed with all adsorption steps occurring along the reaction coordinate before the N-O bond-breaking step. The dotted blue line shows the PES constructed with the second NO adsorption step and H_2 dissociative adsorption occurring in the reaction coordinate after N-O bond-breaking. 126

Figure 7.7 Maximum rates of the slowest step in each mechanism, shown in Figure 7.5, on Pt(111) with 0.5 ML NO spectators, calculated using DFT-derived data. The error bars are calculated by reducing (-) and increasing (+) the DFT-derived activation energy barriers of all steps in the mechanism by 0.2 eV. Rates are calculated at a temperature of 400 K and NO, H_2, H_2O and N_2O partial pressures of 0.005 atm, 0.050, 0.0002 atm and 0.0002 atm, respectively. 140

Figure 8.1 Reaction network for NO reduction by H_2 on Pt catalysts. The green dashed lines indicate the predicted predominant mechanism without any changes to the DFT parameters, whereas the solid black lines indicate possible paths in the model that do not contribute to the flux. Products written in red are not predicted to be produced by the model, but are observed experimentally. Step numbers refer to the step numbers provided in Table 8.1. 152

Figure 8.2 Parity plot of experimental and microkinetic model calculated NO turnover frequencies. Experimental data from Table 8.2. Quality of fit: $R^2 = 0.90$. 154

Figure 8.3 Reaction network for NO reduction by H_2 on Pt catalysts. The green dashed lines indicate the predicted mechanism from the microkinetic model with the DFT parameters optimized (see Table 8.4) to obtain the best description of the experimental kinetics, whereas the solid black lines indicate possible paths in the model that do not contribute to the flux. The elementary step numbering shown on the arrows refers to the elementary step numbers provided in Table 8.1. 155

Figure 8.4 Selectivity (a) N_2/N_2O and (b) NH_3/N_2O in NO reduction by H_2 on Pt/γ-Al_2O_3 at 413 K and 101.3 kPa. Points indicate experimental data and dotted lines are predictions from the microkinetic model with the optimized DFT-derived parameters reported in Table 8.4. 157

Figure 8.5 N_2 selectivity (N_2/N_2O) in NO reduction by H_2 on $Pt/\gamma\text{-}Al_2O_3$ at 413 K and 101.3 kPa. Points indicate experimental data and dotted lines are predictions from the microkinetic model with all products formed through N* (Alternative mechanism II). The lack of agreement between the experimental and model-predicted selectivity trend for N_2/N_2O suggests that the N* pathways considered do not contribute significantly. 161

List of Tables

Table 5.1 Preferred adsorption configurations and corresponding ZPE-corrected PW91 adsorption energies (BE) of H_2*, O*, H*, OH* and H_2O* on PdAg(110), Pd(111) and Ag(111) at ¼ ML coverage. Molecular hydrogen does not adsorb associatively on Pd(111) or Ag(111). 62

Table 5.2 Preferred adsorption configurations and corresponding ZPE-corrected PW91 binding energies (BE), O-O bond lengths (dO-O), and frequency of the O-O vibrational modes (νO-O) of O_2*, OOH* and HOOH* on PdAg(110), Pd(111) and Ag(111). 64

Table 5.3 ZPE-corrected PW91 activation energy barriers (E_A) and reaction energies (ΔE) for all elementary steps. The values without (with) parentheses are based on the reactant or product states used in the NEB calculation of the minimum energy path (infinitely far apart). 66

Table 5.4 d-band center (εd) of surface atoms at various sites in PdAg(110), Pd(111), Pd(100), Pd(211), Ag(111) and Ag(211). 79

Table 6.1 Half-Wave Potentials ($E_{1/2}$) of the ORR on Pt_{ML}, $Pd_{interlayer}$ and Pt_{ML}, and two $Pd_{interlayer}$ and Pt_{ML} for the various mole ratios of Ir:Re/C core compositions 96

Table 6.2 Platinum mass, platinum group metal (PGM) mass and specific activities of Pt_{ML}, Pt_{ML} and one Pd interlayer, and Pt_{ML} and two Pd interlayers at 0.9 V/RHE for the various mole ratios of the Ir-Re/C core 100

Table 7.1 Activation energy barriers (E_A) and reaction energies (ΔE) for elementary steps on clean Pt(111) (low coverage) and on Pt(111) with 0.5 ML NO co-adsorbates (high coverage).[a] 122

Table 7.2 N_2O production in NO reduction by H_2: Maximum rates of elementary steps in competing reaction mechanisms, outlined in Figure 7.5, as calculated from DFT-derived data on Pt(111) with 0.5 ML NO spectators.[a] 138

Table 8.1 Binding energies (BE) with respect to the respective gas phase species and activation energy barriers (E_A) for elementary steps considered, all calculated with DFT-PW91 on Pt(111) with 0.5 ML NO spectators. These values were used as the initial parameters in the microkinetic model. 149

Table 8.2 Reaction conditions, turnover frequencies (TOF) and selectivities obtained from kinetics experiments on Pt/γ-Al_2O_3 at 413 K and 101.3 kPa. All rates and selectivities are the steady-state values; 'y' denotes mole fraction at the reactor inlet. 151

Table 8.3 Experimental (Pt/γ-Al_2O_3) and microkinetic model-predicted (high NO coverage Pt(111)) reaction orders at 413 K and a total pressure of 101.3 kPa. The microkinetic

model results are obtained after adjustment of the DFT-derived parameters for Pt(111), as explained in the text. 154

Table 8.4 DFT-derived parameter values on high NO coverage Pt(111) and the respective parameter values required to generate a microkinetic model that describes the experimental trends for NO reduction by H_2 on Pt/γ-Al_2O_3 at 413 K and 101.3 kPa (see Figure 8.4). 158

Table 8.5 Campbell's degree of rate control (X_{RC}) and the degree of selectivity control for elementary steps (X_{N2} and X_{NH3}), averaged over all experimental conditions reported in Table 8.1. This analysis was conducted using the DFT-derived data with the changes reported in Table 8.4, such that the flux proceeds through the pathways shown in Figure 8.3. 163

Chapter 1 Introduction

Based on the International Energy Agency's *World Energy Outlook 2013*, growth in world energy demand is projected to increase by one-third between 2011 and 2035.[1] The expected dramatic increase in energy demand has broad implications for energy security, economic development and environmental protection. In particular, carbon dioxide, a byproduct of typical fossil fuel combustion processes, has been designated as a greenhouse gas and thus a significant man-made cause of global climate change.[2] Based on current energy policies and practices, and expectations for growth in demand, energy-related CO_2 emissions have been projected to increase 20% between 2011 and 2035.[1] In the absence of technological or policy changes to alter the current emissions trajectory, the global average surface temperature is projected to increase by 2.6 to 4.8 °C (Figure 1.1),[2] which will adversely affect natural ecosystems. The impacts of this temperature increase as well as processes aiming to alter the greenhouse gas emissions trajectory are topics of current scientific research. In the fields of chemistry and engineering, in particular, the extreme increase in global energy consumption and consequences of global climate change have made the development of alternatives to petroleum derived fuels and chemicals, and improvement of the efficiency of existing processes, essential.

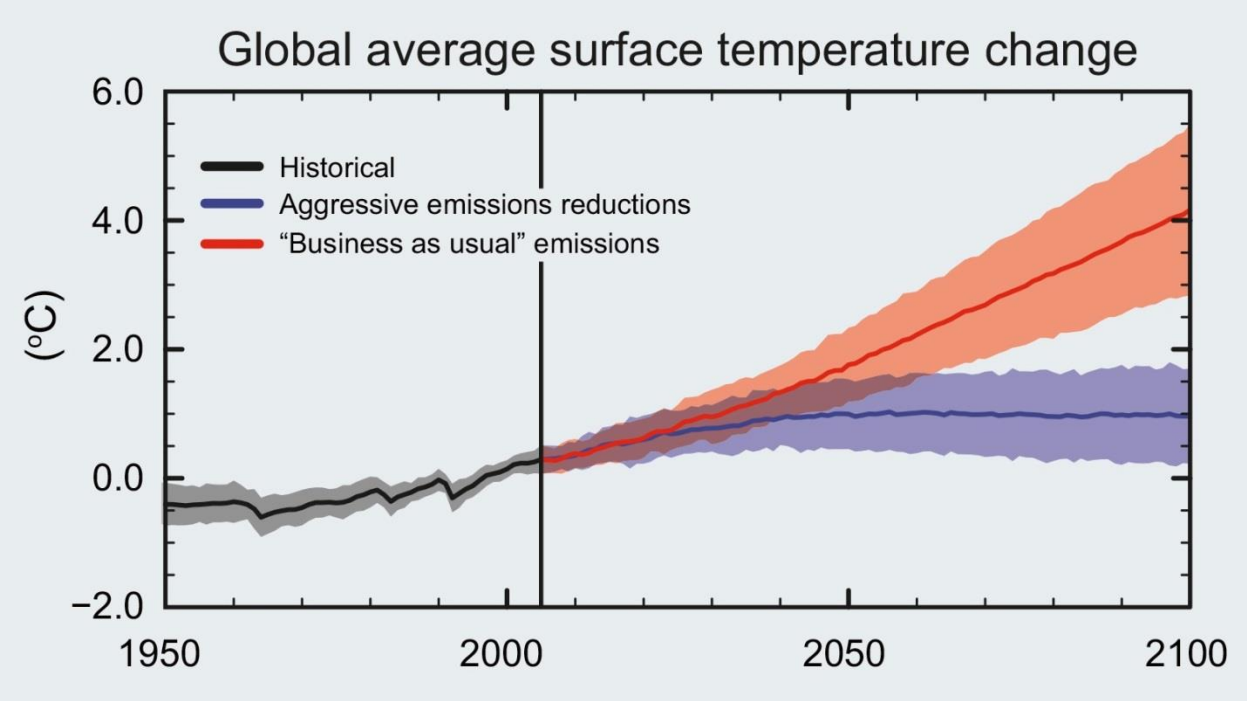

Figure 1.1 Model projected global average surface temperature for a business-as-usual emissions scenario (red) and aggressive emission reductions scenario (blue). Black is the modelled estimate of past warming. Solid lines represent the average of different model runs, and the shaded areas provide a measure of the spread (one standard deviation) between the temperature changes projected by the different models. All data are relative to a reference period (set to zero) of 1986-2005. Figure from National Academy of Sciences.[2]

Solutions to these energy and environmental challenges require innovative research ranging a breadth of length scales. Located at the atomic scale is the task of designing improved catalysts capable of converting chemical reactants to products more efficiently, and thus at lower economic, energy and environmental costs. Catalysts play a crucial role in determining the economic viability and efficiency of many important chemical reactions related to sustainability including converting biomass,[3-5] coal,[6] or natural gas[7, 8] to fuels and chemicals, CO_2 fixation,[9, 10] fuel cells,[11, 12] and exhaust gas cleaning,[13, 14] among many others.

Throughout the past decade, studies combining state-of-the-art theoretical tools with experimental surface science and reaction kinetics have greatly enhanced our understanding of heterogeneous catalysis at the atomic scale.[15, 16] The complexity of the problems that can be

studied using computational approaches including density functional theory calculations, kinetic Monte carlo simulations and microkinetic modeling, has increased due to steady growth in computational power and improved algorithms. Recent studies using combined experimental and theoretical approaches have produced significant advances, especially in the area of microkinetics.[17-19] Current research efforts in computational catalysis generally begin by aiming to obtain a detailed understanding of the surface chemistry governing catalyst activity and selectivity in a chemical reaction. This fundamental information can then be combined with theoretical studies of the electronic structure of catalytic materials to design improved catalysts for energy- and environmental-related applications.

1.1 Reaction Mechanisms

Elucidating the underlying surface chemistry is paramount to the design of improved catalysts and thus is the aim of much of the research reported in this dissertation. Progress in electronic structure calculation algorithms based on density functional theory (DFT), combined with the powerful computational resources available today, allow the generation of atomic-scale images of the reaction coordinate. Calculated reaction thermochemistry and activation energy barriers facilitate the generation of the detailed potential energy surface (PES), including all mechanistic pathways, for the conversion of reactants to products. The results from first-principles mechanistic studies have been frequently used to describe experimental results for complex reacting systems, including methanol synthesis,[17, 20] ammonia synthesis[21] and the low temperature WGS reaction,[18] to name a few. A microkinetic model can be particularly useful for bridging the pressure (i.e., vacuum conditions versus industrial pressures) and material (i.e., model single crystal surfaces versus inhomogeneous catalyst particles) gaps between first

principles calculations and realistic reaction conditions.[17-19] In this dissertation an assortment of tools for kinetic analyses are utilized to improve our understanding of the mechanisms of a variety of important surface processes including hydrogen diffusion on a metal-oxide, the direct synthesis of hydrogen peroxide from gas phase hydrogen and oxygen, and nitric oxide reduction by hydrogen.

1.2 Catalyst Design

The knowledge gained from studies in theoretical surface science has been used to direct the design of novel catalysts, capable of enhancing the activity and selectivity of specific reaction steps. A variety of important factors have been shown to affect the electronic structure, and therefore observed efficacy of a catalyst, including surface strain,[22] surface structure,[23] and the presence of species that can promote or poison elementary reaction steps.[24] These factors can now be employed to tune the behavior of a catalyst in the design process. Alloying with another transition metal, to generate a bimetallic surface or subsurface alloy (Figure 1.2) is also a common method for modifying catalyst activity. Importantly, many experimental research groups have successfully synthesized and tested surface and subsurface alloys in the form of core-shell nanoparticles. For example, first principles studies guided the identification of improved homogeneous bimetallic and near surface alloy catalysts for the oxygen reduction reaction at the cathode of fuel cells[25] and in the preferential oxidation of carbon monoxide in the presence of H_2.[19] In this dissertation, many of these catalyst design principles are applied to elucidate the relationship between the electronic structure of a bimetallic alloy and its theoretically predicted behavior for the direct synthesis of hydrogen peroxide. In another study,

a core-shell alloy, composed of transition metals that cost less than platinum, is shown to be an effective catalyst for the oxygen reduction reaction.

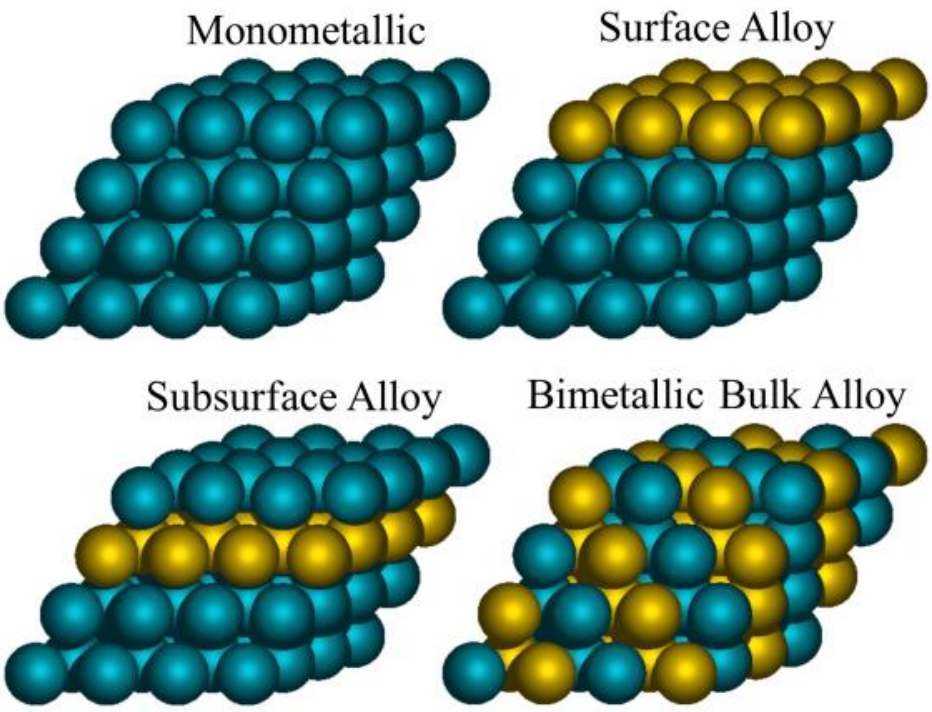

Figure 1.2 Models of the (111) facet of various bimetallic alloy structures. Blue spheres represent a metal, A, and gold spheres represent a different metal, B.

1.3 Dissertation Scope

The general introduction presented here is followed, in Chapter 2, by an overview of first principles-based calculations and their application to studies in surface science and catalysis. The two chapters that follow describe fundamental surface science studies of a model surface composed of a monolayer iron oxide film on Pt(111), conducted in collaboration with the scanning probe microscopy group of Prof. Flemming Besenbacher at Aarhus University. In the first of these chapters, Chapter 3, the diffusion of hydrogen atoms on the iron oxide surface is observed, by scanning tunneling microscopy, to be facile at low temperature in the presence of water. Density functional theory calculations and isotope-exchange experiments confirm the

STM observations, and a proton-transfer mechanism that proceeds via an H_3O^+-like transition state is revealed. In Chapter 4, the atomic-scale structure and associated energetics of water adsorption on the iron oxide film, in the presence and absence of hydroxyl groups, is discussed. Notably, whereas large amorphous monolayer islands form on the bare film, the hydroxylated iron oxide film acts as a hydrophilic nanotemplate, causing the formation of a regular array of ice-like hexameric nanoclusters.

Chapter 5 provides a detailed theoretical investigation of a PdAg homogeneous bimetallic alloy for the direct synthesis of hydrogen peroxide from gas phase hydrogen and oxygen. The results demonstrate that the minimum energy path involves the initial formation of a peroxyl (OOH) intermediate followed by O–O bond scission, suggesting that the PdAg bimetallic alloy may not be an effective catalyst for the direct synthesis of H_2O_2. The impact of alloying Ag with Pd is illustrated by comparing the energetics of the alloy with the monometallic surfaces and examining the electronic structure of the alloy surface.

In Chapter 6, through collaboration with Dr. Radoslav Adzic's electrocatalysis group at Brookhaven National Laboratory, we report that a core-shell structured electrocatalyst composed of a platinum and palladium bilayer shell deposited on an iridium-rhenium nanoparticle core shows specific electrocatalytic activity for the oxygen reduction reaction greater than that of platinum. Our density functional theory calculations revealed that the molar ratio of Ir to Re affects the binding strength of adsorbed hydroxyl and, thereby, the oxygen reduction activity of the catalysts. This finding indicates that these materials are promising alternatives to conventional Pt electrocatalysts in low temperature fuel cells.

Chapter 7 and Chapter 8 report detailed studies of the reaction mechanism in the reduction of nitric oxide by hydrogen at low temperatures on Pt catalysts. In Chapter 7, the reaction energetics on Pt(111) at high and low NO coverage are reported and the significant effect of the NO coverage on the energetics is shown. A new approach for analyzing the theoretical results, namely the maximum rate analysis, is described and applied. The results of this analysis indicate that NO activation in NO reduction by H_2 on Pt(111) occurs via a H-assisted pathway. In Chapter 8, the full microkinetic model is constructed and combined with experimental kinetics data to provide insight into the reaction pathways, including the key rate and selectivity determining steps, under realistic reaction conditions.

Chapter 2 Methods

A brief discussion of the important principles that underlie density functional theory is provided in this chapter. A thorough description of the origins and mathematical details of first principles electronic structure calculations and their application in catalysis can be found in a variety of published books[26, 27] and reviews.[28, 29]

2.1 Theoretical Foundations

The Time-Independent Schrodinger Equation (TISE) is the quantum mechanical equation upon which electronic structure theories are based.

$$H\psi = E\psi$$

In this equation, H is the Hamiltonian operator, E is the total energy and ψ is the wavefunction. In quantum mechanics, all of the information about a given system is contained in the wave function of the system. The definition of the Hamiltonian depends on the system being described. In computational chemistry, the systems we are interested in are composed of atoms, molecules and solids and therefore contain many electrons interacting with many nuclei.

The Born-Oppenheimer approximation, which takes advantage of the fact that electrons move thousands of times more rapidly than atomic nuclei allows for separation of the TISE into nuclear and electronic mathematical problems that can be solved separately. The electronic

structure calculation can therefore be viewed as a system of electrons interacting with fixed nuclei, and the Schrodinger equation becomes

$$\left[-\frac{h^2}{2m}\sum_{i=1}^{N}\nabla_i^2+\sum_{i=1}^{N}V(r_i)+\sum_{i=1}^{N}\sum_{j<i}U(r_i,r_j)\right]\psi=E\psi$$

The three bracketed terms on the left side of this equation are the kinetic energy of each electron, the interaction energy between each electron and the atomic nuclei, and the interaction energy between the electrons. For this Hamiltonian, ψ is the electronic wave function, which is a function of the spatial coordinates of all of the electrons in the system. For problems of practical interest, this many-body equation is unsolvable, which motivated the development of approximate methods, such as density functional theory.

2.2 Density Functional Theory

Density Functional Theory relies on two theorems developed by Pierre Hohenberg, Walter Kohn and Lu Jeu Sham in the mid-1960s.

(1) The ground-state energy from Schrodinger's equation is a unique functional of the electron density.

(2) The electron density that minimizes the energy of the overall functional is the true electron density corresponding to the full solution of the Schrodinger equation.

Importantly, the electron density can be written in terms of single-electron wave functions:

$$\rho(r) = \sum_i n_i |\psi_i(r)|^2$$

The single-electron wave functions are found by solving the Kohn-Sham equations:

$$\left[-\frac{h^2}{2m}\nabla^2 + V(r) + V_H(r) + \mu_{XC}[\rho(r)]\right]\psi_i = \varepsilon_i \psi_i$$

The terms in the Hamiltonian on the left side of the equation are the electron kinetic energy, the Coulomb interactions between the electron and the nuclei, the Coulomb interactions between the electron considered in one Kohn-Sham equation and the total electron density in the system, and the exchange-correlation functional. The exchange-correlation functional includes all the quantum mechanical effects not included in the first three known terms, including the self-interaction that arises because the electron being described is also part of the total electron density. The exact form of this functional is unknown, but several empirical and semi-empirical forms have been proposed in the literature and utilized in various research applications. The development of new, improved exchange-correlation functionals is the subject of ongoing research. Throughout this dissertation the PW91 generalized gradient approximation (GGA) has been used for the exchange-correlation functional.[30]

Solution of the Kohn-Sham equations must be done iteratively, since the electron density we are solving for also defines the potentials in the equations, and this is referred to as the self-consistency loop (Figure 2.1). The self-consistent PW91 density is determined by iterative diagonalization of the Kohn–Sham Hamiltonian, Fermi population of the Kohn–Sham states (k_BT = 0.1 eV), and Pulay mixing of the resulting electronic density.[31] An outer loop, the ionic relaxation loop, uses energy and force information to update the positions of the ions to find the

locally optimized (minimum energy) geometry. For all DFT calculation results presented in this dissertation, the structures were relaxed until the Hellmann–Feynman forces acting on the relaxed atoms were smaller than 0.05 eV/Å.

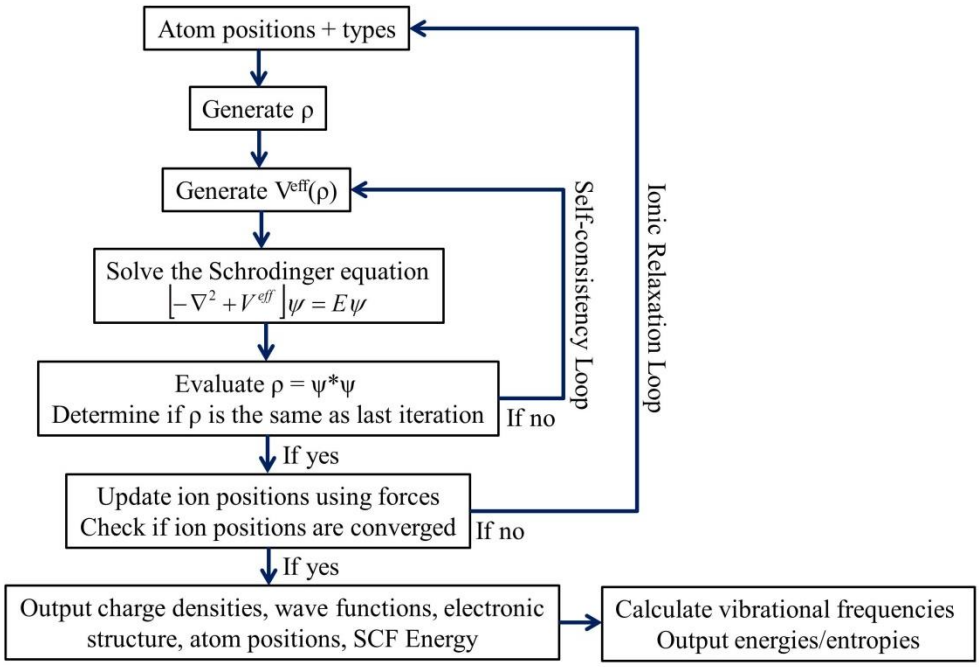

Figure 2.1 Schematic flow diagram of the key steps in density functional theory calculations. Adapted from Morgan.[32]

2.3 Applications of Density Functional Theory to Surface Chemistry

The ground state energies calculated from density functional theory can be used to calculate, among others, many different properties important in heterogeneous catalysis. The general DFT-derived properties used in analyses throughout this dissertation are described in detail here.

2.3.1 Thermochemistry and Binding Energies

The adsorption energy, or binding energy, indicates the strength with which an adsorbate binds to a surface, with more negative numbers indicating stronger adsorption. All surface chemistry calculations reported in this dissertation are calculated on slabs, repeated periodically in the x and y directions, with the specific facet indicated by Miller indices. The periodic slabs include sufficient vacuum in the z-direction to ensure there is no interaction between successive slabs. In all cases, convergence of the total energy with respect to the k point set and with respect to the number of metal layers included is confirmed. Details regarding the structure of model catalyst surfaces and specific calculation methods (e.g., total energy code used, k point set) are provided in the methods section of each chapter.

The binding energies reported throughout this dissertation, unless otherwise noted, are calculated as

$$BE = E_{total} - E_{clean} - E_{gas}$$

where E_{total} is the DFT-calculated total energy of the slab with the adsorbate on it, E_{clean} is the total energy of the clean metal slab, and E_{gas} is the total energy of the respective adsorbate in the gas phase. The binding energies can then be used for determining the heat of reaction, ΔH, of a surface reaction

$$\Delta H = \sum_{i=1}^{n} BE(Products) - \sum_{i=1}^{m} BE(Reactants) + \Delta H_{gas}$$

where n and m are the number of product and reactant species, respectively, and ΔH_{gas} is the heat of the reaction in the gas phase. Depending on the level of accuracy desired, this value for ΔH

can be corrected for the zero point energies and reaction temperature. These corrections are derived from the vibrational frequency calculations described in the next section.

2.3.2 Vibrational Frequencies

Vibrational frequencies are calculated by numerical differentiation of the forces using a second order finite difference approach with a step size of 0.015 Å. The Hessian matrix is mass weighted and diagonalized to yield the harmonic frequencies and normal modes. For surface adsorbates, the metal atoms are fixed in these calculations. The vibrational frequencies can then be used to calculate the vibrational contribution to the entropy (S_{vib}).

$$S_{vib} = k_B \sum_{i}^{\#\ of\ modes} \left(\frac{x_i}{e^{x_i} - 1} - ln(1 - e^{x_i}) \right)$$

where k_B is the Boltzmann constant and x_i for each vibrational mode is defined in terms of the vibrational frequency, ν_i, as

$$x_i = \frac{h\nu_i}{k_B T}$$

where h is Planck's constant and T is temperature. The entropy can be used to fit the parameters of the Shomate equation for a specific species, using the procedure suggested by Grabow and Mavrikakis,[20] which can subsequently be used to calculate the temperature correction to the enthalpy. In addition, the vibrational frequencies can be used to calculate the zero-point energy of a molecule.

$$ZPE = \sum_{i} \frac{h\nu}{2}$$

2.3.3 Transition State Energies

Various methods for identifying the transition state, and thereby the transition state energy, using density functional theory have been proposed. In this dissertation, minimum energy pathways and transition state energies for all elementary steps are calculated using the climbing-image nudged elastic band (CI-NEB) method.[33, 34] At least seven intermediate images are interpolated between reactant and product states for each elementary step, and adjacent images are connected by "elastic bands." Real forces act perpendicular to the bands and spring forces act parallel to the bands. The images are relaxed and allowed to move according to the calculated forces, subject to the constraint of the elastic band, and the forces perpendicular to the bands are minimized. Because the transition state is a saddle point along the reaction coordinate, at the transition state the force perpendicular to the reaction coordinate is zero. Identification of the transition state of the minimum energy pathway for each elementary step is confirmed by vibrational frequency calculations yielding a single imaginary frequency along the reaction coordinate.

2.3.4 Potential Energy Surfaces

The calculated reaction thermochemistry and activation energy barriers can be subsequently utilized in a kinetic analysis via the generation of the detailed potential energy surface for a given elementary step or sequence of elementary steps (Figure 2.2). In more detailed analyses, the entropic contributions can be incorporated to generate the analogous Gibbs free energy surface. Using these plots, the relative energetics of competing mechanisms, or of the same mechanisms on various alternative catalyst surfaces, can be compared to predict catalyst activity and selectivity. If a more rigorous analysis is desirable, a full microkinetic model can be constructed.

The general microkinetic modeling procedure is described elsewhere[35, 36] and specific details of the procedure used in this dissertation are provided in Chapter 8 (8.2.3 Microkinetic Model).

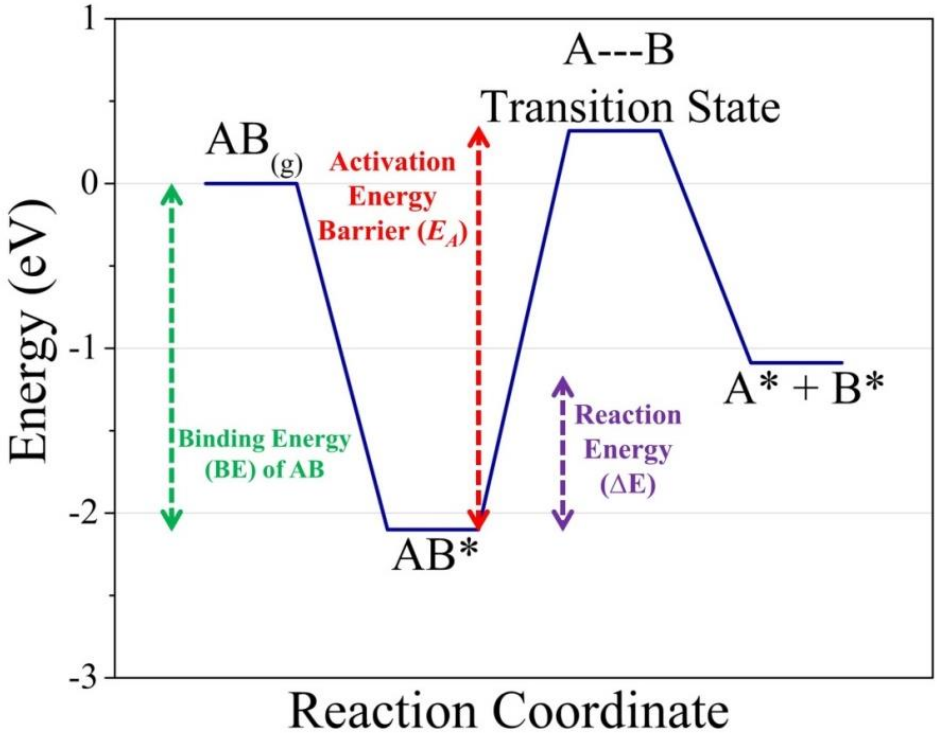

Figure 2.2 Potential energy surface (PES) for the reaction $AB_{(g)} \rightarrow A^* + B^*$, in which gas phase AB adsorbs and then dissociates to form the surface adsorbates A* and B*. The activation energy barrier and reaction energy indicated are for the surface reaction AB* → A* + B*.

Chapter 3 Water-mediated Proton Hopping on an Iron Oxide Surface[i]

3.1 Introduction

The diffusion of hydrogen on oxide surfaces is an important process in a number of applications, including catalytic hydrogen evolution and reforming,[37-39] photocatalytic dehydrogenation,[40] the synthesis of metallic materials from oxide precursors[41] and hydrogen storage.[42] Diffusion of hydrogen is particularly important in cases where "spillover" effects operate, where the active sites for H_2 dissociation or association are spatially separated from the active sites for other reactions.[37] For example, on many hydrogenation catalysts, which consist of metal nanoparticles dispersed onto a high-surface-area oxide support, H atoms produced by dissociation at the metal particles can migrate from the metal particles onto the oxide and across the oxide surface to another adsorbed reactant. Mechanisms involving spillover hydrogen have been implicated in many important catalytic reactions including methanol synthesis[43] and hydrogenation of benzene and toluene.[44] The presence of spillover hydrogen on oxides can also affect the catalytic activity of the oxides themselves, in some cases making an otherwise inactive catalyst active.[37]

[i] Merte, L. R.; Peng, G.; Bechstein, R.; Rieboldt, F.; Farberow, C. A.; Grabow, L. C.; Kudernatsch, W.; Lægsgaard, E.; Mavrikakis, M.; Besenbacher, F., *Science* 2012, 336, 889-893. Contributions by C. A. Farberow: 50% of DFT calculations and writing the theoretical sections of the manuscript; extensive work on synthesis of the final manuscript with L. R. Merte and G. Peng.

Enhancement of the rates of surface reactions involving hydrogen diffusion upon addition of water has been observed in a number of cases.[40, 41, 43, 45-47] However, the fundamental atomistic mechanisms underlying hydrogen diffusion on solid surfaces and the factors influencing them still remain unsettled because of the great complexity of oxide materials and the difficulty in characterizing them at the atomic level. The use of atomically flat single crystal surfaces as model systems for more complex materials allows detailed, atomic-scale characterization of surface reactions under well-controlled conditions and this so-called surface science approach has proven extremely powerful in unraveling the complex processes occurring on the surfaces of heterogeneous catalysts and related materials.[48] Scanning probe microscopies are capable of revealing the dynamic structure of materials at the atomic scale and can thus provide direct insight into reaction mechanisms and kinetics. However, experimental studies of hydrogen diffusion on well-defined model oxide surfaces are scarce[49-51] and have been limited almost exclusively to rutile TiO_2(110). In the work reported in this chapter, we investigated proton hopping on an oxygen-terminated FeO(111) monolayer film on Pt(111).

3.2 Methods and Materials

3.2.1 Experimental Methods

Pt(111) single crystals (Mateck, GmbH) were prepared by cycles of Ar^+ sputtering and annealing at 1000-1200 K, as well as oxidation treatments to remove any traces of carbon contamination, until a clean and atomically flat surface was obtained, as judged from STM and/or XPS measurements. Flat FeO thin films were then grown[52, 53] by deposition of Fe by electron-beam evaporation followed by oxidation in 1×10^{-6} mbar O_2 at 1000 K. The film coverages were determined from large-scale STM images, and could be adjusted as needed to

result in a closed 1 ML single FeO layer. Hydrogenated surfaces were produced by exposing the surfaces to atomic H (D) produced from H_2 (D_2) gas using a thermal gas cracker as described previously.[54, 55]

STM measurements were performed using a home-built Aarhus STM, mounted in an ultra-high vacuum (UHV) chamber with a base pressure of ~1×10^{-10} mbar.[56] The STM itself is mounted in an aluminum block which can be cooled to just under 100 K when in contact with a liquid nitrogen-cooled, retractable cold finger, while the piezoelectric scanner assembly is held near room temperature by heating with a Zener diode. The sample is held in thermal contact with the Al block, and during measurements, with the cold finger released so that the block hangs freely from its suspension springs, the sample and block warm at a rate of ~10 K/hour.

The water exposures prior to low-temperature (105 K and 160 K) STM measurements were performed by removing the cooled sample from the STM block using the in-vacuum transfer arm so that the sample faced the water inlet. Deionized water, degassed by several freeze-pump-thaw cycles, was dosed onto the surface using 1 ms pulses from a binary piezoelectric valve. Calibration of water coverages was performed by deposition of water onto clean Pt(111), where water forms an overlayer with known density of 1.1×10^{15} cm^{-2}.[57] TPD peak areas measured for water deposition on Pt(111), bare FeO/Pt(111), and H-FeO/Pt(111) fall on the same line when plotted against exposure, indicating constant, most likely unity, sticking probability, so that direct association of coverage with exposure is possible. The surface coverage of 1 monolayer (ML) is defined here as the density of O atoms in the FeO film, 1.2×10^{15} cm^{-2}. It was determined that a single pulse from the piezoelectric doser produced a water coverage of ~0.02 ML on the surface.

TPD experiments were carried out using a commercial UHV surface analysis system (SPECS), equipped with a Hiden quadrupole mass spectrometer (QMS) fitted with a glass shroud with a 4 mm entrance aperture as well as an X-ray source and electron energy analyzer for XPS, a SPECS variable-temperature STM-150 (Aarhus), and similar equipment for sample preparation as on the home-built STM system. For these experiments, a hat-shaped Pt(111) crystal 7 mm in diameter was used, with a type K thermocouple spot-welded to the side of the crystal. Liquid nitrogen cooling allowed the sample to be cooled to ~110 K, and a filament placed behind the sample provided radiative and electron-beam heating up to ~1200 K. A Eurotherm temperature controller was used to provide the linear heating ramp for the TPD experiments, which was set at 2 K/s for all measurements.

In the SPECS UHV TPD chamber, water (similarly deionized and degassed) exposures were performed by backfilling the chamber through a leak valve. Calibration of the water dose was also accomplished by deposition onto clean Pt(111) and measurements of the surface coverage of the water monolayer by STM. Beginning with the pristine FeO/Pt(111) film, H-D exchange measurements were performed by exposing the surface to atomic deuterium, and immediately thereafter measuring a TPD trace by ramping up to 250 K (the initial TPD measurement, where the water desorption is a result of exposure of the crystal to the chamber rest gas, is designated no. 0). The sample was subsequently cooled to 130 K, at which temperature H_2O was dosed, and a TPD trace to 250 K was immediately recorded. The procedure was repeated until insignificant quantities of D were detected in the desorbing water.

3.2.2 Computational Methods

Spin-polarized density functional theory (DFT) calculations using the DFT+U approach by Dudarev et al.[58] were performed using the VASP code.[31, 59] As in previous DFT studies of the FeO/Pt(111) system[60-62] we used the projector augmented wave (PAW) method[63, 64] and chose the parameters describing the on-site Coulomb interaction between Fe 3*d* orbitals as U = 4 eV and J = 1 eV (U_{eff} = U - J = 3 eV). To model the 1 ML FeO/Pt(111) surface we used the experimentally observed ($\sqrt{91}\times\sqrt{91}$)R5.2º unit cell consisting of one layer of Fe atoms and one layer of O atoms ("bilayer") supported on a three-layer Pt(111) slab. Activation energy barriers for hydrogen and water diffusion were calculated with adsorbates located in the 'face-centered cubic' (fcc) domain of the unit cell (see Chapter 4 (4.3.1 Hydroxylation of FeO with Atomic Hydrogen) for a detailed description of the domain designations). Activation energy barriers for intrinsic and water-mediated H diffusion on the hcp and top domains were also computed and these were found to be almost identical to those presented for the fcc domain. According to a previous study using a ($\sqrt{84}\times\sqrt{84}$)R10.9º unit cell,[62] the difference between three and seven supporting Pt layers is negligible and for that we consider our setup converged with respect to the included number of Pt metal layers. The FeO film, all adsorbates, and the top Pt layer were fully relaxed, while the bottom two layers were fixed at bulk positions using the experimental value for the Pt-Pt spacing in the (111) plane of 2.77 Å.[65] The Brillouin zone was sampled with the gamma point only. Exchange and correlation were described by the GGA-PW91 exchange-correlation functional,[30] and a kinetic energy cutoff of 400 eV was used. The initial guess for the magnetic structure is based on a row-wise anti-ferromagnetic (RW-AFM) structure, with a magnetic defect, due to the odd number of Fe atoms, at the top domain.[61] Activation energy barriers were determined through climbing image nudged elastic band (CI-NEB) calculations.[34]

3.3 Results and Discussion

The FeO monolayer thin film, which has been extensively characterized by a variety of experimental techniques, exhibits a simple hexagonal structure, with a characteristic ($\sqrt{91}$x$\sqrt{91}$)R5.2º moiré-type coincidence superlattice structure[66] caused by the mismatch between the FeO and the Pt(111) hexagonal layers. An atomically-resolved STM image of the bare FeO layer (Figure 3.1A) shows individual Fe and O atoms as well as a longer-scale (~2.5 nm) modulation in brightness from the moiré structure. Previous temperature programmed desorption (TPD) and infrared reflection absorption spectroscopy (IRAS) studies have shown that water molecules adsorb weakly on this surface,[67-69] desorbing at temperatures comparable to water multilayers and ~80-100 K lower than on TiO_2(110) and MgO(100), where interaction with exposed metal cations dominates the adsorption behavior of water.[70] On thicker Fe_3O_4(111) films, the availability of reactive Fe sites on the Fe_3O_4 surface causes water to adsorb dissociatively.[68] Thus, the Fe atoms of the FeO film must interact very weakly with adsorbed H_2O molecules, so OH-H_2O interactions can be studied in the absence of water dissociation. Note that on TiO_2(110), water dissociation was critical for water-assisted proton hopping. Additionally, by using an atomic hydrogen source, H adatoms bound to FeO lattice oxygen can be produced in a well-controlled manner, as discussed previously.[54, 71]

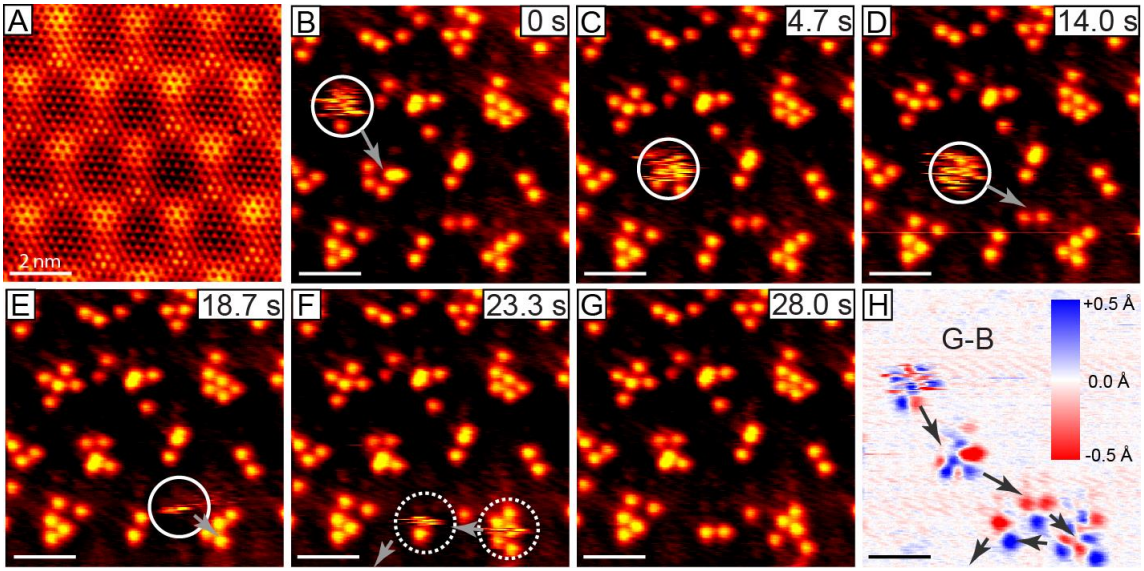

Figure 3.1 (A) An atomically-resolved STM image of the bare FeO film, showing its moiré-structure and protrusions due to individual Fe and O atoms. (B-G) Series of scanning tunneling microscopy (STM) images of the hydrogenated FeO film on Pt(111) at 105 K. The hydrogen atoms (bright spots) diffuse rapidly in the presence of a water molecule which hops from one domain to the next until it leaves the scanning area. The rapid movement of H atoms in the presence of the water molecule manifests itself as irregular streaks in the STM image, marked with circles. (H) The difference image, obtained by subtracting the first image from the last, shows the changes in H atom positions along the path of the water molecule. Scale bars in all images correspond to 2 nm.

Figure 3.1(B-G) depicts a series of STM images of the hydrogenated FeO film, where bright protrusions correspond to single H adatoms. The H atoms preferred certain sites in the film's moiré superstructure, which caused them to organize in distinct groups. The temporal sequence of STM images of the hydrogenated film, obtained at 105 K, shows the movements of H atoms induced by a water molecule that moved quickly across the surface. Favorable bonding interactions caused the water molecule to be momentarily trapped at a group of surface-bound H atoms before moving to another nearby group. While the water molecule was trapped at such a cluster, the atoms within the group rearranged rapidly and repeatedly on the time scale of the STM measurement (~18 ms per scan line), as revealed by the irregular streaked appearance of the moving H atoms in the STM images. After the water molecule moved away, the H atoms changed positions. The difference image in Figure 3.1H shows clearly the changes in positions of

the H atoms during the course of the STM measurements and thus the path taken by the water molecule as it crossed this area of the surface.

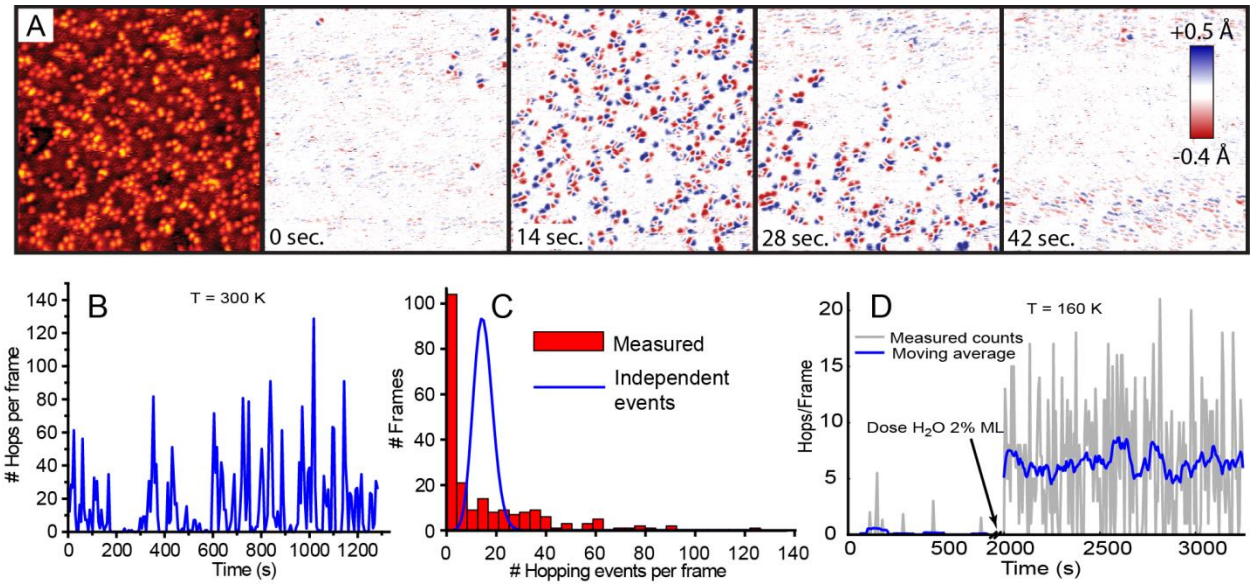

Figure 3.2 (A) Time-resolved STM measurements of hydrogen atoms on FeO(111)/Pt(111) at room temperature. The first frame shows a single 180×180 Å STM image of the FeO film showing H atoms as bright protrusions. The remaining frames are sequential difference images showing the changes in H atom positions between frames. (B) The hopping rate extracted from a room-temperature STM movie in terms of the number of hopping events observed per frame. (C) Histogram of hopping events from (B) compared with that expected for independent diffusion events. (D) Hopping rate extracted from STM movies acquired at 160 K before and after exposure to a small amount of water.

Water-mediated H atom diffusion was observed up to 300 K, but at this highest sample temperature, the diffusion events were too rapid to follow the motion of the individual mediating water species by STM, as was possible at 105 K. However, the underlying mediated diffusion mechanism (as opposed to the "intrinsic" direct hopping of an H atom from one site to another) was nonetheless reflected in the statistical characteristics of the diffusion rate. Figure 3.2A shows a series of consecutively-acquired STM difference images of the 180×180 $Å^2$ area of the surface depicted in the leftmost panel. As in Figure 3.1H, the movements of the H atoms between STM scans are visible in the difference image as pairs of red and blue spots. What is striking about the room temperature measurements is that the number of hopping events occurring in each scan

varies enormously from one image to the next. If the hopping events were independent of one another, a more stable hopping rate would be observed with variability following a Poisson distribution. In fact, the majority of STM images show basically no movement of H atoms, but in a few images dramatic events occurred in which almost all H atoms moved. Quantification of the hopping rates from a room-temperature STM movie acquired at a rate of 6 seconds/scan is presented in Figure 3.2B, and the corresponding histogram of scan-to-scan hopping rates is shown in Figure 3.2C. The average hopping rate observed in these measurements was 14.9 events/frame, and the deviation from the plot expected for a Poisson distribution for independent events occurring at this rate is apparent. The hopping events are correlated in time, and larger-scale STM measurements further reveal correlations in space on a scale of tens of nanometers (Figure 3.3).

These correlations are easily explained by a diffusion mechanism where mediating species diffuse across the surface and induce diffusion of nearby H atoms. Even under ultrahigh vacuum (UHV) conditions (~1–5×10^{-10} mbar), the number of water molecules impinging on the sample surface from residual gas in the UHV chamber was sufficient to dominate the mobility of the H atoms. Experiments where a small amount of water was intentionally dosed onto the surface at 160 K while recording STM movies show a large increase in the hopping rate after dosing (Figure 3.2D).

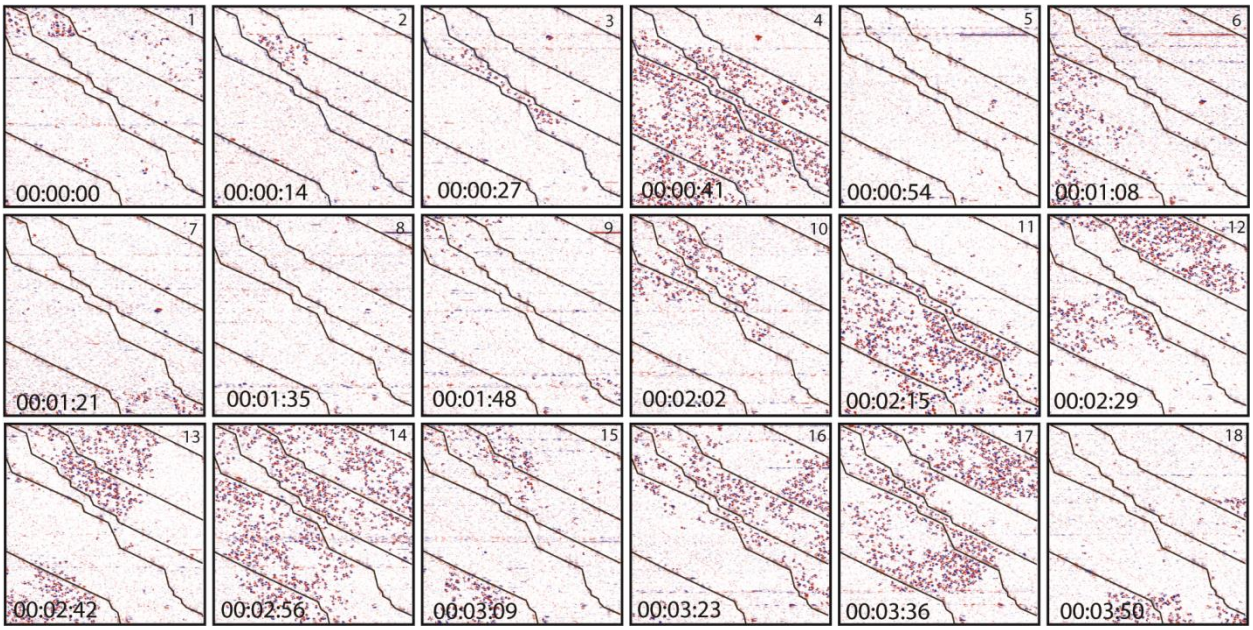

Figure 3.3 Excerpt from a room-temperature STM movie recorded on a 650 × 650 $Å^2$ area of a hydrogenated FeO/Pt(111) thin film. Each frame shown is the difference between two consecutively-acquired STM topographs, and black lines mark the positions of mono-atomic step edges (the steps are 2.25 Å in height, ascending from lower left to upper right) in the Pt(111) substrate. Red/blue pairs in the difference images represent single H atom diffusion events. The collective nature of the diffusion events is clear in these large-scale images. The non-uniformity of the 'swarms' of events is a result of the random diffusion paths of water molecules on the surface. Note further the tendency of these swarms to avoid crossing step edges.

The acceleration of hydrogen diffusion by water is generally attributed to proton transfer processes, where the water molecule donates one of its protons to a surface site and accepts a proton from another site.[38] To determine whether proton exchange processes played a role on the observed water-promoted hydrogen diffusion on FeO, we conducted a series of isotope exchange experiments where atomic deuterium (D) was used instead of atomic hydrogen to produce a hydrogenated FeO film (Figure 3.4). These experiments were performed by repeatedly dosing H_2O at 130 K to such a deuterated FeO thin film and measuring the TPD yields of H_2O, HDO, and D_2O. Each TPD experiment was stopped at 250 K to avoid reduction of the FeO film[54] and to minimize exposure of the sample to the background gas above the water desorption temperature. Desorption of water from the sample surface is observed at ~180 K, where sharp peaks are observed for all three isotopologues (Figure 3.4A). The substantial yields of HDO and

D_2O reflect proton exchange between the water molecules and the deuterated surface. Repeated H_2O doses led to an exponential decay of the deuterium fraction, as shown in Figure 3.4B, and the rate of this decay indicates that complete isotopic scrambling, and thus facile proton exchange, occurred at temperatures below 160 K.

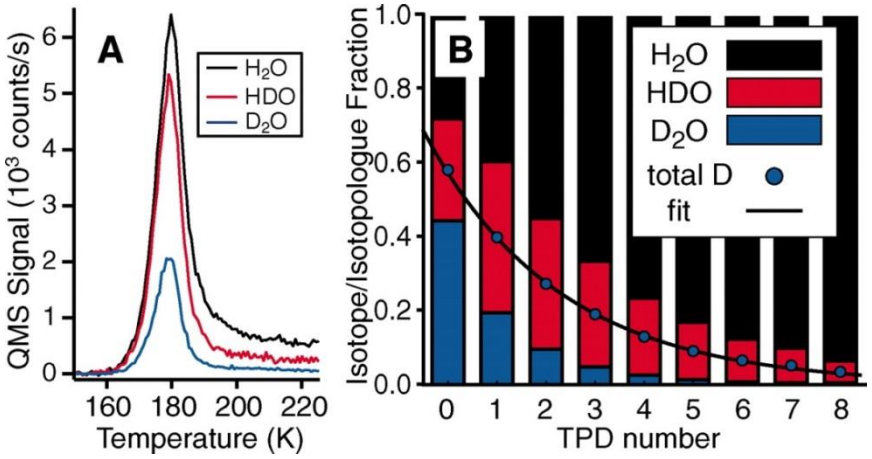

Figure 3.4 Isotope exchange between adsorbed D atoms and dosed H_2O. (A) Example of a TPD measurement where H_2O was dosed onto a D-covered surface. The peaks at 180 K due to HDO (m/z = 19), and D_2O (m/z = 20), in addition to that of H_2O (m/z = 18), arise from proton exchange with the surface. (B) Fraction of each isotopologue and of total deuterium in the desorbing water, from a series of TPD measurements where the sample was re-cooled after each measurement and exposed again to H_2O. Formation of HDO and D_2O depletes the deuterium fraction, which decays exponentially with the number of measurements.

To elucidate the underlying mechanism of the fast hydrogen diffusion observed in experiments we performed DFT+U calculations of H diffusion in the fcc domain of the FeO/Pt(111) system, which is the preferred domain for H-adsorption. On the fcc domain of the clean FeO/Pt(111) surface, water is weakly bound with a calculated binding energy of only -0.11 eV. However, in the presence of a pre-adsorbed H, the binding of a water molecule is -0.60 eV. This enhanced binding of a water molecule is caused by the formation of a hydrogen bond with the pre-adsorbed surface H. For H diffusion to occur at temperatures as low as 105 K, the most likely mechanism is a proton transfer process mediated by H_2O as shown in insets of Figure 3.5. The reaction coordinate corresponding to the minimum energy pathway (see the blue solid line in

Figure 3.5) involves the transfer of the surface proton to the water molecule and the formation of a short-lived hydronium ion (H_3O^+) species at the transition state. Subsequently, one of the water protons is transferred to an O atom on the surface. For this process, we calculated an activation energy barrier of 0.21 eV. This activation energy barrier was found to be invariant with respect to H-coverage up to a local H-coverage similar to that in the experiments.

For comparison, we also considered the intrinsic diffusion of H atoms in the absence of H_2O molecules. In particular, we studied the direct hopping of a single H atom adsorbed from one O atom to a neighboring O in the same fcc domain. This direct proton hopping is characterized by a large activation energy barrier, ~1.02 eV (see the red dashed line in Figure 3.5), which is comparable to that for intrinsic H diffusion on TiO_2(110).[50] Thus, for temperatures below room temperature this pathway can be excluded with certainty.

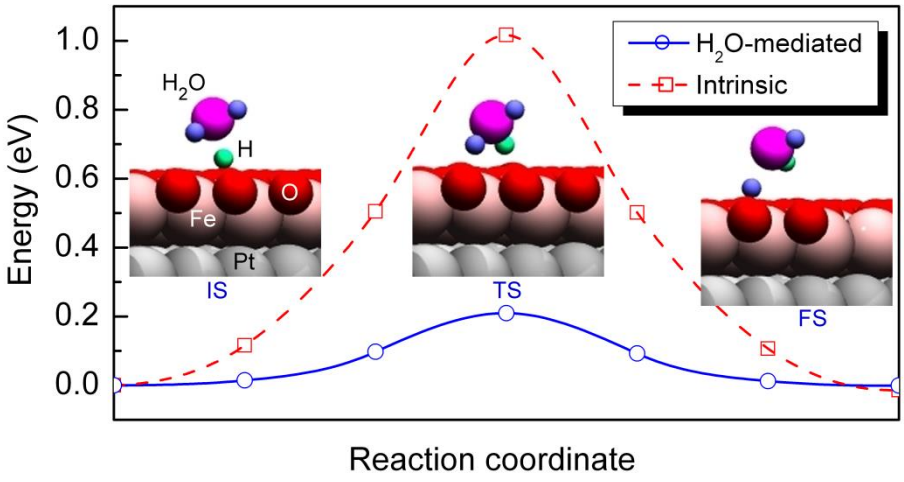

Figure 3.5 Energy profile for hydrogen atom diffusion on FeO/Pt(111): H_2O-mediated (blue solid line) and intrinsic (red dashed line); insets provide cross-section views of the initial (IS), transition (TS), and final state (FS) for the H_2O-mediated diffusion

For water molecules to promote H diffusion as observed experimentally, low activation energy barriers to water diffusion are required, in addition to proton exchange steps. To ensure

that this is indeed the case, we used DFT+U calculations to study the diffusion of water in the presence of surface hydroxyls arranged in a $(\sqrt{3}\times\sqrt{3})R30°$ overlayer. More specifically, we analyzed water rotation around a surface OH group and water hopping from one surface OH group to a neighboring one. The calculated minimum energy profile for these two processes is shown in Figure 3.6. The water molecule, adsorbed near a surface OH group, can rotate around this OH group (i.e., in the form of a H_2O-H complex) with small barriers of 0.07–0.19 eV [steps (i) $\rightarrow$ (ii) $\rightarrow$ (iii)]. Direct transfer of the H_2O molecule from one surface OH to another OH via a flip of the H_2O molecule [step (i) $\rightarrow$ (iv)] is also very facile, with an energy barrier of 0.26 eV. The combination of these steps allows the water molecule to change positions rapidly within a group of adsorbed H atoms, as observed in the STM images shown in Figure 3.1.

Water-mediated diffusion of H atoms on the FeO(111) thin film occurs even though no Lewis acid sites (i.e. under-coordinated metal ions) exist on this surface that can bind the water molecules strongly. Thus, the water-mediated H diffusion on FeO(111) is fundamentally different from that previously observed for water-mediated H diffusion on rutile TiO_2(110). On the anisotropic rutile TiO_2(110) surface, across-row proton hopping was found to be facilitated by dissociation and reforming of H_2O molecules at under-coordinated surface Ti^{4+} sites.[51] This process is only possible because of a particular arrangement of surface sites: a Lewis acid site to stabilize the OH species adjacent to the ‘hopping’ proton, and a Brønsted base site adjacent to the acid site to stabilize the donated proton released upon dissociation. For long-range transport by this mechanism, each Brønsted base site must also have at least one additional Lewis acid site located directly adjacent to it in a similarly favorable configuration, and it must in turn have an additional Brønsted base site next to it, forming a ‘chain’ along which the proton can be passed.

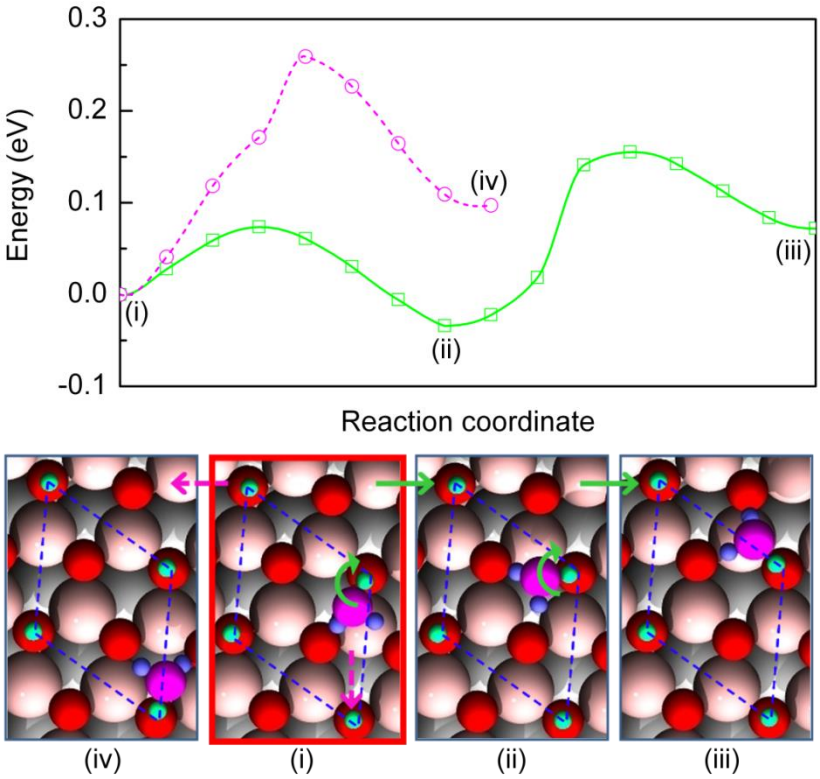

Figure 3.6 Energy profile for water diffusion on FeO/Pt(111) with a local H overlayer in a (√3×√3)R30° pattern: (i) → (ii) → (iii) rotation of the water molecule around the surface OH [see the green curved arrow in inset (i) and (ii)]; (i) → (iv) flipping of the H_2O molecule from one OH group to another [see the pink dashed arrow in inset (i)]; corresponding top views of atomic structures are shown by insets (i)—(iv).

In contrast, this study demonstrates that even in the absence of Lewis acid sites, water-mediated proton hopping still occurs. The process is more rapid than that observed on TiO_2(110), where the Lewis acid sites trap the water molecules, slowing the process considerably so that H diffusion events could be directly observed (in STM movies on a timescale of a few seconds) at temperatures as high as ~187 K.[51] On FeO(111), however, the H diffusion process is too fast to be directly resolvable on a similar timescale, even at 105 K. The observed rapid proton hopping on FeO(111) in the form of the large 'collective' diffusion events is related not only to the ease with which protons are exchanged, but also to the combination of high stability and high mobility of water molecules adsorbed through hydrogen bonding.

3.4 Conclusions

From an interplay between STM and DFT studies we revealed that the mobility of hydrogen on the FeO(111) thin film grown on Pt(111) is completely dominated by a water-mediated hopping mechanism. This mechanism, revealed for H atoms on the fcc domains, consists of the transfer of a surface proton to a water molecule, leading to a short-lived hydronium ion species at the transition state. No bonding occurs between the water molecule and the metal cations of the FeO thin film. This domain-specific adsorption of H and the facile diffusion of H_2O between these domains on the flat FeO(111)/Pt(111) model oxide surface provide an illustration of how a templating species (e.g., H) may be utilized to specifically guide the surface transport of another molecule (e.g., H_2O) with nanometer-scale precision. These nanoscale conveyor belts might be useful in emerging nanofluidics applications,[72, 73] including nanotube sensors and the modeling of transport across biological membranes.

Chapter 4 Water Clustering on Nanostructured FeO Films[i]

4.1 Introduction

The structure of water adsorbed on solid surfaces has been a topic of strong and sustained research interest, which is attributable to applications in catalysis as well as diverse fields including electrochemistry, geochemistry, atmospheric chemistry, and corrosion.[70, 74-76] Due to the relative strength and particular directionality of interactions between water molecules, which are delicately balanced against molecule-surface interactions, the structures of water monolayers on various surfaces exhibit surprising diversity. This has been recently demonstrated in scanning tunneling microscopy (STM) studies,[57, 77-79] which allow direct visualization of hydrogen bonding networks. The most detailed insight into water adsorption has been achieved for single-crystal metal surfaces, where the structure of water layers is determined mainly by the dimensions of the surface unit cell and the strength of metal-oxygen bonding.[78]

As this fundamental research is primarily motivated by materials science and surface chemistry, it is desirable to take steps to extend our understanding of water adsorption and

[i] Merte, L. R.; Bechstein, R.; Peng, G.; Rieboldt, F.; Farberow, C. A.; Zeuthen, H.; Knudsen, J.; Lægsgaard, E.; Wendt, S.; Mavrikakis, M.; Besenbacher, F., *Nature Communications* 2014, 5, 4193. Contributions by C. A. Farberow: 80% of DFT calculations and writing the theoretical sections of the manuscript; extensive work on synthesis of the final manuscript with L. R. Merte and G. Peng.

clustering to the surfaces of other materials which are also involved in a variety of applications. Highly relevant in this regard are metal oxides, which are ubiquitous under ambient and aqueous conditions. Oxides add an additional level of complexity compared to metals, as water molecules can bond both to metal cations and oxide anions and, in addition, adhere strongly to OH groups formed by water dissociation, at lattice sites or at abundant structural defects.[70, 80-88] Although these fundamental aspects of water adsorption on oxide surfaces have been well-established, comparatively few microscopy studies have been conducted to provide detailed information about the structures formed and the influence of defects. As a result, understanding of water adsorption on oxides remains far behind that of adsorption on metals.

An additional relevant factor in the adsorption of water on the surfaces of natural or man-made materials is the fact that many such materials have nanometre-scale dimensions and thus present an adsorption landscape for water which is inhomogeneous. Such inhomogeneity can lead to the formation of distinct nanometre-scale water structures, as observed on a boron nitride nanomesh,[89] or can disrupt the formation of an ordered phase, as observed on stepped Pt surfaces.[90] On oxide surfaces, an inhomogeneous distribution of defects or the presence of different facets can lead to a strongly varying distribution of OH groups, creating large variations in hydrophilicity over short length scales.[87] In general it is not well-understood how nanoscale variations in surface structure impact the formation and structure of the first few wetting layers on oxide surfaces. Consequently, well-controlled studies of water adsorption on nanostructured, model oxide surfaces should be enlightening.

Monolayer FeO grown on Pt(111), as described in the previous chapter, exhibits a 2.5 nm moiré superstructure due to the ~10% lattice mismatch between the FeO film and the substrate.[66]

The resulting modulation in the film's structure, best understood in terms of periodic variation in Fe-O buckling normal to the surface, creates an inhomogeneous adsorption potential,[91] so that adsorbed atoms and molecules have been found to form arrays with the periodicity of the film's superstructure instead of forming larger, more random aggregates.[92, 93] Although previous temperature-programmed desorption (TPD), infrared reflection absorption spectroscopy and ultraviolet photoelectron spectroscopy studies of water adsorbed on ultra-thin FeO(111) films have shown rather weak interactions between water and the surface,[67, 69, 83] no microscopy studies have been reported to date and the potential effect of the films' moiré structure on the adsorption has not been considered. Additionally, as demonstrated in previous studies,[54, 71, 94] OH groups can be introduced to the FeO surface in a well-controlled manner by exposure to atomic hydrogen enabling us to directly and systematically study the effects of hydroxylation on H_2O adsorption and clustering. As will be discussed below, the OH groups formed in this manner also show a distinct spatial distribution following the film's moiré structure, allowing us to examine the impact of nanometre-scale variations in defect density. In this chapter, we report a combined experimental and theoretical study of water adsorption, clustering and desorption on bare and hydroxylated monolayer FeO/Pt(111) films at low temperatures.

4.2 Methods

The experimental equipment and procedure for STM and TPD measurements are identical to those described in Chapter 3 (3.2.1 Experimental Methods). The DFT calculation procedure used in this Chapter is also described in detail in Chapter 3 (3.2.2 Computational Methods).

4.3 Results

4.3.1 Hydroxylation of FeO with Atomic Hydrogen

An STM image of the bare FeO/Pt(111) surface is displayed in Figure 4.1a, with a structural model of the film shown in Figure 4.1b. As is clear in the STM image, the FeO film exhibits a distinct moiré superstructure, which can be described in terms of three high-symmetry domains. These domains are distinguished by the local stacking sequence of the Fe and O layers relative to the high-symmetry points of the Pt(111) surface: At the FCC domain (square), Fe ions reside above *fcc* hollow sites and O ions reside above *hcp* hollow sites; at the HCP domain (triangle), Fe ions reside above *hcp* hollow sites and O ions reside above Pt atoms; at TOP domains (circle), Fe ions reside above Pt atoms and O ions reside above *fcc* hollow sites. Unambiguous identification of the different domains in STM images has been achieved through intentional creation of defects in the FeO film.[55, 61] It has been shown that, under the imaging conditions of Figure 4.1a, the bright points in the TOP domains correspond to Fe ions while the bright points at the FCC domains correspond to O ions.[61]

Figure 4.1c shows an STM image of an FeO film which has been exposed to atomic hydrogen, leading to protonation of ~5% of the FeO lattice oxygen ions. Throughout this chapter we refer to these protonated O ions as hydroxyls or OH groups, and to the surface prepared in this way as being hydroxylated. The image in Figure 4.1c was acquired at 160 K after additionally dosing ~0.02 ML water onto the surface to promote H atom mobility,[94] allowing equilibration of the structure, and to ensure that the effects of adsorbed water on the spatial distribution of OH groups, described in Chapter 3, are accounted for. This results in a more well-ordered distribution compared to what is observed directly after H atom exposure. The OH

groups appear in STM images as bright protrusions,[55] and due to rapid diffusion at this temperature, the coadsorbed H_2O is not visible. From the distribution of OH groups relative to the moiré structure (Figure 4.1d, inset), we found a strong preference for occupation of FCC domains, followed by partial occupation of HCP domains. The local arrangement of OH groups is also not random, as evidenced by their pair correlation function extracted from this image, plotted in Figure 4.1d. Here the prominent peak at the second-nearest-neighbour position (corresponding to a separation of $\sqrt{3}\cdot a$, where a is the 3.1 Å FeO lattice parameter) and smaller peak at the fifth-nearest-neighbour position (corresponding to a separation of $3\cdot a$) indicate a strong tendency toward local $\sqrt{3}\times\sqrt{3}R30°$ ordering. Such an arrangement is depicted in Figure 4.1b. DFT calculations showed that the $\sqrt{3}\times\sqrt{3}R30°$ ordering results essentially from repulsion between neighbouring OH groups; the binding energy of a single H atom in the FCC domain is -2.75 eV, while the differential binding energy of a second H atom at a nearest-neighbour site is -2.65 eV and at a second-nearest-neighbour site is -2.73 eV. Thus, the second hydroxyl at the second-nearest-neighbour site is 0.08 eV more stable than that in the nearest-neighbour configuration.

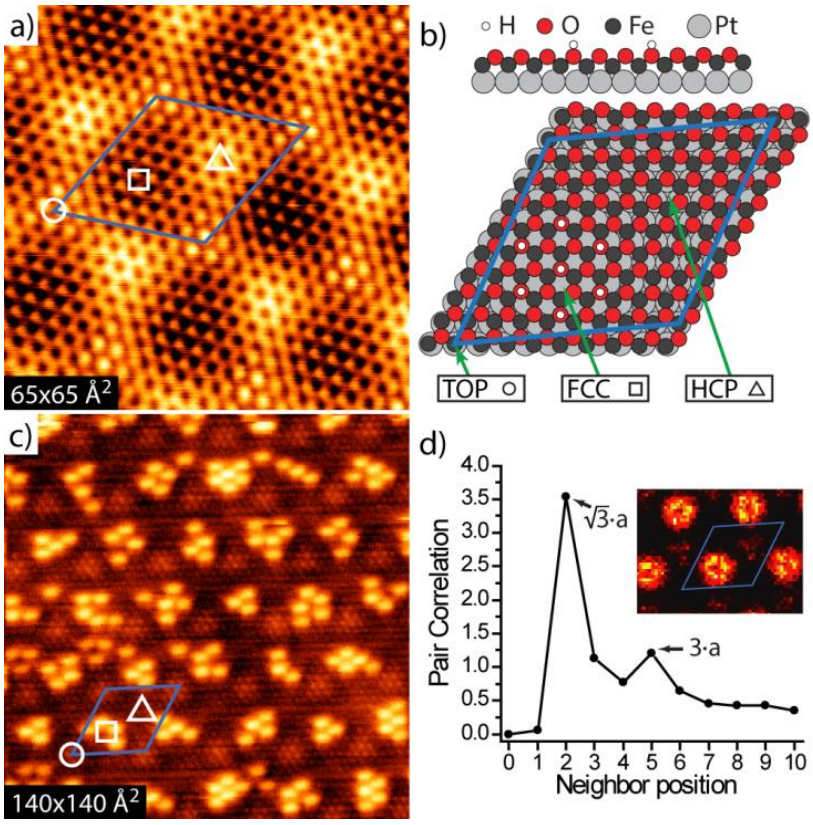

Figure 4.1 (a) STM image of the bare FeO/Pt(111) film (65 mV, 3 nA). The moiré unit cell and high symmetry domains are indicated. Circle, square, and triangle are used to denote TOP, FCC, and HCP domains respectively. (b) Ball model of the FeO/Pt(111) film. The ~25Å moiré unit cell is indicated as are the three high-symmetry domains. OH groups are shown (with white dots for H atoms) in the preferred FCC domain of the moiré unit cell in their preferred $\sqrt{3}\times\sqrt{3}R30°$ arrangement. (c) STM image (0.7 V, 0.4 nA) of the hydroxylated FeO film with an OH coverage of 0.05 ML, acquired at 160 K after additionally dosing ~0.02 ML water (not visible). (d) Pair correlation function for OH groups showing peaks at the 2nd nearest neighbour and 5th nearest neighbour positions, indicating local $\sqrt{3}\times\sqrt{3}R30°$ ordering. Inset: Distribution of OH groups within the moiré cell, showing the preference for occupation of FCC domains.

4.3.2 Effect of Hydroxylation on Water Clustering

Figure 4.2a shows an STM image of water on the bare FeO surface at 110 K, following exposure at ~130 K. Adsorbed water forms two-dimensional (2D) islands on the terraces and elongated clusters along the step edges. The irregular shapes of the water islands on the terraces result from the moiré structure, with voids formed preferentially at one type of domain, appearing brightest in the STM image (see contrast-enhanced inset in Figure 4.2a), several of

which are marked with gray dots. Under the imaging conditions employed here (+1.4 V, 0.2 nA), these bright regions in STM images of the bare FeO film correspond to TOP domains[61] where Fe ions occupy sites above Pt atoms. The tendency of water to avoid wetting these domains is an indication that interactions between water molecules and Fe ions play no significant role in the structure; we found by DFT calculations that water monomers adsorb most strongly (-0.21 eV adsorption energy) at Fe sites of TOP domains, where a larger in plane atomic spacing and smaller Fe-O rumpling make these cations more easily accessible compared to the FCC and HCP domains, where monomer adsorption energies of -0.11 and -0.13 eV were calculated. The strong preference for water to occupy FCC and HCP domains rather than TOP domains is therefore attributed to the significantly weaker electrostatic field above O atoms at TOP domains caused by the smaller rumpling of the FeO.[91, 95, 96]

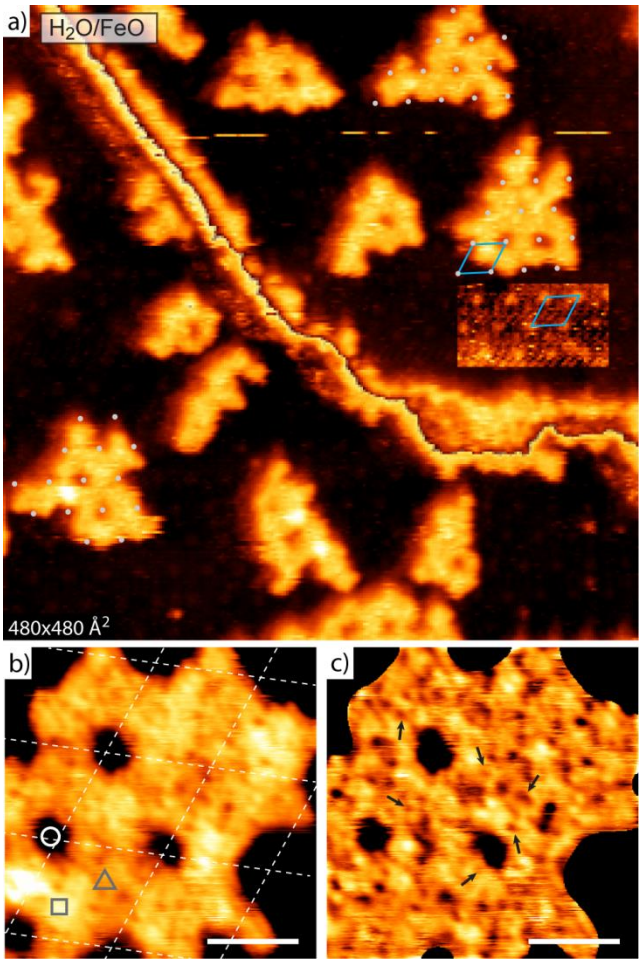

Figure 4.2 (a) STM image of water adsorbed on the bare FeO/Pt(111) film, acquired at 110 K. The moiré unit cell is indicated in blue and the positions of TOP domains in the vicinity of three H_2O islands are indicated with gray dots. The rectangular area shows enhanced contrast of the bare FeO film, where bright spots are seen corresponding to the TOP domains. The image shows two terraces (higher terrace in the upper right) separated by a single-atomic height step in the Pt(111) substrate. A cyclic colour scale is used to improve contrast. (b) High magnification STM image of a H_2O island on the bare FeO film. This image is the average of four successive STM measurements at 110 K. The grid marks the moiré unit cells, and the different domains are labelled as in Figure 4.1b. Scale bar: 20 Å. (c) The same STM image as in (b) after subtraction of the long-range height variations. Arrows indicate some of the 4-5 Å pores observed in the structure. Scale bar: 20 Å.

A high-resolution STM image of one water island on the bare FeO film is shown in Figure 4.2b. Despite some enhanced noise in such images, suggesting possible diffusion of the molecules or interactions with the STM tip, sequential images of the same island acquired over a period of ~2 min showed the structure to be essentially static. To increase the signal-to-noise ratio, four sequentially-acquired STM images were averaged to obtain the image shown in Figure

4.2b. To further enhance the molecular-scale contrast, we removed the long range variation in apparent height of the water layer by subtraction of a polynomial background, and the result is displayed in Figure 4.2c. Although individual water molecules were not resolved, the image clearly shows an absence of crystalline order, and instead indicates formation of an amorphous hydrogen-bonded network. Several pores are discernible with diameters in the range of 4-5 Å, some of which are indicated in Figure 4.2c with arrows. These pores arise from ring structures incorporating roughly 5-6 H_2O molecules, similar to those observed in ordered structures on metal surfaces.[76, 77]

The apparent height of the water layer varies between the different domains of the FeO moiré structure. Considering the very weak chemical interactions between the molecules and the surface, indicating negligible differences in electronic structure, these differences may indicate variations in the height of the water layer above the FeO film. According to DFT calculations[61] the heights of the FeO oxygen ions above the Pt interface layer follow the order TOP (307 pm) > FCC (304 pm) > HCP (298 pm), whereas the apparent height of the water layer above the FCC domains is consistently larger than that over the HCP domains and the single occupied TOP domain by 15-30 pm. This observation is consistent with the stronger electrostatic field at the FCC domains, causing a greater tendency towards vertical orientation of the water molecules, with O-H bonds directed toward the surface.[97]

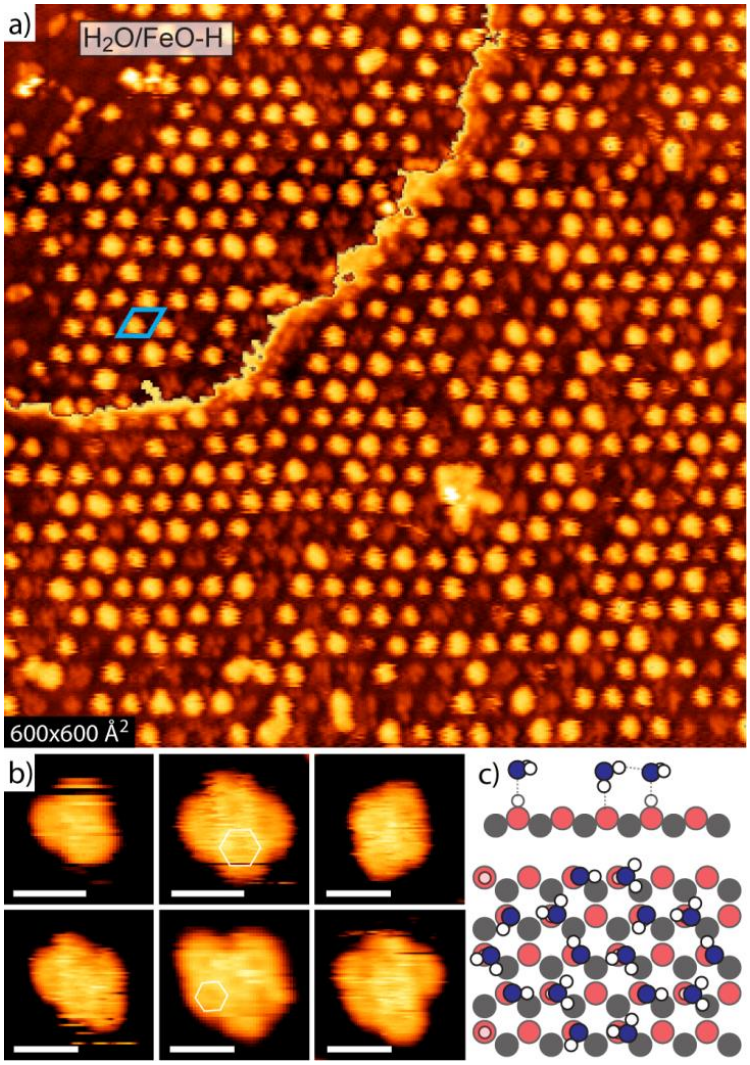

Figure 4.3 (a) STM image of water adsorbed on a hydroxylated FeO film with an OH coverage of 0.05 ML, acquired at 110 K. The moiré unit cell is indicated in blue. The image shows two terraces (higher terrace in the upper left) separated by a single-atomic height step in the Pt(111) substrate. A cyclic colour scale is used to improve contrast. (b) High-magnification images of H_2O clusters on hydroxylated FeO showing a hexagonal ring structure. Scale bars: 10 Å. (c) Schematic model of the hexagonal ring structure on hydroxylated FeO inferred from STM measurements; upper section gives a cross-section view; bottom an atop view.

The presence of surface hydroxyls on the FeO film, introduced using atomic hydrogen, changed the adsorption behaviour of water entirely, as demonstrated in Figure 4.3a. Here, instead of extended islands, we observe small, separated water clusters confined to the FCC domains of the moiré unit cells. Thus, the strong affinity of water for surface OH groups enables the FeO

film, which itself exhibits a relatively flat potential energy surface for water adsorption, to act as a nano-scale template for water clusters.

In addition to altering the size and shape of water clusters formed on FeO, the presence of OH groups has a striking effect on the molecular-scale ordering of the water within the clusters. Figure 4.3b shows high-magnification STM images of H_2O clusters of various sizes observed on a hydroxylated FeO film. The clusters exhibit a distinct hexagonal ring motif with apparent $\sqrt{3}\times\sqrt{3}R30°$ symmetry, similar to ring structures that have been observed on several metal surfaces[75]. Assuming that the preferential $\sqrt{3}\times\sqrt{3}R30°$ ordering of OH groups observed on FeO (Figure 4.1c, d) is retained upon exposure to water, half of the H_2O molecules in the hexagonal structure should lie flat, accepting hydrogen bonds from the surface OH while the other half should be oriented vertically, donating hydrogen bonds to surface O ions. A schematic model of the proposed structure is depicted in Figure 4.3c.

4.3.3 DFT Calculations of Water Clusters on FeO

To gain further insight into the water structures observed on the hydroxylated surface, we carried out DFT+U calculations using, for simplicity, a single cyclic water hexamer[98, 99] adsorbed at the FCC domain of the FeO film populated with OH groups arranged in a $\sqrt{3}\times\sqrt{3}R30°$ pattern (see Figure 4.1b). The cyclic hexamer is the basic structural motif of ice I_h. The most stable isomer in the gas phase has S_6 symmetry and each H_2O simultaneously acts as an H-bond donor and acceptor (Figure 4.4). The relaxed, lowest-energy structure of a S_6-like water hexamer adsorbed onto hydroxylated FeO, whose symmetry is reduced upon adsorption to that of point group C_3, is depicted in Figure 4.5a, b. Three of the six H_2O molecules are oriented parallel to the surface, accepting hydrogen bonds from the surface OH (green dashed lines in Figure 4.5a),

and the remaining three H_2O molecules are oriented perpendicular to the surface, with one O-H bond oriented downwards toward a surface O atom (white dashed lines in Figure 4.5a).

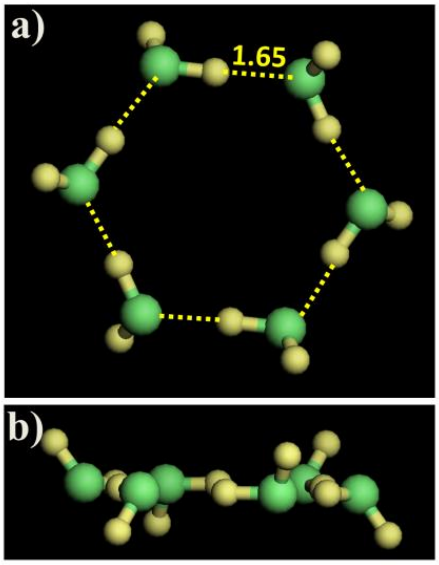

Figure 4.4 Top (a) and side (b) views of the optimized structure of a S_6 cyclic water hexamer in the gas phase. Dashed lines indicate hydrogen bonds. In the S_6 structure, all hydrogen bond lengths are 1.65 Å. H and O atoms are indicated by yellow and green spheres, respectively.

The hydrogen bonds inside the cyclic ring have two different general lengths, which alternate around the ring. This can be understood by focusing on one parallel-oriented water molecule: The accepted H-bond is longer (1.85-1.87 Å), whereas the donated H-bond is shorter (1.53-1.55 Å). Inside the cyclic ring the average length of H-bonds is 1.70 Å, slightly longer (by 0.05 Å) than that of a cyclic water hexamer in the gas phase (Figure 4.4), due to the influence of hydrogen bonds with the surface. The H-bonds between the parallel H_2O and surface OH are in the range of 1.57-1.61 Å, while the H-bonds between the perpendicular H_2O and surface O are longer (1.72-1.81 Å). Note that the parallel H_2O molecules are slightly tilted relative to the surface, with an average vertical displacement of 0.35 Å between the two H in the parallel H_2O.

This displacement is smaller than the value for the S_6 hexamer in the gas phase (0.78 Å, projected along the S_6 axis).

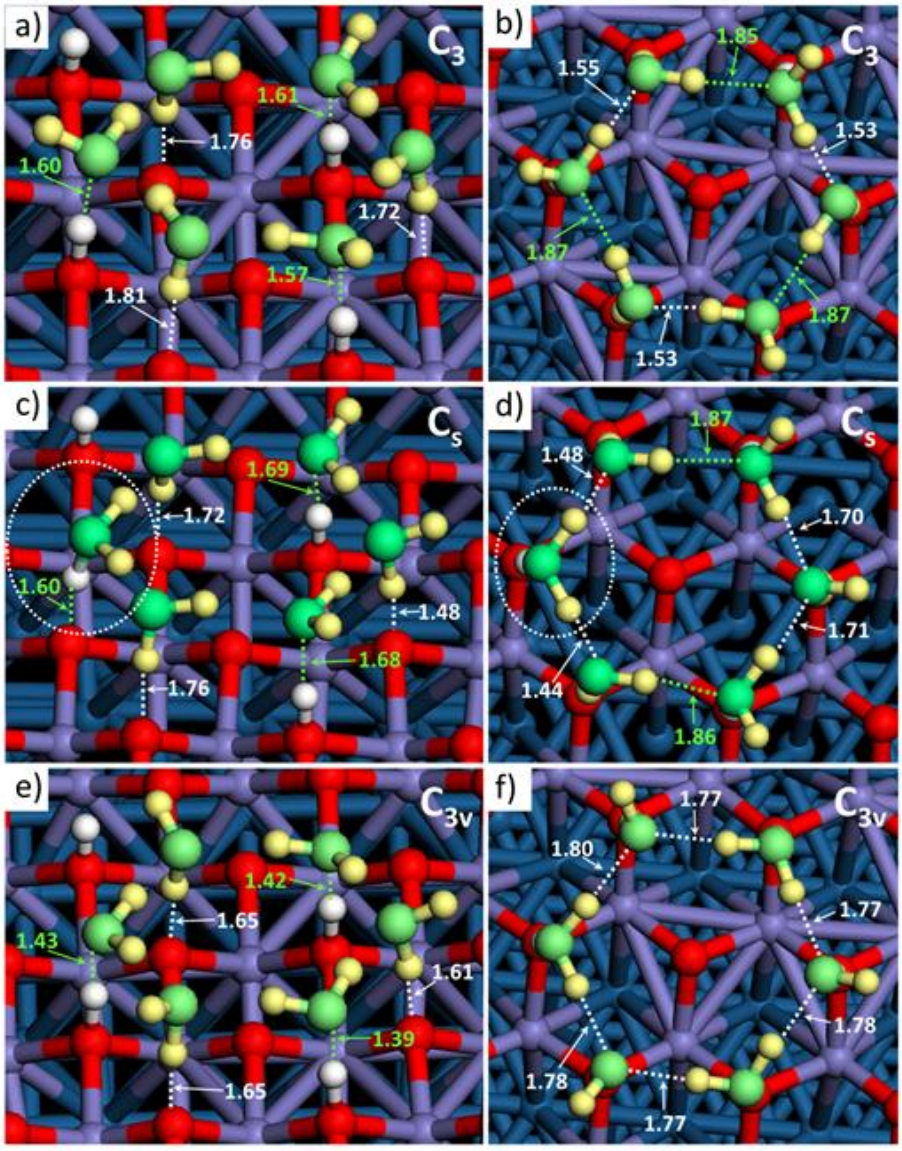

Figure 4.5 Tilted side (a,c,e) and top (b,d,f) views of three cyclic water hexamers, differing in the orientations of the molecules, adsorbed on the hydroxylated FeO film as determined by DFT+U calculations. All numerical values for bond lengths are in Å. Green (white) dashed lines in (a,c,e) indicate hydrogen bonds between the hexamer and the surface where the water acts as a hydrogen bond acceptor (donor). Green (white) dashed lines in (b,d,f) indicate hydrogen bonds where the parallel water is accepting (donating) a hydrogen bond. Note the transfer of one H^+ ion from the surface to one water molecule, forming a hydronium (H_3O^+) ion, in the C_s structure, highlighted by dashed white ovals in (c,d). Blue, purple, red, and white spheres indicate Pt, Fe, O, and H atoms, respectively. H and O atoms in H_2O are highlighted by yellow and green spheres, respectively.

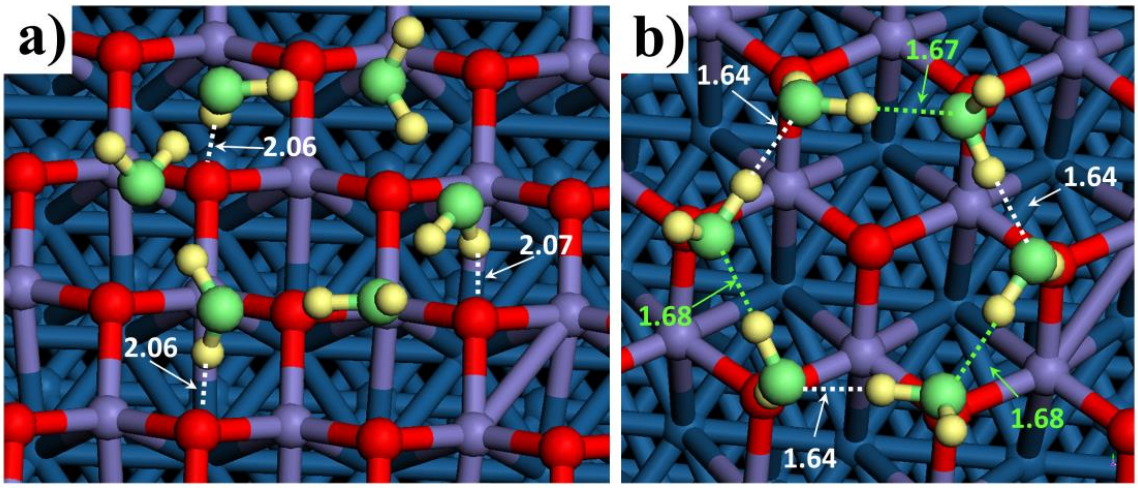

Figure 4.6 Tilted side (a) and top (b) view of the lowest-energy structure of a C_3 cyclic water hexamer adsorbed on bare FeO/Pt(111), i.e. *without* pre-adsorbed H, as determined by DFT+U calculations. All lengths are given in Å. White dashed lines in (a) indicate hydrogen bonds between the hexamer and the surface. Green (white) dashed lines in (b) indicate hydrogen bonds where the parallel water is accepting (donating) a hydrogen bond. Blue, purple, red, and white spheres indicate Pt, Fe, O, and H atoms, respectively. H and O atoms in H_2O are shown by yellow and green spheres, respectively.

The average adsorption energy of H_2O in the C_3 hexamer (Figure 4.5a, b), relative to isolated, gas-phase H_2O molecules, is calculated to be -0.68 eV per H_2O. For reference, the adsorption energy of an isolated H_2O molecule hydrogen bonded to a surface OH is -0.62 eV and that of an isolated molecule on the bare FeO surface ranges from -0.1 eV to -0.2 eV, depending on the moiré domain. H_2O adsorbed as a C_3 hexamer on the bare FeO surface (Figure 4.6) has a mean adsorption energy of -0.42 eV per H_2O molecule (referenced to isolated gas-phase H_2O), nearly all of which is due to intermolecular hydrogen bonding; for a similar S_6 cyclic hexamer in the gas phase (Figure 4.4) we calculated a formation energy of -0.39 eV per H_2O.

In bulk ice I_h, where all H_2O molecules are found in a tetrahedral bonding arrangement, each donating and accepting two hydrogen bonds to its neighbours, the positions of the protons (i.e., the orientations of the water molecules) do not exhibit crystalline order but are instead random,

within the constraint that the H-bonds remain saturated, and a transition to an ordered structure only occurs at very low temperatures.[100] Breaking of the bulk symmetry, as occurs at surfaces and in nanostructures, has the potential to induce proton ordering by eliminating the near-degeneracy of structures with water molecules in different orientations.[101, 102]

To investigate the extent of proton ordering in H_2O nanoclusters on FeO, we performed additional calculations using a different cyclic hexamer where one of the H_2O molecules acts as a double H-bond donor, and a second acts as a double-H-bond acceptor (Figure 4.5c, d). This cyclic H_2O hexamer has C_s symmetry and is 0.89 eV less stable in the gas phase than the S_6 hexamer discussed above. Remarkably, when adsorbed on hydroxylated FeO, the C_s hexamer is nearly isoenergetic with the adsorbed C_3 hexamer; the calculated average adsorption energy is -0.66 eV per H_2O. A third hexamer, characterized by C_{3v} symmetry, with three double H-bond donors and three double H-bond acceptors (Figure 4.5e, f), was likewise similar in energy to the adsorbed C_3 and C_s hexamers; although unstable in the gas phase calculation (it converged to the S_6 structure), on hydroxylated FeO the adsorption energy was calculated as -0.67 eV per H_2O. Although the differences in energy between these configurations are too small to predict which will be dominant in experimentally-observable H_2O clusters,[41,42] it is clear that the hydroxylated FeO surface significantly stabilizes bonding configurations that otherwise are unfavourable. This, very likely, leads to a significantly greater degree of proton disorder than would be expected based on gas phase results.

In the gas phase, the striking differences in stability of the three different cyclic hexamers result from the cooperative nature of hydrogen bonds in water.[103, 104] Formation of a hydrogen bond between water molecules involves a polarization of each molecule's electronic charge

density toward the region between the two molecules where the hydrogen bond is formed. This polarization depletes electronic charge from the covalent OH bonds of the acceptor molecule, increasing its tendency to act as a donor to another H_2O molecule, which in turn experiences a similar polarization, and so on. The result is, depending on the configuration, an enhancement or diminishment in mean hydrogen bond strength compared to what would be expected based on pairwise interactions, i.e. that observed in an H_2O dimer. In the S_6 water hexamer, the position of each molecule as a simultaneous H-bond donor and acceptor takes full advantage of these effects and a corresponding increase in stability is observed. In the C_s and C_{3v} hexamers, however, molecules are found which either donate two hydrogen bonds without accepting any, or which accept two hydrogen bonds without donating any. This unfavorable configuration leads to a reduction in hydrogen bond strength compared to that of an H_2O dimer, significantly destabilizing the structures.

However, by interaction with the hydroxylated FeO surface such effects are almost fully compensated. In the C_{3v} structure (Figure 4.5e, f), the three double-donor H_2O molecules accept strong hydrogen bonds from surface OH groups, with calculated O-H distances of 1.39-1.43 Å, while the three double-acceptor H_2O molecules donate relatively strong bonds to the substrate O ions, with calculated O-H distances of 1.61-1.65 Å. The effects are even more extreme for the C_s isomer, where polarization of the double-donor H_2O molecule is sufficient to draw the OH proton away from the surface, spontaneously forming an H_3O^+ ion (indicated by the dashed oval in Figure 4.5c, d). The double-acceptor H_2O at the opposite side of the molecule likewise interacts strongly with the surface, with a calculated O-H distance of 1.48 Å.

Cooperative effects are also apparent in the adhesion of the C_3 hexamer (Figure 4.5a, b). The weak interaction between the hexamer and the bare FeO surface is reflected in the H-bond lengths of the molecules with OH bonds directed toward the surface, which are calculated to be 2.06-2.07 Å (Figure 4.6). The strong hydrogen bonds formed at surface OH groups on hydroxylated FeO impart substantial donor character to the associated flat-lying H_2O molecules, which then form strong donor bonds to the neighbouring vertical H_2O molecules, as reflected by the alternating bond lengths around the ring mentioned above. As a secondary effect, the acceptance of this strong H-bond by the vertically-oriented H_2O molecules leads to a significant contraction of the hydrogen bond lengths between these molecules and the surface O ions, to 1.72-1.81 Å. Even for the FeO film, which should be considered a rather acidic oxide (on the basis of the relative strengths of donor and acceptor H-bonds with water[105]), O ions adjacent to OH groups act as H-bond acceptors as a result of cooperative hydrogen bonding. These interactions effectively separate the hexamer into three associated dimers, each held together by an especially strong hydrogen bond (1.53-1.55 Å), qualitatively similar to what has been observed for water on TiO_2(110)[88] and predicted for MgO(100)[106] and O/Ru(0001).[107]

The substantial donor character imparted to the "parallel" H_2O molecules by H-bonding to OH groups on hydroxylated FeO will create an effective repulsive interaction between these complexes, providing an additional driving force for the formation of a structure with $\sqrt{3}\times\sqrt{3}R30°$ ordering of the underlying H atoms, independent of the intrinsic distribution of H atoms on the surface described above. A similar effect has been observed in mixed OH/H_2O monolayers on Pt(111) (OH in this case referring to a distinct molecule coadsorbed with water), where very stable, ordered hexagonal structures form at a 1:1 OH:H_2O ratio as a result of alternating H-bond donor (H_2O) and acceptor (OH) molecules.[108, 109] Such a tendency toward

donor/acceptor ordering should be expected to occur as a general feature of water adsorption on hydroxylated oxide surfaces, to the extent this is compatible with the geometric features of the specific surface.

4.3.4 Desorption Kinetics

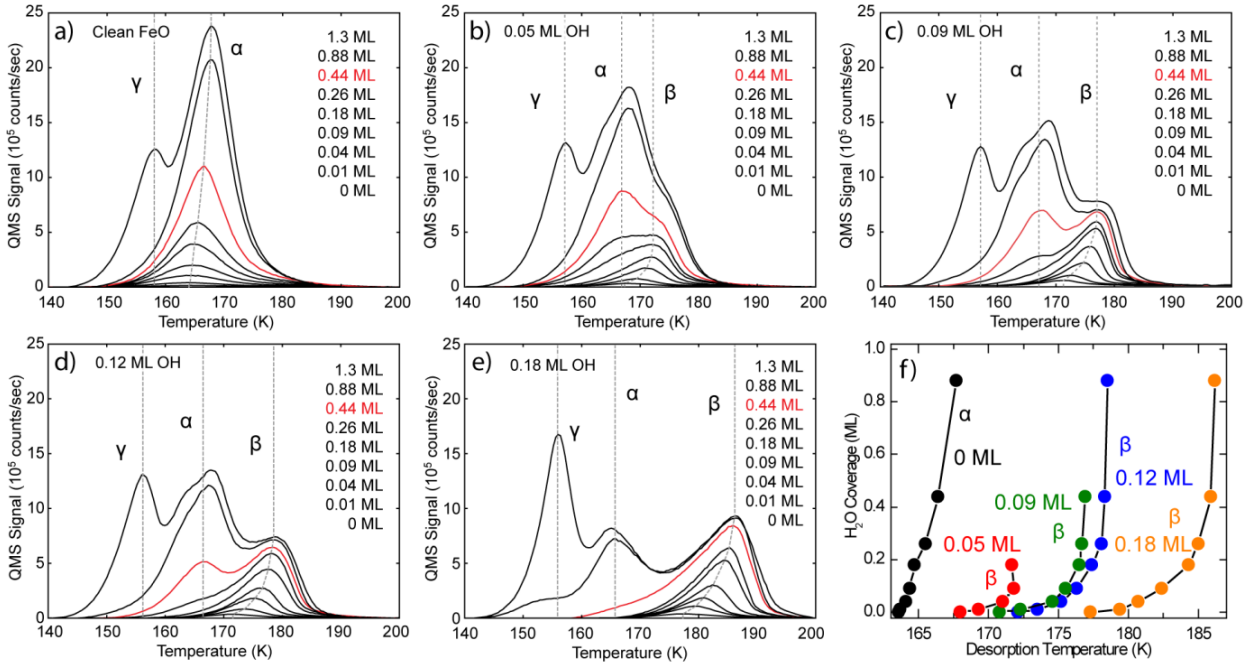

Figure 4.7 TPD measurements (2 K/s linear ramp) of H_2O from (a) bare FeO/Pt(111), and hydroxylated FeO films with OH coverages of (b) 0.05 ML, (c) 0.09 ML, (d) 0.12 ML, (e) 0.18 ML. Dashed lines indicate primary desorption features (see text); traces obtained with an initial H_2O coverage of 0.44 ML are plotted in red for easy comparison. (f) Plot of the peak temperature of the highest-temperature desorption feature (α for bare FeO, β for hydroxylated FeO) for various OH coverages and H_2O exposures.

To investigate the effect of hydroxylation on the desorption behaviour of water, we conducted TPD measurements on the bare FeO film and on films with various OH coverages (Figure 4.7). For each surface, prepared initially by exposure of the FeO film to atomic hydrogen, H_2O was dosed at 130 K and TPD traces were measured up to 250 K, after which the sample was re-cooled to 130 K and the next measurement was conducted. Reaction of OH groups to form H_2O, leading to irreversible reduction of the surface, occurs only above ~400 K.[54] Similar to previous

observations for a 2-layer thick FeO(111) film,[67] the TPD traces from the bare film show a single peak (denoted α) for sub-monolayer coverages at 164–168 K and an additional peak at ~158 K (denoted γ) due to adsorption on top of the first wetting layer. On the hydroxylated FeO surface a new feature appeared in the TPD spectra at higher temperatures, 167–186 K (denoted β). With increasing OH coverage the β feature becomes more prominent and shifts to higher temperatures. As can be seen by comparing the traces plotted in red in Figure 4.7a–e, growth of the β feature occurs at the expense of the α feature.

Interpretation of the measured TPD traces is assisted by STM measurements of different quantities of water adsorbed on FeO surfaces with varying OH coverages. The STM images in Figure 4.8 illustrate the effects of the relative H2O and OH coverages on the size and molecular structure of adsorbed water clusters at 110 K. Figure 4.8a and Figure 4.8b show surfaces where small and large quantities of water were dosed onto surfaces with high and low coverages of OH groups, respectively. On the surface (Figure 4.8a) with an excess of OH groups, whose coverage is sufficient to populate HCP domains as well as FCC domains, we observed that the islands exhibit a clear hexagonal ring structure at both the FCC and HCP domains. In contrast, on the FeO surface with a low coverage of OH groups and an excess of water (Figure 4.8b), the hexagonal ring structure is only observed at FCC domains; at the HCP domains, which are unoccupied by OH groups, a disordered structure is observed similar to that found on the bare FeO film.

Accordingly, under the conditions of the STM experiments, adsorbed water occurs in two distinct phases: an ordered phase associated with OH groups, and an amorphous phase associated with the bare FeO surface. Although it cannot be ruled out that a single mixed phase is formed at

temperatures higher than 110 K, we tentatively assign the α and β TPD features to desorption of water from bare and hydroxylated regions on the FeO film. Note also that the α feature only appears in the TPD spectra when a water coverage approximately two times the OH coverage is exceeded, indicating that the β feature corresponds to a phase incorporating a maximum H_2O:OH ratio of 2:1, as is the case for the hexagonal ring structure discussed above. Alternatively, assignment of the α feature to a mixed phase, in which the OH groups are dispersed uniformly remains a possibility. However, we find this possibility less likely, since we would expect a shift in the α peak as function of the OH:H_2O ratio, which was barely observed. Note, however, that at the highest H_2O coverages in the presence of OH groups, the α state appears to include two components, indicating that the OH groups do have some effect on the desorption kinetics, though the cause of this is not clear at present.

As noted above, the β TPD feature, associated with water adsorption at OH groups, shifts to higher temperatures both with increasing H2O coverage and increasing OH coverage. The peak positions in the different experiments are plotted together in Figure 4.7f, along with the positions of the α peak of the bare film for comparison. Variation in the β desorption temperature with OH coverage may reflect differences in H2O cluster size due to isolation of OH groups in separate moiré unit cells, since the number of OH groups per cell determines the maximum number of water molecules that can be stabilized in each. This is supported by comparison of the STM images shown in Figure 4.8a and Figure 4.8c, obtained on surfaces with the same quantity (0.1 ML) of water adsorbed onto FeO films with OH coverages of 0.12 and 0.05 ML, respectively. On the surface with the lower OH coverage (Figure 4.8c), a large number of smaller clusters is observed, whereas on the surface with high OH coverage (Figure 4.8a) a smaller number of larger clusters is seen. The corresponding difference in desorption temperature for these two

systems is ~4 K (Figure 4.7f). It is not clear from the present results whether these subtle effects, apparently due to cluster size, result from increasing thermodynamic stability with increasing size or from more complex kinetic factors.

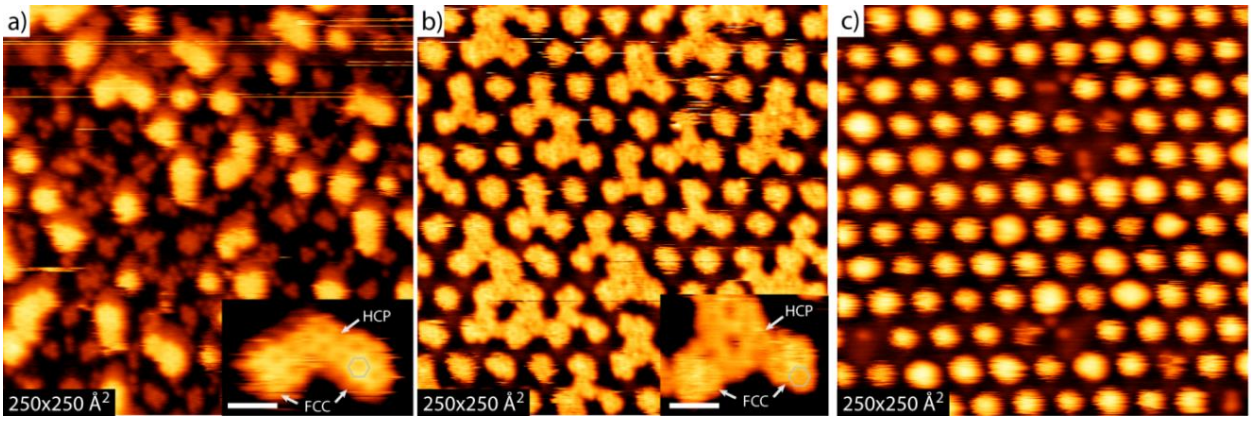

Figure 4.8 STM images of H_2O adsorbed on hydroxylated FeO with various OH coverages and H_2O exposures. (a) 0.1 ML H_2O, 0.12 ML OH, (b) 0.25 ML H_2O, 0.05 ML OH, (c) 0.1 ML H_2O, 0.05 ML OH. Insets in (a) and (b) are high-resolution images of H_2O clusters on the respective surfaces, showing the different structures at HCP domains with and without OH groups. Scale bars: 10 Å.

Finally, a feature of the TPD data worth noting is the invariance of the 2nd-layer γ desorption temperature irrespective of the surface OH coverage (Figure 4.7a-e). This result shows that the enhanced hydrophilicity conferred to the surface by the OH groups is lost after formation of the first H2O monolayer. This is similar to hydrophobic water layers studied previously on hydrophobic Pt(111)[110] and graphite[111] surfaces as well as on a hydrophilic kaolinite surface.[112] In all these cases, the preferential downward orientation of O–H bonds in the outermost water layers left surfaces devoid of "dangling H-bonds" which could bind strongly to the next layer of water. The TPD results thus provide further support for the "H-down" model of the hexagonal water structure on the hydroxylated FeO film, and indicate that, in spite of the very weak interactions with the surface, the structure formed on the bare FeO surface likewise contains few or no H_2O molecules with O-H bonds directed away from the surface. The broader implications

of this result are not trivial; under ambient temperature conditions, thermal flipping of O-H bonds away from the surface can be sufficient to create hydrophilic interactions on a surface which is hydrophobic at low temperatures, as exemplified by recent MD simulations of water interacting with kaolinite.[113, 114]

4.4 Conclusion

STM, DFT and TPD studies addressing water clustering on bare and hydroxylated FeO surfaces revealed that highly localized hydrophilic domains are formed upon hydroxylation of a moiré-structured FeO monolayer on Pt(111), such that adsorbed water forms nanometre-sized clusters rather than extended 2D islands. The water clusters exhibit a hexameric ring structure stabilized by hydrogen bonding with surface OH groups, in contrast to the larger islands on the bare surface which exhibit an amorphous structure.

The STM and DFT results suggest that within the hexagonal structure, half of the water molecules accept H-bonds from surface OH groups while the other half donate H-bonds to surface O ions, resulting in an H_2O:OH ratio of 2:1. This 2:1 ratio is supported by TPD measurements, which show a single desorption feature for H_2O coverages up to approximately two times the initial OH coverage. Remarkably, when this ratio is exceeded, excess water adsorbed on the surface is neither incorporated into the hexagonal structure, forming a phase with a diluted OH concentration, nor is it induced to form an ordered structure by proximity with the hexagonal phase. Rather, by STM, we observed a coexistence of ordered and disordered water structures on a scale of 1 nm. This result highlights the very localized influence of OH groups on the structure of the adsorbed water monolayer, in contrast to what has been observed on metal surfaces, where only small concentrations of defects are sufficient to induce large-scale

formation of ordered structures locked into simple registry with the substrate.[76] Detailed investigation, by DFT, of orientational ordering of water molecules in hexagonal H_2O nanosclusters showed that cooperative hydrogen bonding effects play a substantial role in determining the details of the structures and the interactions between water molecules and the surface. Stronger molecule-surface interactions were found to compensate for weaker intermolecular interactions in certain structures—in one case through spontaneous formation of an H_3O^+ ion—so that otherwise unfavourable configurations at the cluster edges are energetically comparable to the more balanced H-bond donor-acceptor configuration which is by far most stable in the gas phase.

The discovered templating effect of the hydroxylated FeO film allows control of the dispersion of adsorbates, making it an intriguing surface for the study of small clusters of water and other hydrophilic species. It would be interesting, for example, to investigate the orientational ordering and proton transfer dynamics of H_2O in few-molecule clusters at lower temperatures, where such structures can be fully or partially frozen. One can further envision using the hydroxylated FeO film to control the bottom-up synthesis of nanostructures based on hydrophilic components or precursors; though the templating effects of the bare FeO film itself are rather weak, being observed most clearly only at very low temperatures,[91, 93] hydrogen bonding with surface OH groups should significantly enhance ordering, enabling directed self-assembly at higher temperatures.

Chapter 5 Mechanistic Studies of Oxygen Reduction by Hydrogen on PdAg(110)[i]

5.1 Introduction

Dating back to the introduction of the term "catalysis," the direct reaction between hydrogen and oxygen on catalytic surfaces has been an intensely studied research topic.[115, 116] Recent work on this topic is motivated by the important role of the oxygen reduction reaction (ORR) taking place at the cathode of proton exchange membrane fuel cells (PEMFCs)[11, 117-119] and the direct synthesis of hydrogen peroxide (H_2O_2).[120-122] The current method for H_2O_2 production is via the anthraquinone autoxidation process, which circumvents explosive H_2-O_2 mixtures. However, this process has several drawbacks which contribute to its high capital and operating costs, including expensive periodic replacement of the quinine component, use of a complex and toxic solvent system, and energy intensive separation steps.[120, 121]

An alternative method for hydrogen peroxide production is the direct synthesis of H_2O_2 from H_2 and O_2, which is a thermodynamically favorable reaction:

$$(1)\quad H_2 + O_2 \rightarrow H_2O_{2\,(l)} \qquad \Delta G^0_{298K} = -120.4 \text{ kJ/mol}$$

i Farberow, C. A.; Godinez-Garcia, A.; Peng, G.; Perez-Roblez, J. F.; Solorza-Feria, O.; Mavrikakis, M., *ACS Catalysis* 2013, 3, 1622-1632. Contributions by C. A. Farberow: 100% of DFT calculations and writing the manuscript.

Yet, the non-selective oxidation of H_2 to water is thermodynamically even more driven:

(2) $H_2 + ½\ O_2 \rightarrow H_2O_{(l)}$ $\Delta G^0_{298K} = -237.2$ kJ/mol

H_2O_2 decomposition (3) and H_2O_2 hydrogenation (4) are also thermodynamically favorable, but undesirable side-reactions:

(3) $H_2O_{2\ (l)} \rightarrow H_2O_{(l)} + ½\ O_2$ $\Delta G^0_{298K} = -116.8$ kJ/mol

(4) $H_2O_{2\ (l)} + H_2 \rightarrow 2\ H_2O_{(l)}$ $\Delta G^0_{298K} = -354.0$ kJ/mol

For direct H_2O_2 synthesis to be a feasible alternative to the anthraquinone process, identification of a direct synthesis catalyst that selectively catalyzes reaction (1) is necessary.

The first patent for the direct synthesis of H_2O_2 was reported in 1914 for liquid-phase synthesis using a Pd catalyst.[123] Since then, many related investigations have aimed to develop more efficient processes for the direct synthesis of H_2O_2, often through the design of improved catalysts.[124-133] The addition of halide anions, specifically chloride and bromide, improves H_2O_2 yield on Pd catalysts.[129, 130] Hutchings et al. demonstrated that alloying Pd with Au improves H_2O_2 selectivity and yield in the direct synthesis, even in the absence of halide ions.[131, 132] Recently, Pd-based membrane catalysts have been examined for the direct synthesis of H_2O_2.[134-137] These H_2 impermeable membrane catalysts can operate at the desirable stoichiometric H_2/O_2 ratio thereby avoiding the hazards associated with explosive H_2/O_2 mixtures. A major drawback is that thin film Pd membranes form a brittle and catalytically inactive β-PdH phase.[138] Utilization of Pd alloys, including metals such as Cu, Ni, Fe, Pt and Ag, is one means of

preventing this problem, but identification of an alloy with desirable catalytic properties as well is an open research topic.[133, 136, 138, 139]

The mechanism for hydrogen oxidation has been thoroughly studied, using experimental and theoretical methods, on several monometallic and bimetallic catalysts.[109, 140-142] In particular, recent theoretical studies have aimed to understand the remarkable reactivity and selectivity of PdAu catalysts.[143-146] The activation energy barriers and thermochemistry of elementary steps implicated throughout the literature in the H_2-O_2 reaction can be classified as hydrogenation steps and O-O bond scission steps:

Hydrogenation

$$O_2 + H \rightarrow OOH$$

$$OOH + H \rightarrow HOOH$$

$$O + H \rightarrow OH$$

$$OH + H \rightarrow H_2O$$

$$2OH \rightarrow H_2O + O$$

O-O Bond Scission

$$O_2 \rightarrow 2O$$

$$OOH \rightarrow OH + O$$

$$HOOH \rightarrow 2OH$$

For the synthesis of H_2O_2, a catalyst which prefers hydrogenation over O-O bond scission is required. Thus, the design of bimetallic alloy catalysts, composed of reactive transition metals, such as Pd or Pt, and less reactive noble metals which tend to suppress O-O bond scission, such as Au or Ag, could be potentially useful catalysts, as demonstrated by previous studies on

PdAu.[131-133, 141] In this work, we have performed a systematic density functional theory (DFT) investigation of O_2 reduction by H_2 on a Pd-noble metal alloy, PdAg, a catalyst widely studied for its application in hydrogenation reactions.[147-149] The minimum energy path in the reaction between H_2 and O_2 on monometallic Pd has been previously shown to lead to H_2O formation via OOH dissociation.[141] Therefore, suppressing this dissociation step by alloying with Ag, which exhibits a higher barrier similar to that of Au, might result in improved H_2O_2 selectivity.[141] The detailed thermochemistry of adsorption of hydrogen oxidation reactants and intermediates, namely molecular oxygen (O_2), molecular hydrogen (H_2), atomic oxygen (O), atomic hydrogen (H), hydroxyl (OH), peroxyl (OOH), hydrogen peroxide (HOOH), and water (H_2O) on the close-packed (110) facet of PdAg is described in detail. Accordingly, the calculated energetics of the elementary steps discussed above, including activation energy barriers, are presented. These results are compared and contrasted with the analogous results recently reported by Ford et al. for the monometallic close-packed (111) surfaces of Pd and Ag[141] to illustrate the effect of alloying on the reaction energetics. The electronic characteristics of the metal atoms in the PdAg(110) surface, controlling the chemistry, are also discussed.

5.2 Methods

Density functional theory calculations are performed using DACAPO, a periodic, self-consistent total energy code.[29, 150] The exchange-correlation functional is described by the generalized gradient approximation (GGA-PW91).[30] The electron ion interactions are described by Vanderbilt ultrasoft pseudopotentials.[151] The electron wave function is expanded using plane waves with a kinetic energy cut-off of 25 Ry.[152] The self-consistent PW91 density is determined by iterative diagonalization of the Kohn-Sham Hamiltonian, Fermi population of the Kohn-Sham

states (k_BT= 0.1 eV), and Pulay mixing of the resulting electronic density.[31] All total energies are extrapolated to k_BT = 0 eV. Because gas phase molecular oxygen carries a magnetic moment, calculations involving adsorbed molecular oxygen are performed spin-polarized, whereas all other calculations are not spin-polarized. The surface Brillouin zone is sampled with a 6 x 6 x 1 Monkhorst-Pack k point grid.

The PdAg surface is modeled by the (110) facet of the stable $L1_1$ phase of the PdAg bulk alloy (Figure 5.1b).[153, 154] Our calculations show that this bimetallic surface is more stable than the (111) surface of PdAg, which contains monometallic layers. The surface is represented by a (2 x 2) four-layer slab, corresponding to 0.25 monolayer (ML) coverage for a single adsorbate in the unit cell, periodically repeated in a super cell geometry with successive slabs separated by six equivalent layers of vacuum. Adsorption is allowed on only one of the two exposed metal surfaces per slab, and the electrostatic potential is adjusted accordingly.[155, 156] The optimized lattice parameter of the bulk alloy in the rhombohedral unit cell is calculated to be 4.95 Å and the angle is 33.51^o (Figure 5.1a). The bottom two layers of the metal slab are fixed in their bulk truncated positions whereas the top two layers are allowed to relax.

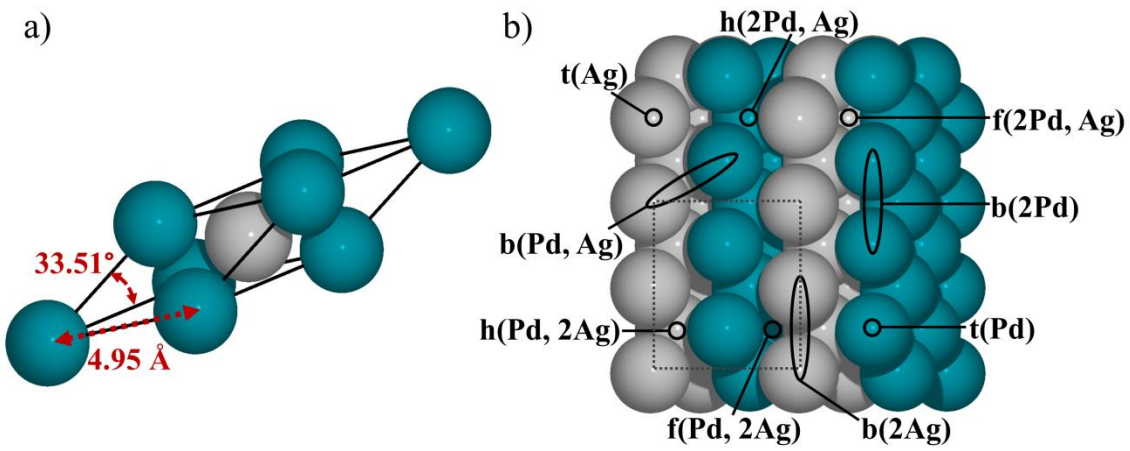

Figure 5.1 a) The optimized rhombohedral unit cell for bulk $L1_1$ PdAg. b) Top-view of the (110) facet of the $L1_1$ phase of PdAg. First letter of the adsorption site name indicates the geometry of the site: f = fcc, h = hcp, t = top, b = bridge; the surface atoms to which an adsorbate at the respective site is coordinated are listed inside the parenthesis, Pd (green spheres) and Ag (grey spheres); Dotted black line indicates the 2 x 2 surface unit cell.

Minimum energy paths and activation energy barriers for all elementary steps are calculated using the climbing-image nudged elastic band (CI-NEB) method.[34] At least seven intermediate images are interpolated between reactant and product states. The transition state of the minimum energy path for each elementary step is confirmed by vibrational frequency calculations yielding a single imaginary frequency along the reaction coordinate. All reported binding energies, activation energy barriers and reaction energies include zero-point energy corrections (ZPEC), which are calculated as $ZPE = \sum_i \frac{1}{2} h\nu_i$, where i's correspond to the different vibrational modes and ν_i are the vibrational frequencies which are calculated by diagonalizing the mass-weighted Hessian matrix.[157]

5.3 Results

5.3.1 Adsorption of Reactants and Intermediates

The high symmetry adsorption sites on the PdAg(110) surface are shown schematically in Figure 5.1b and are analogous to those found on the close-packed (111) surface of a face-centered cubic (fcc) alloy. The nomenclature for adsorption sites used throughout this chapter indicates the site by the first single letter: fcc (f), hcp (h), bridge (b) and atop (t). The metal atoms at the surface, including the number of each type, to which the adsorbate is coordinated are listed inside parenthesis. A summary of the binding energies and preferred adsorption sites on PdAg(110), and those reported by Ford et al. on Pd(111) and Ag(111) for H_2*, H*, O*, OH* and H_2O* can be found in Table 5.1. This data, with the addition of O-O bond distances and vibrational frequencies of the O-O vibrational modes, are listed for O_2*, OOH* and HOOH* in Table 5.2. The adsorption geometry and thermochemistry of all intermediates on PdAg(110) are described in the two following subsections and illustrated in Figure 5.2. The calculated activation energy barriers and reaction energies of elementary steps are discussed in a subsequent section (5.3.2 Elementary Steps). Detailed information describing the adsorption of intermediates on Pd(111) and Ag(111) have been previously described by Ford et al.[141] The computational tools and unit cell size used by Ford et al. are identical to those used in this study, however, the calculations in this study were completed with the top two layers of the slab relaxed whereas calculations performed by Ford et al. are for static slabs. Yet, relaxation effects on the calculated adsorbate thermochemistry and activation energy barriers were shown to be minimal on Pt(111).[141]

Adsorption of H_2*, H*, O*, OH*, and H_2O*

The preferred adsorption site for molecular hydrogen on PdAg(110) is at the t(Pd) site, binding through both H atoms (Figure 5.2), with a binding energy of -0.34 eV. The calculated H-H bond distance for adsorbed molecular hydrogen, H_2*, is 0.86 Å, which is elongated relative to the calculated bond distance in the gas phase (0.76 Å). This relatively strong adsorption of H_2 to a metal is reminiscent of the adsorption of dihydrogen in inorganic Kubas complexes.[158] Using a combination of experiment and theoretical calculations, Schmidt et al. found a molecular chemisorption state of H_2, reported here, on Pd(210).[159] The binding energy of atomic hydrogen, H*, is -2.65 eV at a coverage of 0.25ML. Atomic hydrogen is stable at each of the four high-symmetry 3-fold sites of PdAg(110) with similar binding strengths, but exhibits a slight preference for the f(2Pd, Ag) site. At a coverage of 0.5 ML on PdAg(110), the differential binding energy of the second H* is -2.54 eV, indicating a slight repulsion between H* at neighboring f(2Pd, Ag) sites. The preferential adsorption site for O* on PdAg(110) at 0.25 ML coverage is at the f(2Pd, Ag) site (Figure 5.2) with a binding energy of -3.55 eV. Atomic oxygen occupies the same surface site at 0.5 ML coverage; the differential binding energy for the second O* is -2.98 eV, indicating a more substantial repulsion between the two coadsorbed O*, compared to coadsorbed H* (see above).

In its most stable adsorbed state, hydroxyl, OH*, binds with an adsorption energy of -2.33 eV at the f(2Pd, Ag) site, and with its O-H bond tilted away from the surface normal (Figure 5.2). At 0.5 ML coverage, the differential binding energy of the second OH* is -2.08 eV. The preferred binding site of both OH* at 0.5 ML coverage is the b(Pd, Ag) site. At this higher coverage the H of one OH* is tilted and oriented toward the O of the neighboring OH*, allowing for H-bonding between adjacent OH*s. The O-H bond length in OH* on PdAg(110), at coverages of 0.25 ML

and 0.5 ML, is ~0.98 Å. At 0.5 ML coverage, the stronger attraction of OH*, at the b(Pd, Ag) site, to Pd can be clearly noted by the Ag-OH bond length, 2.34 Å, versus the Pd-OH bond length of 2.12 Å.

H_2O* binds weakly to the surface with a binding energy of -0.20 eV. H_2O* binds through its oxygen atom and occupies a t(Pd) adsorption site (Figure 5.2). The optimized geometry for H_2O* yields the following results: O-H bond distances of ~0.98 Å and an H-O-H angle of 104.3°. The bond angle and bond lengths of adsorbed water are virtually identical to the calculated gas phase values (O-H bond distances of 0.98 Å and an H-O-H angle of 104.3°).

Table 5.1 Preferred adsorption configurations and corresponding ZPE-corrected PW91 adsorption energies (BE) of H_2*, O*, H*, OH* and H_2O* on PdAg(110), Pd(111) and Ag(111) at ¼ ML coverage. Molecular hydrogen does not adsorb associatively on Pd(111) or Ag(111).

	PdAg(110)		**Pd(111)** [141]		**Ag(111)** [141]	
	Site	BE (eV)	Site	BE (eV)	Site	BE (eV)
H_2*	t(Pd)	-0.34	--	--	--	--
O*	f(2Pd, Ag)	-3.55	fcc	-3.64	fcc	-3.13
H*	f(2Pd, Ag)	-2.65	fcc	-2.70	fcc	-1.92
OH*	f(2Pd, Ag)	-2.33	br-tilted	-2.04	fcc	-2.28
H_2O*	t(Pd)	-0.20	top	-0.21	top	-0.13

Adsorption of O_2, OOH*, and HOOH**

Molecular oxygen adsorbs on PdAg(110) with a binding energy of -0.60 eV at the top sites on two adjacent palladium atoms (Figure 5.2). The calculated O-O bond distance in the adsorbed molecule on PdAg(110) is 1.32 Å. Compared with the calculated gas phase O-O bond length of 1.23 Å, the elongation of the molecular bond in O_2* is similar to that found for H_2*. Molecular

oxygen adsorbed on PdAg(110) carries 1.08 μ_B of magnetic moment, compared to 2.0 μ_B in the gas phase.

The binding energy of the peroxyl intermediate, OOH*, is -1.18 eV. The most stable configuration is at a b(2Pd)-t(Ag) site. This configuration has the OOH* bound through the non-hydrogenated O end at a b(2Pd) site with the OH end tilted away from the surface, creating an overall tilted state (Figure 5.2). The OH end lies above a t(Ag) site. The calculated O-OH bond length in OOH* at the b(2Pd)-t(Ag) site is 1.50 Å.

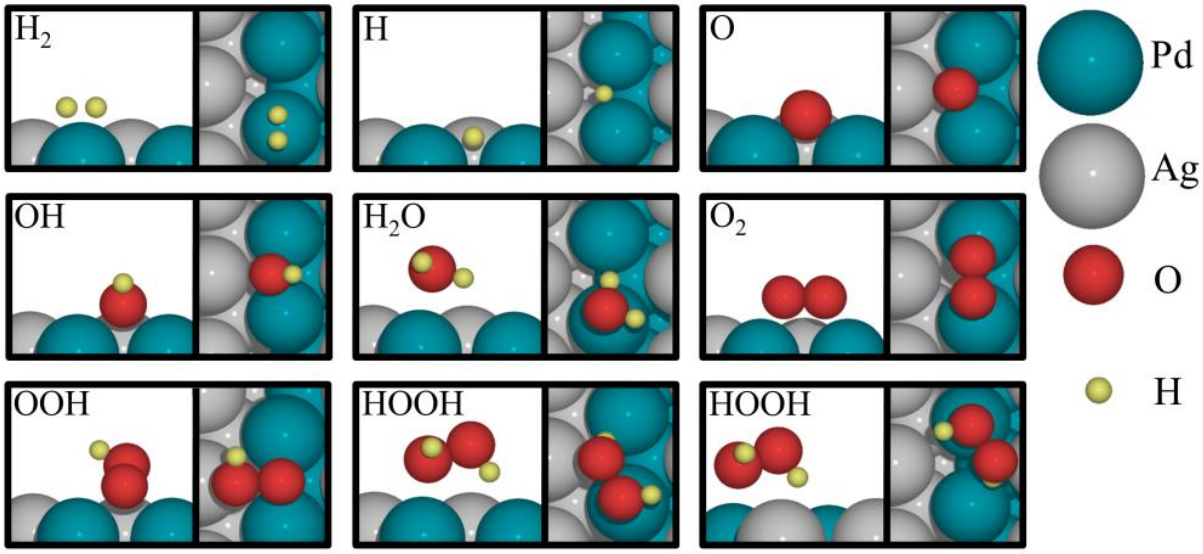

Figure 5.2 Minimum energy adsorption modes (cross section, left panel; and top view, right panel) for the individual adsorbates on PdAg(110).

The interaction of hydrogen peroxide, HOOH*, with the surface is weak; the binding energy is -0.33 eV. Two isoenergetic adsorption sites were identified as the preferred sites: t(Pd)-f(2Pd, Ag) and t(Pd)-h(2Pd, Ag) (Figure 5.2). HOOH* exhibits a similar geometry in both configurations, with the adsorbed molecule interacting more closely with the Pd atoms. Similar to the most stable configuration on many monometallic surfaces, HOOH* adsorbs on PdAg in a *trans* configuration, with one OH group bound at a top site and the H on the other OH group

tilted toward the surface, residing above a hollow site. The calculated HO-OH bond length is 1.48 Å, which is identical to the bond distance calculated for HOOH in the gas phase.

On PdAg(110), Pd(111) and Ag(111) the vibrational frequencies of the O-O stretching mode of adsorbed O_2, OOH, and HOOH all increase in the order OOH<HOOH<O_2. All of these O-O stretching modes are dipole-active and therefore, in principle, could be detected using vibrational spectroscopy. Details of studies identifying these di-oxygen intermediates on various monometallic metal surfaces has been discussed by Ford et al.[141]

Table 5.2 Preferred adsorption configurations and corresponding ZPE-corrected PW91 binding energies (BE), O-O bond lengths (dO-O), and frequency of the O-O vibrational modes (νO-O) of O_2*, OOH* and HOOH* on PdAg(110), Pd(111) and Ag(111).

	Site	**BE (eV)**	**d_{O-O} (Å)**	**ν_{O-O} (cm^{-1})**
PdAg(110)				
O_2*	t(Pd)-t(Pd)	-0.60	1.32	1065
OOH*	b(2Pd)-t(Ag)	-1.18	1.51	710
HOOH*	t(Pd)-f(2Pd, Ag), t(Pd)-h(2Pd, Ag)	-0.33	1.48	821
Pd(111)[141]				
O_2*	top-br	-0.50	1.35	928
OOH*	bent top	-0.96	1.46	704
HOOH*		-0.30	1.48	843
Ag(111)[141]				
O_2*	top-top	-0.12	1.30	1149
OOH*	bent br	-1.01	1.50	784
HOOH*		-0.18	1.47	878

5.3.2 Elementary Steps

The calculated activation energy barriers (E_A) and reaction energies (ΔE) of the elementary steps are reported in Table 5.3 and the initial state, transition state and final state of each step are illustrated in Figure 5.3. For comparison, the activation energy barriers and reaction energies reported for the Pd(111) and Ag(111) surfaces by Ford et al.[141] are also included in Table 5.3. All activation energy barriers and reaction energies reported in this chapter are calculated relative to the co-adsorbed reactant or product states used in the NEB calculation for the minimum energy path. The respective energetics based on infinitely separated reactants and products are reported in Table 5.3 along with the co-adsorbed values.

$$\boldsymbol{H_2^* \rightarrow H^* + H^*}$$

H_2* dissociation proceeds directly from the most stable, though weakly bound, t(Pd) adsorption site on PdAg(110). At the transition state (Figure 5.3), the H-H bond length is 0.95 Å, which is 0.09 Å longer than the bond length in the molecularly adsorbed state. The dissociation of H_2* is a facile step on PdAg(110), with an activation energy of only 0.09 eV and a reaction energy of -0.66 eV, in general agreement with the use of PdAg in hydrogen storage and hydrogenation applications.[160, 161] Hydrogen dissociation is spontaneous (E_A = 0 eV) on Pd(111) with a reaction energy of -0.96 eV. In contrast, this is a highly activated (E_A = 1.04 eV)[162] and endothermic (ΔE = 0.34 eV) elementary step on Ag(111).

Table 5.3 ZPE-corrected PW91 activation energy barriers (E_A) and reaction energies (ΔE) for all elementary steps. The values without (with) parentheses are based on the reactant or product states used in the NEB calculation of the minimum energy path (infinitely far apart).

Elementary Step	**PdAg(110)**		**Pd(111)[141]**		**Ag(111)[141]**	
	***E_A* (eV)**	**ΔE (eV)**	***E_A* (eV)**	**ΔE (eV)**	***E_A* (eV)**	**ΔE (eV)**
H_2* → H*+H*	0.09	-0.66	0.00	-0.96	1.04[a]	0.34
		(-0.45)		(-0.83)		(0.29)
O_2* → O*+O*	1.06	0.75	0.84	-0.67	1.22	0.43
		(-0.82)		(-1.23)		(-0.60)
O_2* + H* → OOH*	0.75	-0.19	0.63	0.04	0.20	-1.06
	(0.92)	(-0.12)	(0.80)	(0.21)	(0.26)	(-1.00)
OOH* → OH* + O*	0.26	-0.98	0.06	-1.18	0.41	-0.61
	(0.44)	(-1.42)		(-1.53)		(-1.19)
OOH* + H* → HOOH*	0.68	-0.29	0.40	-0.25	0.60	-0.78
	(0.91)	(-0.06)	(0.60)	(-0.04)	(0.71)	(-0.66)
HOOH* → OH* + OH*	0.20	-1.83	0.19	-1.39	0.18	-2.06
		(-2.07)		(-1.59)		(-2.11)
O* + H* → OH*	0.74	-0.73	0.72	-0.31	0.36	-1.89
	(0.80)	(-0.72)	(0.95)	(-0.08)	(0.66)	(-1.59)
OH* + H* → H_2O*	0.62	-0.33	0.39	-0.58	0.48	-0.92
	(0.66)	(-0.28)	(0.58)	(-0.38)	(0.63)	(-0.83)
OH*+OH* → H_2O* + O*	0.27	-0.08	0.00	-0.35	0.25	0.23
	(0.52)	(0.43)	(0.00)	(-0.30)	(0.31)	(0.76)

[a]*The reported activation energy barrier for H_2 dissociation on Ag(111) is from Xu et al.*[162]

O_2* → O*+O*

The minimum energy path for direct O_2* dissociation begins with O_2* in its minimum energy state (t(Pd)-t(Pd), BE = -0.60 eV). The dissociation proceeds with stretching of the O-O bond above an f(2Pd, Ag) site, such that each O atom is near a Pd-Ag bridge site at the transition state (Figure 5.3). This geometry of the transition state is in agreement with experiments conducted on

$Pd_{67}Ag_{33}$(111), which suggest that O_2 dissociation requires at least two neighboring Pd atoms.[163] The O-O bond length at the transition state is 1.98 Å. The two O* then settle at neighboring h(Pd, 2Ag) sites, an intermediate stable state along the reaction pathway, before diffusing to the most stable final state with both O* at neighboring f(2Pd, Ag) sites. The activation energy barrier for this O-O bond-breaking step is 1.06 eV and the reaction energy is 0.75 eV (endothermic). This step has a lower barrier on Pd(111) (E_A = 0.84 eV) and a higher barrier on Ag(111) (E_A = 1.22 eV). However, the step is more endothermic on PdAg(110) than on either Pd(111) (ΔE = -0.67 eV) or Ag(111) (ΔE = 0.43 eV). The minimum energy path for direct O_2* dissociation on PdAg(110) differs from that on Pd(111) and Ag(111), where O-O bond scission occurs above an hcp site. As a result, whereas the geometry of the most stable, co-adsorbed final state on all three surfaces is identical (2 fcc sites), the pathway on PdAg(110) goes through the intermediate hcp-hcp (h(Pd, 2Ag)-h(Pd, 2Ag)) state. This h(Pd, 2Ag) site for co-adsorbed O* (0.5 ML) on PdAg(110) is 1.14 eV less stable than the most stable f(2Pd, Ag) site.

$$\boldsymbol{O_2* + H* \rightarrow OOH*}$$

In the initial state for peroxyl formation, O_2* and H* are co-adsorbed in their most stable binding sites at infinite separation, t(Pd)-t(Pd) and f(2Pd, Ag), respectively. As the step proceeds, the OO-H bond forms at a t(Pd) site (Figure 5.3). In the final state of the minimum energy path the OOH* intermediate is at a b(Pd, Ag)-t(Pd) site, which is 0.10 eV less stable than the most stable b(2Pd)-t(Ag) site. The activation energy barrier for this step is 0.75 eV and the reaction energy is -0.19 eV. This step is more energetically favorable on Ag(111) (E_A = 0.20 eV, ΔE = -1.06 eV). On Pd(111), the activation barrier for the peroxyl formation elementary step is lower (E_A = 0.63 eV) than that on PdAg(110), but the reaction energy is less favorable (ΔE = 0.04 eV).

On Ag(111) this step begins with O_2 in the gas phase, as O_2 does not bind on the Ag(111) surface in the presence of 0.25 ML H*.

OOH* → OH* + O*

The minimum energy pathway for breaking the O-O bond in OOH* begins with OOH* in the b(Pd, Ag)-t(Ag) site, which is 0.17 eV higher in energy than the most stable adsorption site, b(2Pd)-t(Ag). The bond-breaking occurs around the Pd atom separating the OH* and O* in the final state (Figure 5.3). The elementary step ends with OH* and O* in the b(Pd, Ag) and f(2 Pd, Ag), respectively. This final state is 0.13 eV higher in energy than the most stable co-adsorbed final state, in which both adsorbates occupy f(2Pd, Ag) sites. The activation energy barrier and reaction energy for this step, 0.26 eV and -0.98 eV, respectively, falls between the respective values on Pd(111) and Ag(111). This step is more energetically favorable on Pd(111) (E_A = 0.06 eV, ΔE = -1.18 eV) and less favorable on Ag(111) (E_A = 0.41 eV, ΔE = -0.61 eV).

OOH* + H* → HOOH*

The minimum energy pathway for OOH* hydrogenation to H_2O_2 requires the OOH* to first diffuse, via a rotation, from the most stable b(2Pd)-t(Ag) site to the b(Pd, Ag)-t(Pd) site. H* begins in its most stable f(2Pd, Ag) site. The H* approaches the OOH* from the same side as the H atom in OOH*, resulting in a cis configuration of the complex at the transition state (Figure 5.3). Interestingly, this contrasts with the trans configuration of the transition state complex in the same step on Pd(111) and Ag(111), where the H approaches OOH* from the opposite side of the H in OOH*. The barrier for this step, 0.68 eV, is higher than the barrier on Pd(111), 0.40 eV, and on Ag(111), 0.60 eV. The final state for HOOH* in this step is one of the two isoenergetic most stable states, t(Pd)-f(2Pd, Ag), and is similar to the most stable configuration of HOOH* on

Pd(111) and Ag(111). This step, with a reaction energy of -0.29 eV on PdAg(110), is slightly less exothermic on Pd(111) (ΔE = -0.25 eV) and significantly more exothermic on Ag(111) (ΔE = -0.78 eV).

HOOH* → OH* + OH*

Beginning in the most stable t(Pd)-f(2Pd, Ag) site the O-O bond in HOOH* breaks across a b(Pd, Ag) site (Figure 5.3). At the transition state, the H in both OH* groups are directed toward neighboring Pd atoms. The activation energy barrier for this step, 0.20 eV, is comparable to that on Pd(111) and Ag(111), 0.19 eV and 0.18 eV, respectively. The step proceeds, following the transition state, with both OH* groups rotating into their most stable co-adsorbed configuration at neighboring b(Pd, Ag) sites. The final NEB co-adsorbed state is analogous to that on Ag(111), but differs from the 0.5 ML OH* state on Pd, where both OH* occupy top sites. With a reaction energy of -1.83 eV, this step is the most exothermic elementary step considered in this study. This step is similarly a highly exothermic step on Pd(111) (ΔE = -1.39 eV) and Ag(111) (ΔE = -2.06 eV).

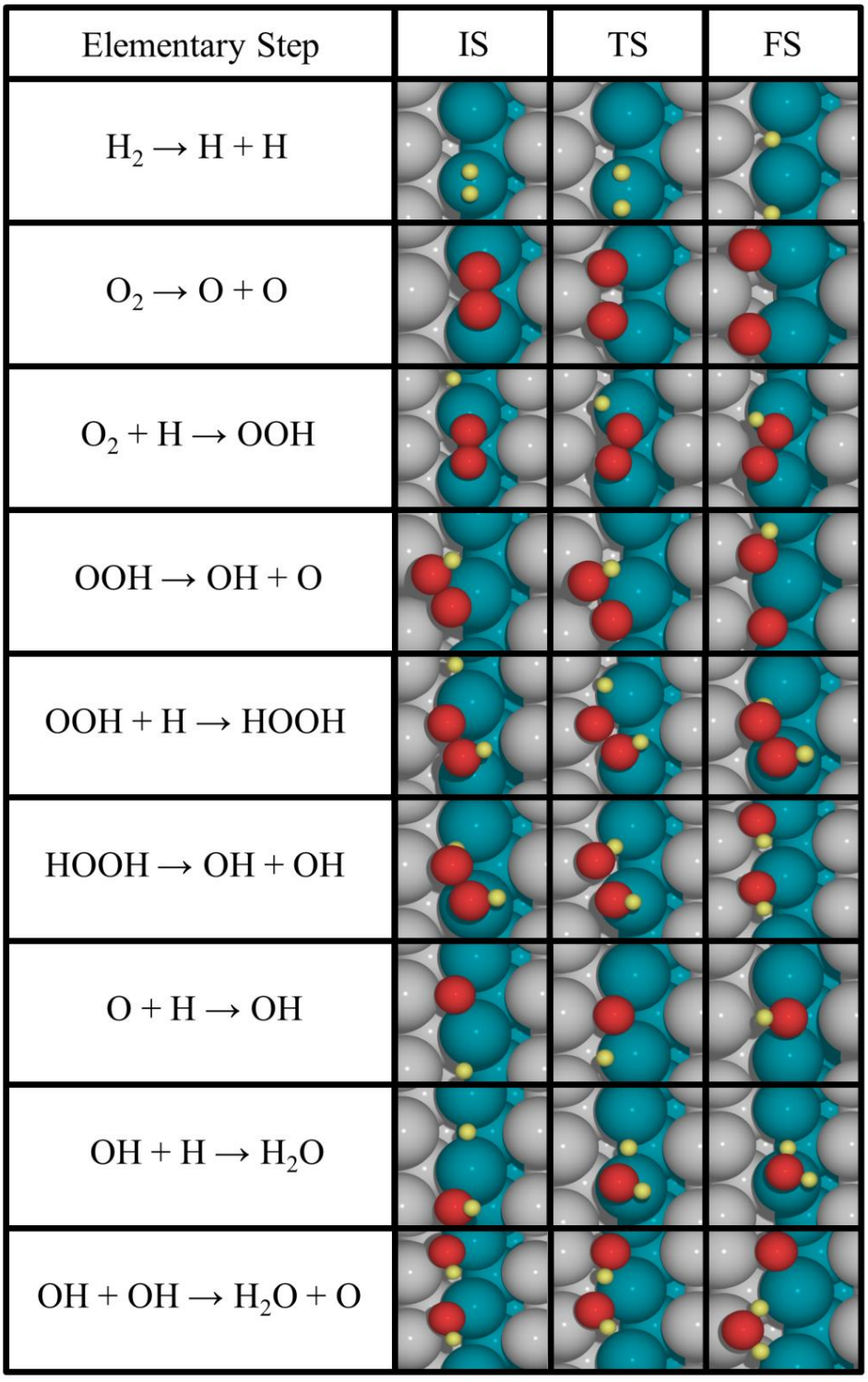

Figure 5.3 The configurations of the calculated initial state (IS), transition state (TS) and final state (FS) of the elementary steps on PdAg(110). IS and FS depict the state used in the NEB calculation. Yellow, red, grey and green spheres represent H, O, Ag and Pd, respectively.

$$O^* + H^* \rightarrow OH^*$$

Hydroxyl formation from O* and H* begins with O* and H* in neighboring f(2Pd, Ag) sites. This initial state is analogous to that on Pd(111), but differs from Ag(111) where H* occupies an hcp site in the most stable co-adsorbed configuration. The transition states on all three surfaces are quite similar, with the H* at an hcp site and the O* in an fcc site (Figure 5.3). Following formation of the O-H bond, OH* is in an intermediate stable b(2Pd) state with the H oriented above an f(2Pd, Ag) site. The OH* must then rotate to reach its final, most stable state, f(2Pd, Ag), with the H oriented above a b(2Pd) site. In both the intermediate minimum energy state and the final, most stable state for OH*, the O-H bond is tilted with respect to the surface plane. The activation barrier on PdAg(110) (E_A = 0.74 eV) is similar to the barrier on Pd(111) (E_A = 0.72 eV), despite the increased exothermicity on PdAg(110) (ΔE = -0.73 eV) compared with Pd(111) (ΔE = -0.31 eV). On Ag(111), this step is significantly more exothermic (ΔE = -1.89 eV) and has a much lower barrier (E_A = 0.36 eV).

$$OH^* + H^* \rightarrow H_2O^*$$

In the initial state for water formation from OH* and H* the adsorbates are in their most stable co-adsorbed configuration: OH* occupies an f(2Pd, Ag) site and H* occupies the neighboring b(2Pd) site. In contrast, on both Pd(111) and Ag(111), the co-adsorbed initial state consists of OH* at a top site and H* at an fcc site. On PdAg(110), at the transition state, the OH* is at a t(Pd) site next to the H* (Figure 5.3). In the final state H_2O* is at its most stable, t(Pd) site. The activation energy barrier is 0.62 eV and the reaction energy is -0.33 eV. This step is less energetically favorable on PdAg(110) than on either Pd(111) or Ag(111); it has a higher barrier and is less exothermic on PdAg(110). The activation energy barrier and reaction energy on Pd(111) are 0.39 eV and -0.58 eV and on Ag(111) are 0.48 eV and -0.92 eV, respectively.

$$OH^* + OH^* \rightarrow H_2O^* + O^*$$

On PdAg(110), the preferential sites for co-adsorbed OH* at 0.5 ML coverage are neighboring b(Pd, Ag) sites. This state is the initial state in the minimum energy path for hydroxyl disproportionation to form H_2O* and O*. At the transition state, one of the OH* has shifted to an f(2Pd, Ag) site closer to the OH* at the neighboring b(Pd, Ag) site (Figure 5.3). This transition state is similar to that found on Ag(111). In the final state, H_2O* and O* are co-adsorbed on PdAg(110) with the H_2O at a t(Ag) site and the O* at an f(2Pd, Ag) site. The activation energy barrier on PdAg(110) is 0.27 eV, similar to the barrier on Ag(111), 0.25 eV. This step is more exothermic on PdAg(110), with a reaction energy of -0.08 eV, compared to the endothermic reaction energy of 0.23 eV on Ag(111). In contrast, this step is spontaneous (E_A = 0 eV) and exothermic (ΔE = -0.35 eV) on Pd(111).

5.3.3 Potential Energy Surfaces

The elementary steps described can be combined to form one dissociative and two associative oxygen reduction reaction mechanisms. The *dissociative* path involves the direct dissociation of O_2 after its adsorption, followed by two hydrogenation steps to yield H_2O. The first associative pathway, the *peroxyl* path, involves the hydrogenation of O_2* to OOH*, followed by its dissociation to O* and OH*, and subsequent hydrogenation of these species to produce H_2O. In the second associative path, the *peroxide* path, O_2* is hydrogenated to OOH* which then undergoes a second hydrogenation to form HOOH*. The HOOH* can then either desorb (making this the selective pathway for the direct synthesis of hydrogen peroxide) or dissociate to yield two OH*. These two OH* species can then undergo a disproportionation step to form H_2O* and O*. To complete the catalytic cycle, the O* can undergo two hydrogenation steps to form H_2O. The reaction between HOOH* and H* to form H_2O and OH* is an alternative peroxide

decomposition step. Li et al. included this elementary step in their study of hydrogen peroxide decomposition on Pd(111) and found that the high activation barrier for this step made it very unfavorable compared with direct decomposition of HOOH*.[144] In this study, all attempts to model this step converged to 2OH* + H*, suggesting that peroxide hydrogenation and dissociation to form H_2O and OH* is not an elementary step on PdAg(110). Ford et al. considered the hydrogenation of HOOH* to HOOHH*, but did not find this to be a stable intermediate on any of the five monometallic sufaces studied, including Pd(111) and Ag(111).[141] The energetics associated with the aforementioned competing mechanisms are shown in the complete potential energy surface (PES) for oxygen reduction on PdAg(110) in Figure 5.4.

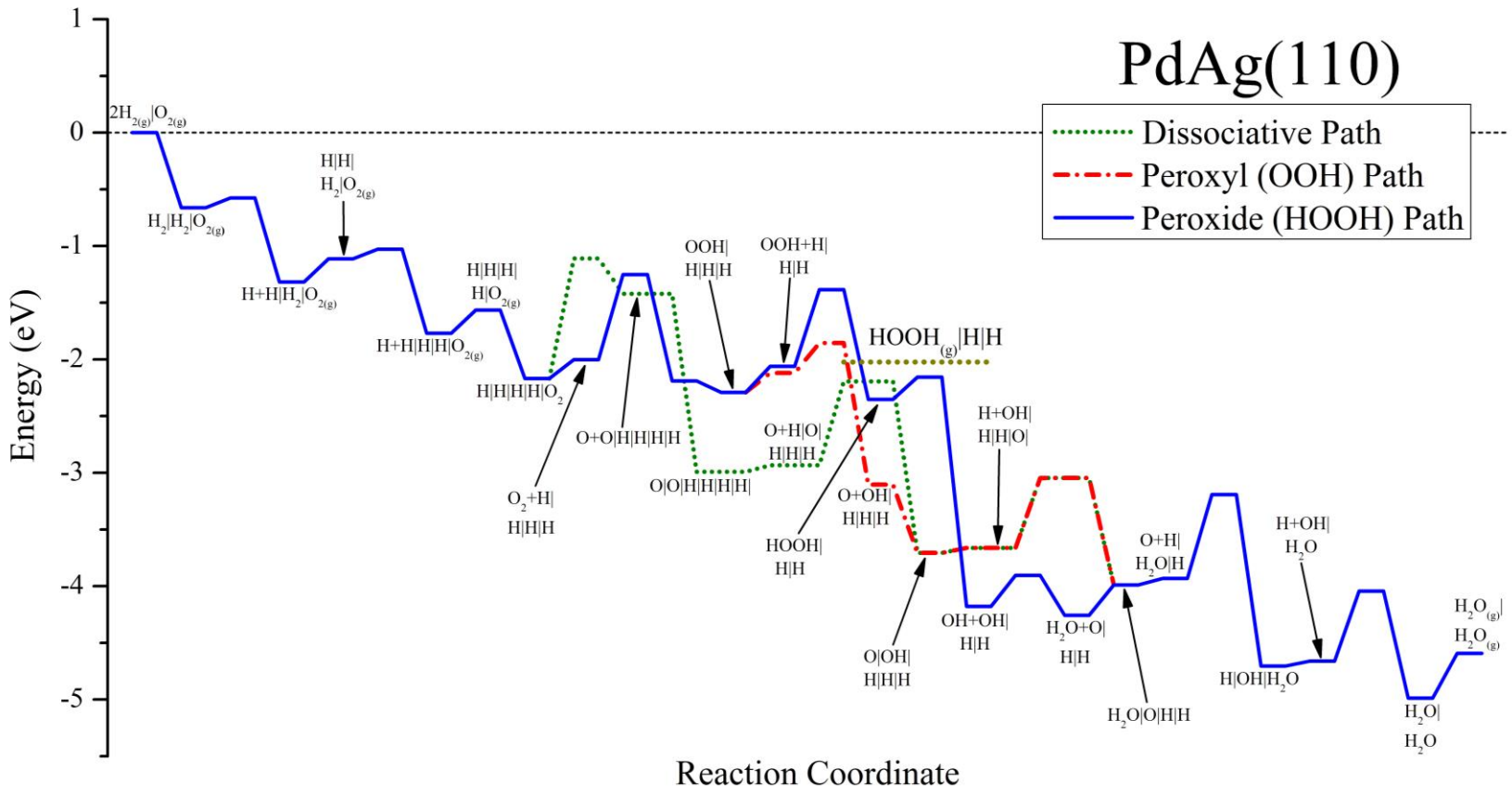

Figure 5.4 The 2D Potential energy surface diagram of the hydrogen-oxygen reaction via the dissociative, peroxyl and peroxide mechanisms on PdAg(110). Zero-energy corresponds to the energy of two H_2 and one O_2 in the gas phase. All non-gas-phase states are adsorbed, but the * is omitted for brevity. Adsorbates connected by "+" are co-adsorbed; those connected by "|" are at infinite separation.

The transition state energy for the direct dissociation of O_2* is higher in energy than the hydrogenation of O_2* to form OOH*, suggesting that based on the PES an associative path should be preferred on PdAg(110). All steps following the O-O bond breaking step in the dissociative path are energetically easier than the O_2* dissociation step, indicating that this step is key in determining the selectivity between the associative paths and the dissociative path. In particular, this step has the highest barrier of any step in all three mechanisms. The associative paths will also compete with O_2* desorption, which is energetically more favorable by 0.15 eV compared with O_2* hydrogenation. Along the associative paths, peroxyl formed via O_2* hydrogenation can either dissociate to form OH* and O* or undergo hydrogenation to form HOOH*. On PdAg(110), the O-OH* dissociation reaction has a significantly lower barrier (E_A = 0.26 eV) and is much more exothermic (ΔE = -0.98 eV) than the competing hydrogenation step (E_A = 0.68 eV, ΔE = -0.29 eV). Dissociation of OOH* eventually leads to H_2O. Following the PES along the peroxide pathway, despite the fact that this path appears to be energetically less favorable, results in the formation of HOOH* that is highly susceptible to decomposition to produce two OH*. The barrier for HO-OH* dissociation is only 0.20 eV and this is the most exothermic step in all three mechanisms. The desorption energy of HOOH* is 0.33 eV, which is 0.13 eV higher than the energy required to dissociate HOOH*, further demonstrating that even if HOOH* is produced on PdAg(110) it is unlikely to desorb as a gas phase product; it will rather decompose. Thus, based on the PES the minimum energy path for the hydrogen-oxygen reaction on PdAg(110) leads to water formation rather than H_2O_2, and H_2O production likely proceeds through the associative, peroxyl, mechanism.

A comparison of the overall PES on PdAg(110) and those on Pd(111) and Ag(111)[141] reveals that on all three surfaces hydrogenation of O_2* is more favorable than direct dissociation. Along the associative paths, the energetics of peroxyl hydrogenation and peroxyl dissociation can therefore be compared to predict the relative selectivity toward peroxide versus water on all three surfaces. As shown in Figure 5.5, on PdAg(110), Pd(111) and Ag(111) the barrier for HOOH* formation via OOH* hydrogenation is 0.47 eV, 0.55 eV, and 0.31 eV higher than the barrier for OOH* dissociation, respectively. Thus, although alloying with Ag decreased the barrier for OOH* dissociation, the relatively small decrease combined with a slight increase in the barrier for OOH* hydrogenation resulted in an overall decrease in the predicted H_2O_2 selectivity. Based on this key selectivity parameter, Ag(111) is expected to display the highest selectivity toward H_2O_2, though the selectivity may still be quite low due to facile decomposition of any H_2O_2 formed.[164, 165] This is a particularly useful comparison as the magnitude of the barriers for H_2O_2* decomposition and the desorption energies are similar on all three surfaces.

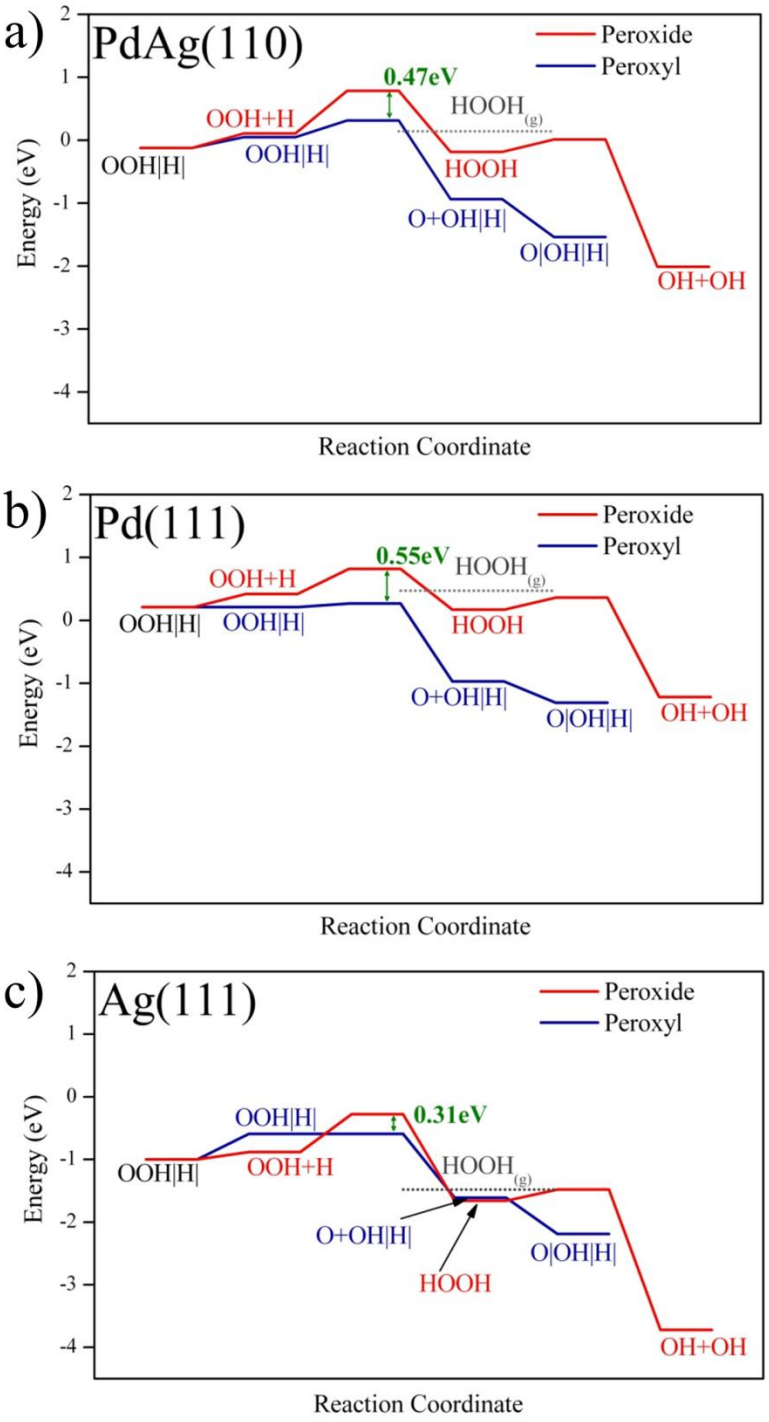

Figure 5.5 The 2D potential energy surface for the selectivity determining steps along the two associative pathways: peroxide path (red) and peroxyl path leading to water (blue). The value reported in green indicates the difference between the transition state energy for peroxyl hydrogenation to peroxide and peroxyl dissociation to O+OH. All species indicated are adsorbed on the metal surface. Adsorbates connected by "+" are co-adsorbed; those connected by "|" are at infinite separation.

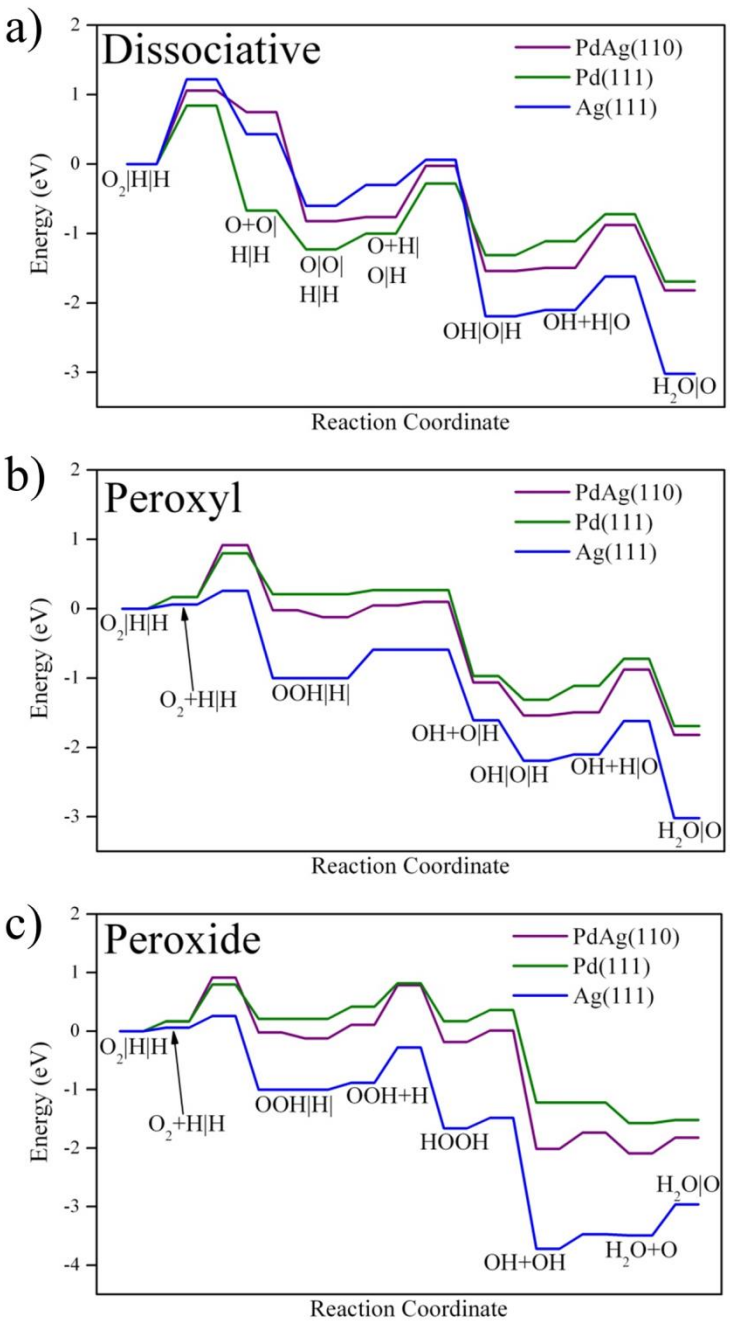

Figure 5.6 The 2D Potential energy surface for the oxygen reduction reaction on PdAg(110), Pd(111) and Ag(111) via the a) dissociative b) peroxyl and c) peroxide path. The potential energy surfaces include only the section along the reaction coordinate in Figure 5.4 that determines selectivity. All species indicated are adsorbed on the metal surface. Adsorbates connected by "+" are co-adsorbed; those connected by "|" are at infinite separation.

To compare the reactivity of PdAg(110), Pd(111) and Ag(111), the PES for each of the dissociative, peroxyl and peroxide pathways, generated using the data on Pd(111) and Ag(111) from Ford et al.,[141] are shown in Figure 5.6a, b and c, respectively. Inspection of the PESs shows that while the PdAg(110) PES generally falls between that of monometallic Pd(111) and monometallic Ag(111), the energetics along each of the three pathways on PdAg(110) follow Pd(111) more closely. This is in agreement with the observation, throughout the reported results, that all adsorbates and transition states on PdAg(110) generally lie closer to the Pd atoms of that surface. Specifically, both of the associative paths on PdAg(110) and Pd(111) are quite similar.

Table 5.4 d-band center (εd) of surface atoms at various sites in PdAg(110), Pd(111), Pd(100), Pd(211), Ag(111) and Ag(211).

Surface	**Site**	**ε_d (eV)**
Pd(111)	Terrace	-1.82
Pd(100)	Terrace	-1.73
Pd(211)	Step edge	-1.71
Pd(211)	Terrace	-1.88
Pd(211)	Step foot	-1.98
Ag(111)	Terrace	-4.12
Ag(211)	Step edge	-4.09
Ag(211)	Terrace	-4.16
Ag(211)	Step foot	-4.22
PdAg(110)	Pd-terrace	-1.68
PdAg(110)	Ag-terrace	-3.63

To further explore similarities and differences in reactivity between PdAg(110), Pd(111), and Ag(111), we calculated the d-band center (ε_d) of the Pd and Ag surface atoms in PdAg(110), and several facets of monometallic Pd and Ag (Table 5.4). The d-band center of Pd in PdAg(110) (ε_d = -1.68 eV) shifts up relative to that of monometallic Pd(111) (ε_d = -1.82 eV). Likewise, the d-band center of Ag in PdAg(110) (ε_d = -3.63 eV) is higher than that in monometallic Ag(111) (ε_d = -4.12 eV). This upshift of the d-band center in Ag is somewhat surprising, as alloying a noble metal with a transition metal generally results in loss of charge by the noble metal, and thus, a downshift in the d-band center. It has been previously demonstrated that in PdAg alloys, both Pd and Ag gain *d* and lose non-*d* (*s* and *p*) charge.[139, 166] The charge loss in Ag is only partially compensated by d-charge gain, resulting in the expected overall loss of charge despite the upshift of the d-band center. The higher lying d-band centers of Pd and Ag correspond to an increase in the reactivity of the Pd and Ag atoms in PdAg(110) compared to the respective atoms' reactivity in their monometallic close-packed surface. Comparison of the shift of the d-band center for Pd versus Ag indicates that alloying Pd and Ag has more significantly altered the reactivity of the Ag atoms. In fact, if one compares the d-band center of the Ag atoms in the PdAg(110) alloy with the d-band center of step edge atoms on the (211) facet of Ag, the increased reactivity exceeds even under-coordinated step sites of Ag. Further, the significantly higher-lying d-band center of the Pd atoms in PdAg(110) compared to the Ag atoms in PdAg(110) indicates that the Pd surface atoms should be much more reactive than the Ag atoms. Comparison of the d-band center of the Pd atoms in PdAg(110) with the d-band center of Pd atoms in the more open (100) and stepped (211) monometallic Pd surfaces shows that the d-band center of Pd in PdAg(110) is quite similar to that of the under-coordinated Pd atoms located at the step sites in Pd(211). Inspection of the preferred adsorption sites (Figure 5.2) and elementary step transition state

geometries (Figure 5.3) demonstrates that the surface chemistry not only prefers to occur near Pd atoms, but also has a preference for the side of the Pd atoms where the fcc sites are coordinated by two Pd atoms, as opposed to two Ag atoms. The preference of adsorbates and co-adsorbates to occupy fcc sites coordinated by two Pd atoms rather than two Ag atoms is a result of the higher d-band center of the Pd atoms. The average d-band center for three-fold sites coordinated by two Pd atoms and one Ag atom is -2.33 eV whereas the average d-band center of three-fold sites coordinated by two Ag atoms and one Pd atom is -2.98 eV. Since the preferred initial and final states for reactants, intermediates and products lie in these sites, the surface reactions generally proceed in the same region of the surface. Thus, the Pd atoms in PdAg(110) behave like 1D arrays of more active surface sites, illustrated in Figure 5.7, dominating the surface chemistry, similar to under-coordinated step sites.[167] In essence, the chemistry occurring on the bimetallic PdAg(110) surface has a dimensionality between that on typical monometallic surfaces (2D chemistry) and the 0D, noncontiguous surface chemistry observed, for example, by Chen et al. for acetoxylation of ethylene to vinyl acetate on surfaces containing Pd monomers surrounded by Au.[168] Another example of 1D surface chemistry has been recently described by Zhong et al.[169] for the polymerization of linear alkanes in 1D channels on the reconstructed Au(110) surface. However, in the case presented here the anisotropy of the surface, facilitating the 1D surface chemistry, is due to the bimetallic composition rather than the atomic scale structure of the surface.

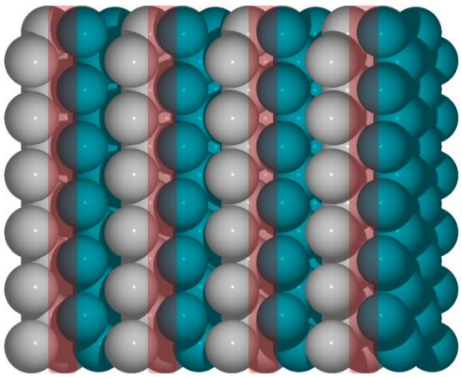

Figure 5.7 The (110) facet of PdAg: Pd (green spheres) and Ag (grey spheres). The regions shaded in red indicate the 1D arrays of active sites on the bimetallic surface.

It is likely that changes in the relative elemental surface composition (Pd:Ag) would create a more significant variation between the three PES's discussed in this work. In PdAg alloys under vacuum, it has been shown that Ag atoms prefer to segregate to the surface creating a surface that is almost exclusively dominated by Ag.[170-172] However, the presence of surface adsorbates, for example H* or O*, can induce surface segregation of Pd due to the stronger interaction between Pd and the adsorbates, as compared with Ag and those adsorbates.[171, 173-175] These two competing factors make it difficult to determine the exact surface composition for PdAg under realistic reaction conditions. The presence of surface ensembles and variations in the composition of the subsurface layers can also alter the local reactivity of Pd surface atoms in PdAg alloys.[139] For this reason, theoretical studies of the direct synthesis of hydrogen peroxide on PdAu have been conducted on a variety of surface compositions.[143, 145, 146] Of these, a surface consisting of Pd monomers surrounded by Au on a Pd substrate best supports the experimental results showing improved H_2O_2 yield and selectivity on PdAu.[145] These Pd monomers are effective at suppressing O-O bond scission in all three reaction intermediates: O_2, OOH and HOOH.[145, 146] Thus, successfully coupling the high reactivity of Pd and the suppression of O-O

bond scission predicted for Au, in the bimetallic alloy to generate a highly selective active site is governed by the particular surface composition. A similar study of Pd monomers surrounded by Ag might therefore yield significantly different results than those presented here.

In closing, we note that more meaningful insights into the reactivity and selectivity of the H_2-O_2 reaction on Pd and Ag compared with PdAg could be obtained from a combined experimental and microkinetic modeling study of the reaction, similar to previous investigations conducted, for instance, for the water gas shift on Cu and Pt[18, 176] and for nitric oxide reduction by hydrogen described in Chapter 8 of this dissertation. Additionally, conclusions drawn here for Pd, Ag and PdAg as catalysts for the H_2-O_2 reaction are based on ¼ ML coverage for all adsorbates. Higher coverages, which may reflect realistic reaction conditions more accurately, may drastically change the reaction energetics and selectivities.[177, 178] In addition, liquid phase direct synthesis of H_2O_2 presents additional mechanistic challenges, including the interaction of intermediates and transition states discussed above with solvent molecules. Insights derived here might serve only as a basis for extending the fundamental understanding needed in more complicated reaction environments.

5.4 Conclusions

A systematic DFT investigation of the hydrogen-oxygen reaction on a model PdAg(110) surface has been performed, allowing for a comparison of the competing reaction mechanisms on the alloy surface with those on Pd(111) and Ag(111). The results show that alloying Pd and Ag shifts the d-band center of both metals in the surface upward, and this effect is more significant for the Ag atoms. The Ag atoms in PdAg(110) are found to be more reactive than even under-

coordinated step edge atoms in Ag(211). Still, the d-band center of the Pd surface atoms remain much higher than the Ag surface atoms. Consequently, the stronger interaction between intermediates and Pd, compared to the relatively weak interaction with Ag, is translated into the preferred location of intermediates and transition states on the alloy surface. In particular, this is demonstrated by the preference of all intermediates to bind at sites which maximize the interaction with the Pd atoms in the alloy surface. The transition states of elementary steps also adopt geometries that maximize coordination with Pd atoms, and thereby the stabilization by Pd. Thus, the Pd atoms in PdAg(110) form 1D arrays of more active surface sites, dominating the surface chemistry, similar to under-coordinated step sites or missing row reconstructions in monometallic Pd surfaces. This results in a potential energy surface for the hydrogen-oxygen reaction on PdAg(110) which can be closely described by the respective potential energy surface on Pd(111). Thus, at a one to one, Pd to Ag, surface composition the effect of Ag on the reaction energetics is fairly small.

The potential energy surface on PdAg(110) shows that direct oxygen dissociation is more difficult than hydrogenation of adsorbed molecular oxygen. Therefore, based on the potential energy surface, the associative paths should be preferred. The associative path leading to hydrogen peroxide production is unlikely to be favorable because hydrogenation of the peroxyl intermediate is much more difficult than its dissociation. Furthermore, any hydrogen peroxide produced is likely to decompose rather than desorb. Based on a comparison of the reaction energetics, Ag(111) is predicted to be more selective toward H_2O_2 than either PdAg(110) or Pd(111), as Ag(111) is most effective at suppressing O-O bond scission. These results suggest that the bimetallic PdAg alloy is unlikely to be an effective catalyst for the direct synthesis of

hydrogen peroxide. However, variations in the alloy composition of PdAg, particularly in the surface layer, may lead to improved H_2O_2 selectivity, as demonstrated in previous studies of PdAu. Thus, the reactivity of PdAg alloys for the direct synthesis of H_2O_2 may merit further experimental and theoretical studies.

Chapter 6 Catalytic Activity of Platinum Monolayer on Iridium and Rhenium Alloy Nanoparticles for the Oxygen Reduction Reaction[i]

6.1 Introduction

In the previous chapter, the homogeneous bimetallic PdAg alloy was investigated for the *gas phase* reaction between H_2 and O_2 for the production of hydrogen peroxide. During the last two decades, considerable research effort has focused on developing improved catalysts for the *electrocatalytic* reduction of oxygen at fuel cell cathodes. Fuel cells are one of the most promising sources of clean energy given their uniquely efficient direct energy conversion and environmentally benign products of their reactions, however, their commercial application as a power source in automobiles and residences has yet to be attained, mainly due to technical and economic barriers. Platinum is the most efficient monometallic catalyst for the oxygen reduction reaction (ORR), however, even Pt catalysts lack sufficient activity due to slow ORR kinetics and stability due to dissolution.[11, 179, 180]

In meeting the challenges involving the high content of Pt and the insufficient activity and stability of existing electrocatalysts, Pt monolayer (Pt_{ML}) electrocatalysts have been developed

[i] Karan, H. I.; Sasaki, K.; Kuttiyiel, K.; Farberow, C. A.; Mavrikakis, M.; Adzic, R. R., *ACS Catalysis* 2012, 2, 817-824. Contributions by C. A. Farberow: 100% of DFT calculations and writing the theoretical section of the manuscript; extensive work on synthesis of the final manuscript with H. I. Karen.

consisting of a single-layer shell of Pt atoms on cores of suitable monometallic or alloy nanoparticles.[181] This concept facilitates the design of catalysts with several unique properties: i) low total Pt content (one monolayer); ii) complete utilization of Pt since all atoms are on the surface; iii) tunable activity and stability due to modification of the geometric and electronic properties of Pt_{ML} induced by various substrates. [182-185] Pt_{ML} electrocatalysts can have mass activities more than an order-of-magnitude higher than that of conventional Pt/C catalysts along with improved stability.[182] Early investigations of this concept demonstrated that the effect of the substrate results in a volcano plot with Pt/Pd(111) closest to the peak, corresponding to the most active surface.[184] Most recent studies using a Pt monolayer approach have involved varying the shape (tetrahedral[186] and nanowires[187]) and morphology (smooth cores[188]) of supporting nanoparticle cores.

Efforts for improving the catalytic properties of Pt and reducing the Pt content in ORR catalysts based on the core-shell approach are exemplified by Pt "skin" catalysts, in which a layer of Pt is formed by surface segregation of Pt in Pt_3Ni alloy,[189] and in some bimetallic dealloyed catalysts.[190] The high activity of the Pt–skin catalyst has been ascribed to the electronic effects of the Ni core.[189] Interesting insight into the role of strain on the catalytic properties were reported for a Pd monolayer deposited at underpotentials (UPD) on several single crystal surfaces in formic acid electrooxidation[191] and the hydrogen evolution reaction.[192]

Applying a Pt monolayer clearly contributes to reducing the cost of catalysts and these catalysts can produce specific activities for the ORR comparable with or higher than conventional Pt electrocatalysts.[181-185, 193] Zhang et al. also reported significantly improved ORR efficiency by depositing a Pt monolayer on a core consisting of non-noble metal (Ni or Co) –

noble metal (Au or Pd or Pt) alloy nanoparticles.[194] In these catalysts, the noble metal shell protected the non-noble metal core from dissolving in acidic electrolyte and improved the catalytic properties of the Pt monolayer by affecting its electronic properties. Xing et al. reported enhanced ORR activity for catalysts prepared with a Pt monolayer shell on a Pd-Au core,[195] while Sasaki et al. reported that Pt monolayer on Ir-Fe core shell nanoparticles showed significantly improved electrocatalytic activity and stability.[196] Most recently Gong et al. reported an improved ORR activity for a Pt monolayer and palladium interlayer on Ir-Co alloy core.[186]

In this chapter, we report a new type of catalyst composed of nanoparticle alloys of iridium and rhenium as the core with either a platinum monolayer or platinum on a palladium interlayer shell deposited on the core. These core metals were chosen because their electron configurations and d-band centers are in the proximity of Pt,[28] they are adequately stable metals with high melting points and high acid and corrosion resistance, and they are priced lower than Pt. The catalysts were characterized and tested for oxygen reduction activity and performance stability, and a density functional theory (DFT) based theoretical study provides a fundamental understanding as to why specific Ir-Re compositions in the core of these catalysts can lead to improved ORR rates.

6.2 Methods

6.2.1 Experimental

The reagents including iridium chloride ($IrCl_3 \cdot xH_2O$, 52.3% metal content), rhenium chloride ($ReCl_3$, 99.9%), copper(II) sulfate pentahydrate ($CuSO_4 \cdot 5H_2O$) and potassium tetrachloroplatinate (K_2PtCl_4) were obtained from Alfa Aesar and Vulcan XC-72R carbon

nanopowder (~60 nm) was obtained from Cabot Corp. Perchloric acid (66-71%) was obtained from Fisher Scientific. Nafion (PFSA Dispersion DE 1020, aqueous solution) from DuPont or 5% lower aliphatic alcohol solution by Aldrich were used for coating over a glassy carbon electrode surface or added into the aqueous catalyst ink. Millipore distilled water (UV Plus with total organic content control) was used to prepare solutions. Research purity grade oxygen gas was obtained from Matheson Tri-Gas and hydrogen and argon gases were obtained from MG Industries and CGI Gas Technologies, respectively.

The reduction of metal halide was carried out at elevated temperatures in a tube furnace. Potentiostats Volta Lab (model PGZ 402) by Radiometer Analytical, S.A. (Lyon, France) and BAS Electrochemical Analyzer 100B were used for electrochemical analyses and copper underpotential deposition (UPD) experiments, respectively. For a rotating disk electrode, Modulated Speed Rotator (Pine Instrument Corp.) was used to control rotation speed. Custom made electrochemical cells were used for routine electrochemical analyses and copper UPD experiments.

The catalyst particles were deposited on a glassy carbon disk (surface area 0.196 cm^2) with a Pt ring (Pine Instruments, Grove City, PA). A leak–free Ag/AgCl reference electrode (Cypress Systems Inc., Kansas) which is stored in 3 M NaCl solution was used with a double-junction reference chamber (BAS). A small platinum flag was used as a counter electrode. All the potentials are reported with respect to a reversible hydrogen electrode (RHE). The electrochemical cell, with 20 mL of 0.1 M $HClO_4$ solution, was purged with argon gas for 20-30 minutes before starting measurements. Oxygen reduction measurements were performed after

purging the cell with research purity oxygen gas for 30-40 minutes to ensure saturation of oxygen in the media. All electrochemical measurements were performed at room temperature.

6.2.2 Catalyst Synthesis and Characterization

The catalyst particles were prepared by mixing desired mole ratios of metals with the carbon nanopowder support. The ratio of the metal mixture to the carbon powder was 3:7 by weight. The aqueous mixture of metal and carbon was sonicated for 30 minutes and then water was evaporated. The dry residue was placed in a quartz boat which was then placed in a glass tube and purged with argon gas for 20 min and then heated at 673 K for one hour under flowing hydrogen gas. The reduced metal catalyst particles were used for subsequent electrochemical analyses and oxygen reduction experiments.

Twenty nanomoles of aqueous mixture of the catalyst particles were sonicated briefly (less than 20 minutes) and 15-20 µL (~0.2 mg/cm^2) of the ink produced was placed on the surface of a glassy carbon ring electrode. The electrode surface was dried under vacuum and then coated by 5 µL of 0.025% Nafion (diluted with distilled water from 5% Nafion solution) and dried under vacuum to evaporate water from the surface. Cyclic voltammograms (CV) of the initial catalysts were taken and then the electrocatalysts were prepared by depositing Pd and/or Pt monolayers on iridium and rhenium alloy substrate by galvanic displacement of underpotentially deposited Cu monolayer by Pd or Pt. This rather straightforward method has been reported elsewhere.[182, 197, 198] Copper UPD was performed in a custom made multiple chamber cell using 50 mM $CuSO_4 \cdot 5H_2O$ in 50 mM H_2SO_4, 1 mM $PdCl_2$ in 50 mM H_2SO_4 and 1 mM K_2PtCl_4 in 50 mM H_2SO_4 solutions. The 50 mM $CuSO_4 \cdot 5H_2O$ in 50 mM H_2SO_4 solution as well as Pd and Pt solutions were purged

by argon gas for 20-30 minutes before starting the Cu UPD and during the displacement experiments.

After the deposition of Pd and Pt monolayers, voltammetry was used to determine the quantity of Pt deposited on the core nanoparticles from the change associated with hydrogen adsorption. Subsequently, kinetic measurements of the ORR were carried out. All electrochemical experiments except oxygen reduction were performed in an Ar gas environment. The catalysts were characterized electrochemically and using X-ray diffraction (XRD), transmission electron microscopy (TEM) and X-ray absorption near edge structure (XANES) spectroscopy. In situ XANES measurements were conducted using an electrochemical cell designed for data acquisition in fluorescence transmission mode. The compartments for the working and counter electrodes were separated by a proton exchange membrane (Nafion 117, DuPont). The experiments were carried out at the beamline X-19A at the National Synchrotron Light Source (NSLS). TEM measurements were performed using JOEL 2100F (STEM/EDX) equipped with a Schottky field emission source operated at 300 KeV, an ultrahigh-resolution objective lens pole piece, an energy dispersive X-ray spectrometer and a post column Gatan imaging filter (GIF). Powder samples were dispersed on a Cu mesh grid coated with a lacey amorphous carbon film.

6.2.3 Density Functional Theory Calculations

Periodic, DFT calculations of OH binding energies on appropriately selected model surfaces were performed with the PW91-GGA exchange-correlation functional using the DACAPO total energy code.[29, 150] The bulk structures of the alloys were determined from the stable ordered phases defined by the Ir-Re phase diagram:[199, 200] Ir_1Re_2 and Ir_1Re_3 were modeled as hexagonal-

close packed (hcp) alloys and Ir_3Re_1 and Ir_5Re_1 were modeled as face-centered cubic (fcc) alloys. For the hcp bulk alloys the calculated optimized lattice constants were 2.77 Å and 2.76 Å and c/a ratios were 1.57 and 1.59 for Ir_1Re_2 and Ir_1Re_3, respectively. The optimized lattice constants for the Ir_3Re_1 and Ir_5Re_1 fcc bulk alloys were 3.86 Å and 3.92 Å, respectively. The closest-packed (111) and (0001) facet of the catalysts were modeled with a $2\sqrt{3}$ x $2\sqrt{3}$ unit cell, corresponding to an adsorbate (OH) coverage of 1/12 ML. The metal slabs consisted of five total layers with the top three layers relaxed and five equivalent layers of vacuum between successive slabs.

6.3 Results and Discussion

6.3.1 Characterization of Ir-Re Alloy Nanoparticles

Carbon supported iridium-rhenium alloy nanoparticles with several different molar Ir:Re ratios (5:1, 3:1, 7:3, 2:1, 1:1, 1:2, 3:7 and 1:3) were prepared by reducing 3:7 mixtures of desired molar ratios of metal chlorides and Vulcan carbon by hydrogen gas at 673 K for one hour. The XRD of the resultant nanoparticles showed broad bands of iridium and rhenium (Figure 6.1), which appear to indicate the amorphous state of these nanoparticles. Iridium in an alloy with rhenium should surface segregate as predicted by a computational study of alloy surface segregation energies.[150] For very small particles (3nm) such a layer may not produce sufficient XRD signal. The peaks for H adsorption and Cu UPD in voltammetry curves are similar to those obtained for Ir nanoparticles, but have no similarity with Re. Thus, voltammetry provides strong support for the surface segregation of Ir.

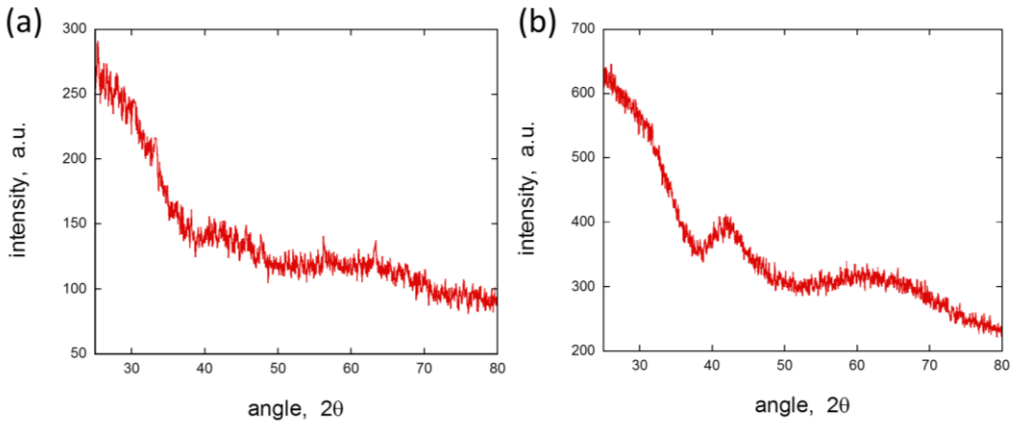

Figure 6.1 XRD pattern of carbon supported (a) IrRe and (b) Ir_3Re_1 nanoparticles synthesized by annealing at 673K in H_2 atmosphere for 1 h.

X-ray absorption spectroscopy (XAS) measurements showed that the metal alloy nanoparticles (1:1 and 7:3 molar Ir:Re ratio) retained the original composition of metals after reducing the metal chlorides (Figure 6.2a, b). The average size of these nanoparticles was 3.3 ± 1 nm based on TEM images (Figure 6.2c).

6.3.2 Pt (Pd) Monolayer Deposition on Ir-Re Nanoparticles

Pt monolayer (Pt_{ML}) or Pd monolayer (Pd_{ML}) plus Pt_{ML} deposition on the carbon-supported Ir-Re nanoparticles were performed by galvanic displacement of a Cu UPD monolayer. This deposition method via Cu UPD has been discussed in detail previously.[181-186] The UPD of Cu on the working electrode was carried out in 50 mM $CuSO_4$ in 50 mM H_2SO_4 at ~100 mV. The electrode was immersed and placed in either 1.0 mM K_2PtCl_4 in 50mM H_2SO_4 or 1.0 mM $PdCl_2$ in 50 mM H_2SO_4 for 3 minutes to deposit a Pt or Pd monolayer by replacing Cu.

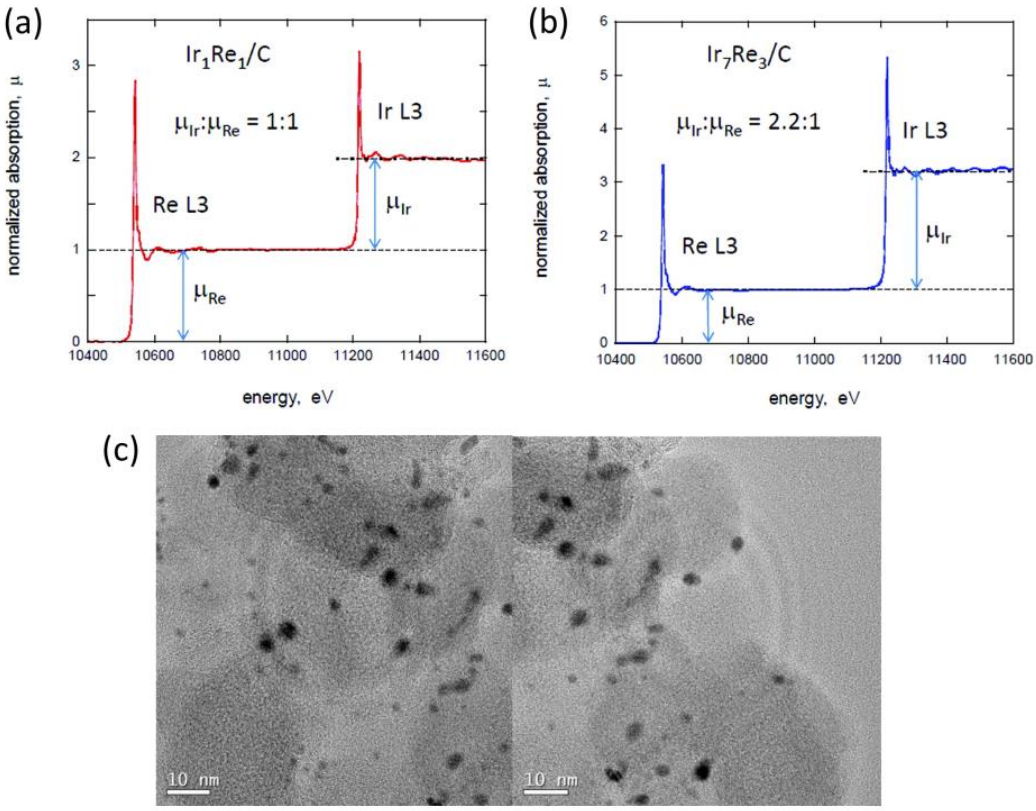

Figure 6.2 XAS results of Re L3 edge (10535 eV) and Ir L3 edge (11215 eV) from (a) Ir_1Re_1/C and (b) Ir_7Re_3/C catalysts prepared by hydrogen reduction of the metal chloride mixtures at 673 K. (c) TEM images of Ir_7Re_3/C catalyst. The average size of the catalyst particle is 2.2-4.4 nm.

Figure 6.3 shows the CVs of the initial Ir_7Re_3/C and Ir_1Re_1/C nanoparticles (dotted line) and after depositing two layers of Pd and a Pt monolayer (solid line), respectively, which clearly indicate Pt monolayer deposition on Ir_7Re_3/C and Ir_1Re_1/C nanoparticle surfaces. The Pt concentrations deposited on carbon supported Ir-Re nanoparticles averaged 2.8 x 10^{-3} mg for Ir_7Re_3 and 1.4 x 10^{-3} mg for Ir_1Re_1. The efficiency of galvanic displacement of Cu UPD monolayer by Pt and the evidence of obtaining one monolayer of Pt (i.e., one-to-one correspondence between Cu coverage and Pt coverage) was verified in earlier publications for properly performed experiments.[193, 201, 202] Pt coverages lower than one monolayer usually result from a partial loss of Cu coverage if the displacement is not O_2-free. Pt coverages greater than

one monolayer may occur if a partial displacement of low-coordination Pd atoms takes place during long exposures to Pt solution.

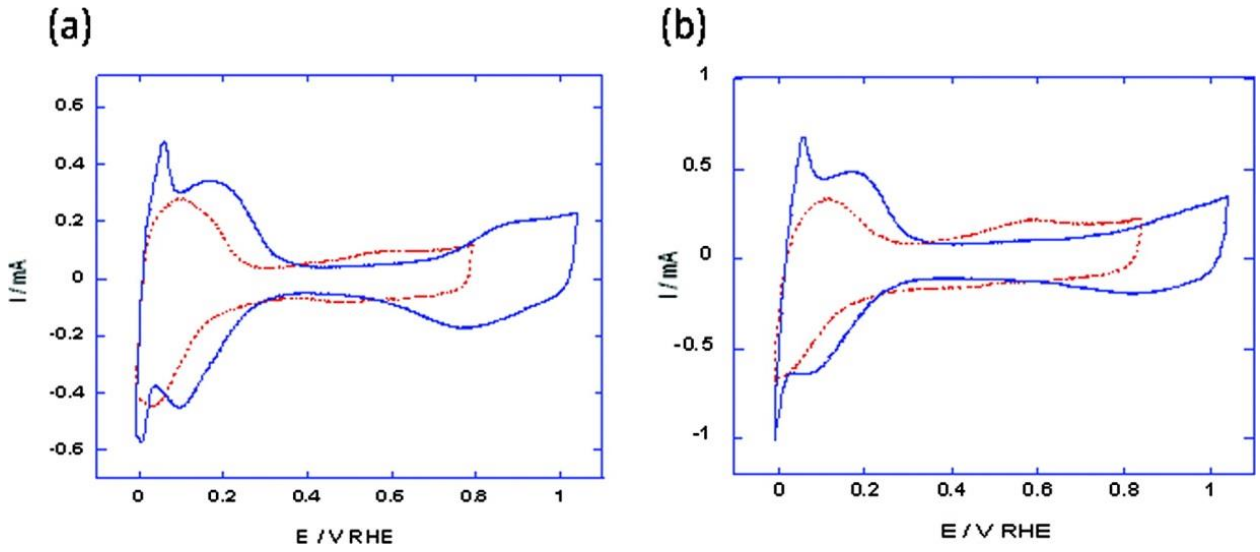

Figure 6.3 Voltammetry curves for (a) Ir_7Re_3/C and (b) Ir_1Re_1/C alloy nanoparticles (dotted red lines) and the same nanoparticles after deposition of two layers of Pd and Pt monolayer (solid blue lines) in deaerated 0.1 M $HClO_4$. Sweep rate: 10 mV/s.

6.3.3 Oxygen Reduction

Table 6.1 summarizes the half-wave potentials of ORR polarization curves of Pt_{ML} or Pd_{ML} and Pt_{ML} shells on different compositions of Ir-Re/C core in oxygen saturated $HClO_4$ at 1600 rpm. The results show that when the Ir:Re mole ratio is approximately 2:1, half-wave potentials of the ORR polarization curves appear to be the highest. To compare the effect of the shell structure on the ORR efficiency, different shell structures were also studied.

Table 6.1 Half-Wave Potentials ($E_{1/2}$) of the ORR on Pt_{ML}, $Pd_{interlayer}$ and Pt_{ML}, and two $Pd_{interlayer}$ and Pt_{ML} for the various mole ratios of Ir:Re/C core compositions

Catalyst	**Ir:Re mole ratio**	**$E_{1/2}$ mV, RHE**		
		Pt_{ML}/Ir-Re/C	Pt_{ML}/Pd_{ML}/Ir-Re/C	Pt_{ML}/Pd 2layers/Ir-Re/C
Ir-Re/C	5:1	837	848	
	3:1	879	857	859
	2.3:1	821	882	888
	2:1	879	890	893
	1:1	802		859
	1:2	765	803	
	1:2.3		831	761
	1:3	812	814	
Pt/C[187]		855		

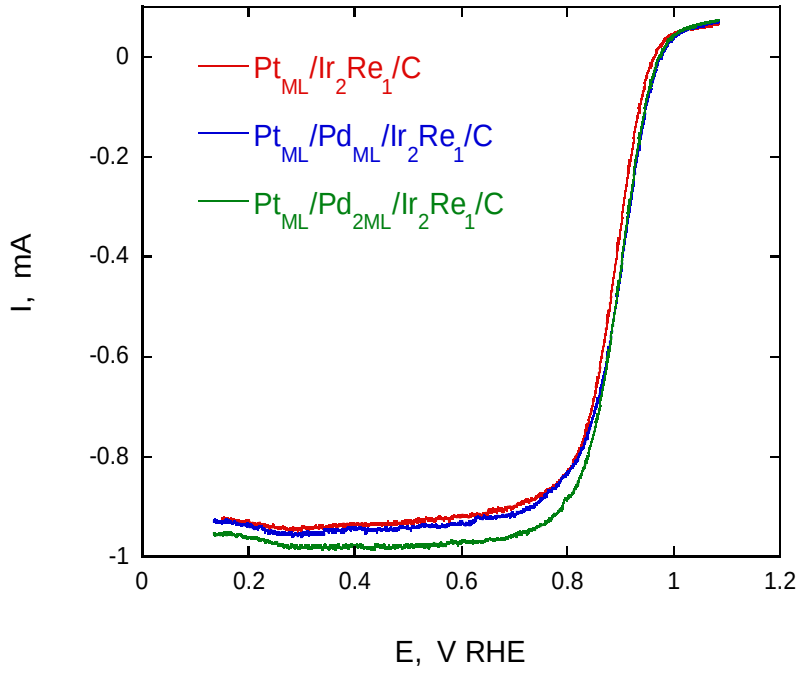

Figure 6.4 Rotating disk electrode measurements of ORR on $Pt_{ML}/Ir_2Re_1/C$, $Pt_{ML}/Pd_{ML}/Ir_2Re_1/C$ and $Pt_{ML}/Pd_{2ML}/Ir_2Re_1/C$ catalysts at 1600 rpm in O_2-saturated 0.1 M $HClO_4$. Sweep rate: 10 mV/s.

Figure 6.4 shows the ORR curves of Pt_{ML}, Pd_{ML} and Pt_{ML}, and 2 layers of Pd and one Pt_{ML} on the Ir_2Re_1 core using a rotating disk electrode (RDE) in oxygen saturated 0.1 M $HClO_4$ solution at 1600 rpm. Significant activity of the electrocatalysts can be inferred from a high onset potential (~1.0 V) of oxygen reduction and high half-wave potentials. The results show that placing a Pd interlayer improves the activity of the catalysts. It is expected that when a Pt_{ML} is directly deposited on Ir-Re core, the Pt atoms will exhibit strain due to lattice compression which adversely affects Pt ORR catalytic activity. It is likely that the excessive contraction comes from an Ir surface, formed by its surface segregation, as discussed above (see 6.3.1 Characterization of Ir-Re Alloy Nanoparticles). The Pd interlayer moderates the contraction of the Pt monolayer and precludes the adverse effect on the catalytic activity of Pt.

Figure 6.5a shows the ORR measurements on Ir_2Re_1 catalyst coated with a monolayer of Pt using a RDE in an O_2-saturated 0.1 M $HClO_4$ solution at different rotation speeds (400-3025 rpm) at a 10 mV/sec sweep rate. Figure 6.6a shows similar experimental results with the Ir_2Re_1/C catalyst coated with a Pd_{ML} and then a Pt_{ML}. The Pt concentrations deposited on the carbon supported Pt_{ML}/Ir-Re and Pt_{ML}/Pd_{ML}/Ir-Re nanoparticles were 8.2 μg/cm^2 and 7.35 μg/cm^2, respectively.

Koutecky-Levich plots for Pt_{ML}/Ir_2Re_1/C and $Pt_{ML}/Pd_{ML}/Ir_2Re_1$/C are shown in Figure 6.5b and Figure 6.6b based on ORR polarization data obtained in Figure 6.5a and Figure 6.6a, respectively. The linearity and parallelism of these plots indicate first order kinetics with respect to the concentration of molecular oxygen.[11, 182, 203] To obtain Pt mass activities (A/mg), the kinetic currents for ORR were determined from the intercepts on 1/j at $\omega^{-1/2}$ equal zero.

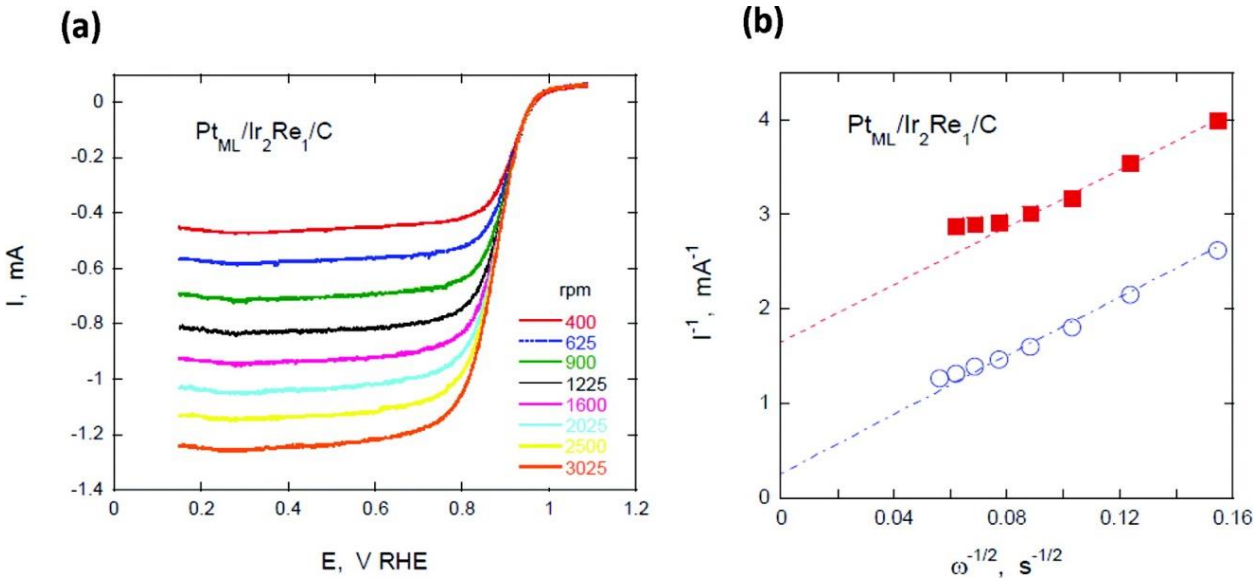

Figure 6.5 (a) RDE measurements of the ORR on $Pt_{ML}/Ir_2Re_1/C$ catalyst as a function of rotation rate. (b) Koutecky–Levich plot (I^{-1} vs $\omega^{-1/2}$) for $Pt_{ML}/Ir_2Re_1/C$ at potentials 0.90 V (■) and 0.85 V (o) based on the data obtained in Figure 6.5a in an O_2-saturated 0.1 M $HClO_4$. Sweep rate: 10 mV/s.

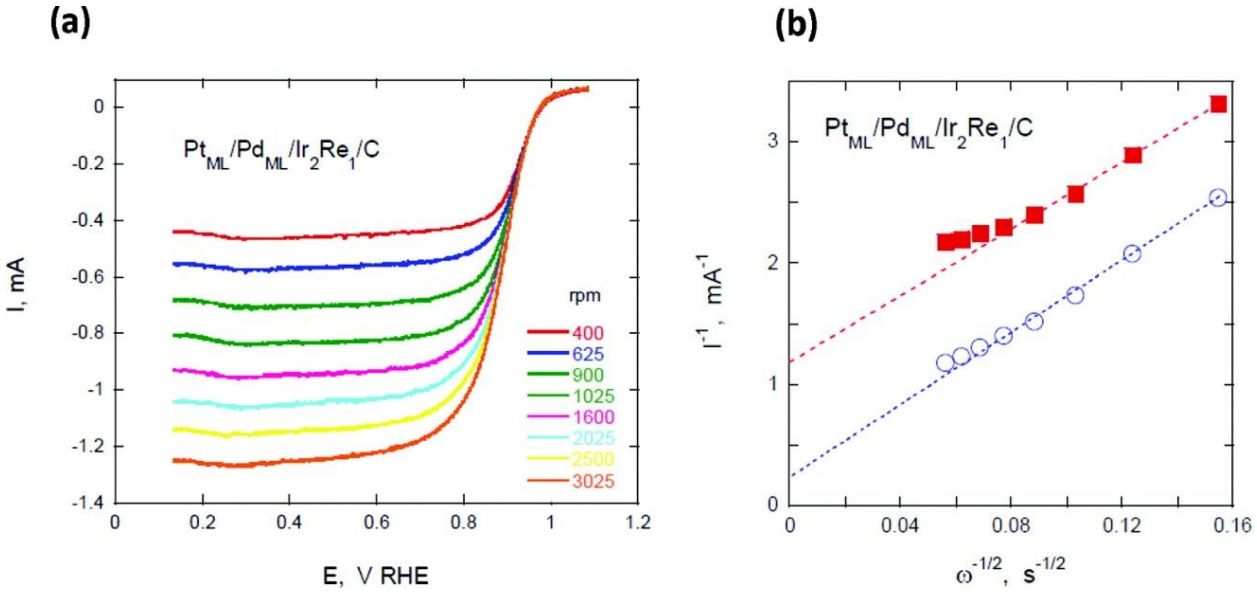

Figure 6.6 (a) RDE measurements of ORR on $Pt_{ML}/Pd_{ML}/Ir_2Re_1/C$ catalyst as a function of rotation rate. (b) Koutecky–Levich plot for $Pt_{ML}/Pd_{ML}/Ir_2Re_1/C$ at potentials 0.90 V (■) and 0.85 V (o) based on the data obtained in Figure 6.6a in an O_2-saturated 0.1 M $HClO_4$. Sweep rate: 10 mV/s.

Table 6.2 shows Pt mass activities (A/mg) and platinum group metal (PGM) mass activities (A/mg) of different molar compositions of Ir-Re catalysts with Pt_{ML}, Pt_{ML} and one Pd interlayer or Pt_{ML} and two Pd interlayers. In these studies, the Ir_2Re_1 core composition showed the highest Pt and PGM mass activities for all three overlayer structures. The Pt and PGM mass activities of $Pt_{ML}/Ir_2Re_1/C$ and $Pt_{ML}/Pd_{ML}/Ir_2Re_1/C$ are 0.38 A/mg, 0.12 A/mg and 0.60 A/mg, 0.18 A/mg at 0.9 V/RHE, respectively. As discussed previously, a Pd interlayer on Ir_2Re_1/C core enhanced the Pt mass activity of the catalysts compared to that of the catalyst without the interlayer. An illustration of the core–shell structure of Ir_2Re_1 cores with different shells and a comparison of their mass activities are shown in Figure 6.7. These catalysts have higher Pt mass activities than that often observed for commercial Pt/C catalyst.[201]

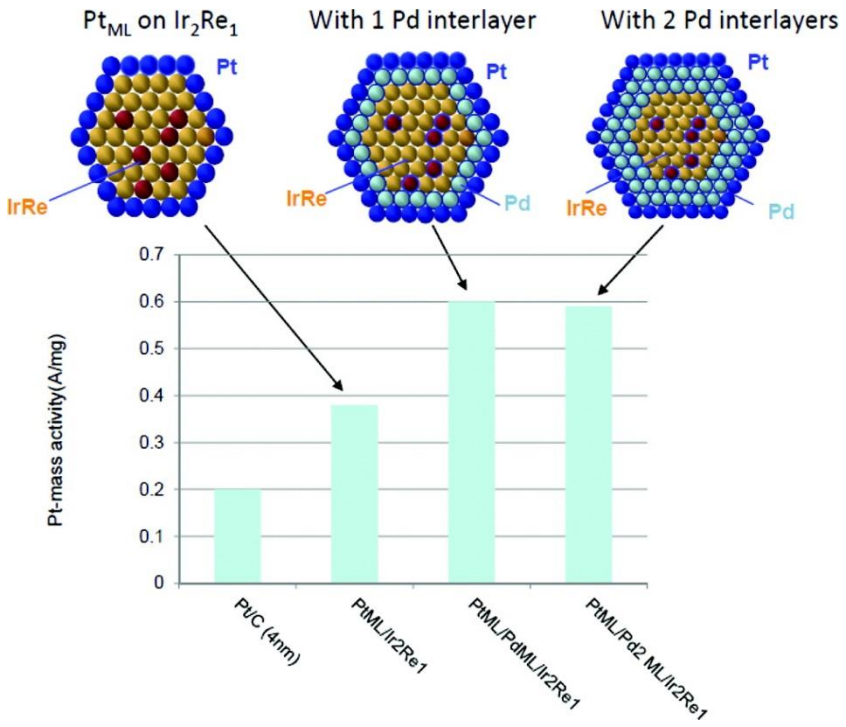

Figure 6.7 Comparison of Pt mass activities for an Ir_2Re_1/C core with different shells (Pt_{ML}, Pt_{ML} and Pd_{ML}, and Pt_{ML} and Pd_{2ML}). Corresponding models of cross sections of nanoparticles are given.

Table 6.2 Platinum mass, platinum group metal (PGM) mass and specific activities of Pt_{ML}, Pt_{ML} and one Pd interlayer, and Pt_{ML} and two Pd interlayers at 0.9 V/RHE for the various mole ratios of the Ir-Re/C core

Catalyst	Pt Mass Activity(A/mg)	PGM Mass Activity(A/mg)	Specific Activity ($\mu A/cm^2$)
Ir_5Re_1/C			
Pt_{ML}	0.19	0.05	160
Pt_{ML}/Pd_{ML}	0.36	0.1	
Ir_3Re_1/C			
Pt_{ML}	0.35	0.11	200
Pt_{ML}/Pd_{ML}	0.45	0.14	
Ir_7Re_3/C			
Pt_{ML}/Pd_{2ML}	0.44	0.13	201
Ir_2Re_1/C			
Pt_{ML}	0.38	0.12	161
Pt_{ML}/Pd_{ML}	0.60	0.18	274
Pt_{ML}/Pd_{2ML}	0.59	0.18	246
Ir_1Re_2/C			
Pt_{ML}	0.16	0.05	180
Pt_{ML}/Pd_{ML}	0.43	0.13	

6.3.4 Density Functional Theory Calculations

The generally accepted four-electron transfer mechanism of oxygen reduction involves O-O bond breaking and O-H bond formation at the catalyst surface. The most effective catalyst is expected to bind oxygen strongly enough to break the O-O bond, while binding the OH group only modestly so that OH removal from the catalyst surface by water elimination is also reasonably facile.[29, 201] Based on DFT calculations, Nilekar and Mavrikakis investigated correlations between metal d-band center energy or OH binding energy and experimentally determined kinetic currents of electrocatalysts for ORR.[204] Plotting the measured kinetic currents

of electrocatalysts such as transition metal alloys or Pt monolayer core-shell nanoparticles versus metal d-band center energies or OH binding energies revealed a volcano-type dependence.[183, 184] The closer to the peak of the volcano plot, a catalyst situates the higher efficiency of kinetics for O-O bond breaking and simultaneous removal of OH from the catalyst surface. Figure 6.8 shows the specific activity of the Ir-Re alloy catalysts with a Pt_{ML} and Pd interlayer shell on various Ir-Re cores versus the OH binding energy calculated using DFT for the respective close-packed model Pt_{ML}/Pd_{ML}/Ir-Re alloy surfaces.

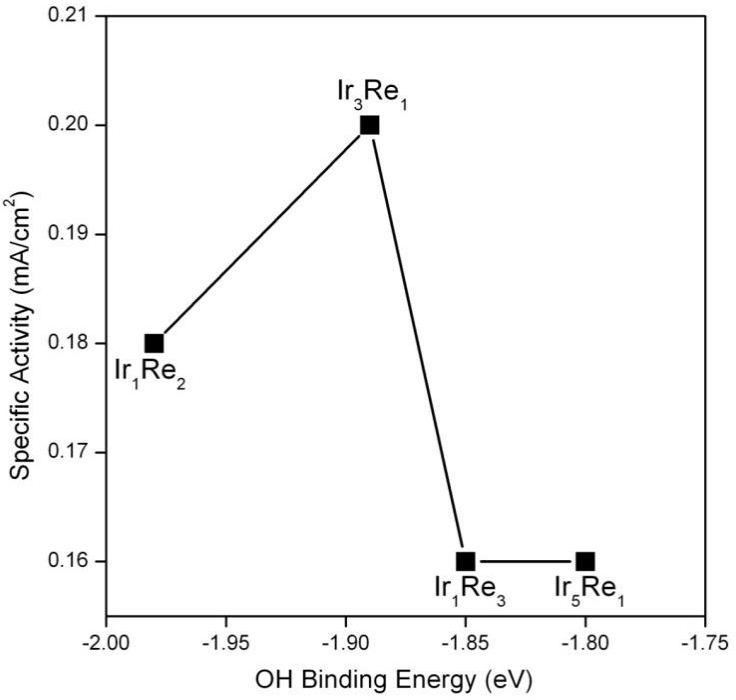

Figure 6.8 Specific activities of the Pt_{ML}/Pd_{ML}/Ir-Re alloy catalysts plotted against the calculated OH binding energy. The labels indicate the Ir-Re alloy composition of each data point.

The OH binding energy calculations support the experimental results discussed above. Whereas $Pt_{ML}/Pd_{ML}/Ir_1Re_2$ binds OH too strongly, making removal of OH via H_2O formation difficult, resulting in poisoning of the catalyst surface by OH, $Pt_{ML}/Pd_{ML}/Ir_1Re_3$ and $Pt_{ML}/Pd_{ML}/Ir_5Re_1$ appear to bind OH too weakly, suggesting weak binding of atomic oxygen and

thus difficult O-O bond activation. Of the alloys studied using DFT for the purpose of the present study, $Pt_{ML}/Pd_{ML}/Ir_3Re_1$ lies at the peak of the volcano with an intermediate OH binding energy corresponding to a maximum specific activity (Figure 6.8). Thus, the molar ratio of Ir to Re in the catalyst influences the binding strength of adsorbed OH and thereby the ORR activity of the catalysts. The systems considered using DFT have been restricted to those which are stable ordered phases as defined by the Ir-Re bulk alloy phase diagram.[199, 200] Unfortunately, we cannot comment on the OH binding energy on the optimum catalyst identified in the experiments, $Pt_{ML}/Pd_{ML}/Ir_2Re_1/C$. However, from those systems where both the experimental and theoretical analysis has been completed, we note the agreement between the experimental and theoretical results in identifying $Pt_{ML}/Pd_{ML}/Ir_3Re_1$ as the best of those catalysts. This result demonstrates that the OH binding energy works well as a reactivity descriptor for ORR, as demonstrated previously for a number of other systems.[183, 184, 186]

6.3.5 Stability of the Catalysts

An accelerated stability test for the $Pt_{ML}/Pd_{ML}/Ir_2Re_1$ catalyst was performed using a rotating disk electrode in a 0.1 M $HClO_4$ solution at room temperature. Figure 6.9 shows the ORR polarization curves at 1600 rpm before and after 30,000 potential cycles from 0.6 to 1.0 V. After 30,000 cycles the half-wave potential of the ORR polarization curve resumed at almost the original level when the cell medium was changed to fresh electrolyte and was tested for ORR. This indicates good stability and durability of the $Pt_{ML}/Pd_{ML}/Ir_2Re_1$ catalyst at ambient temperature under the accelerated test conditions.

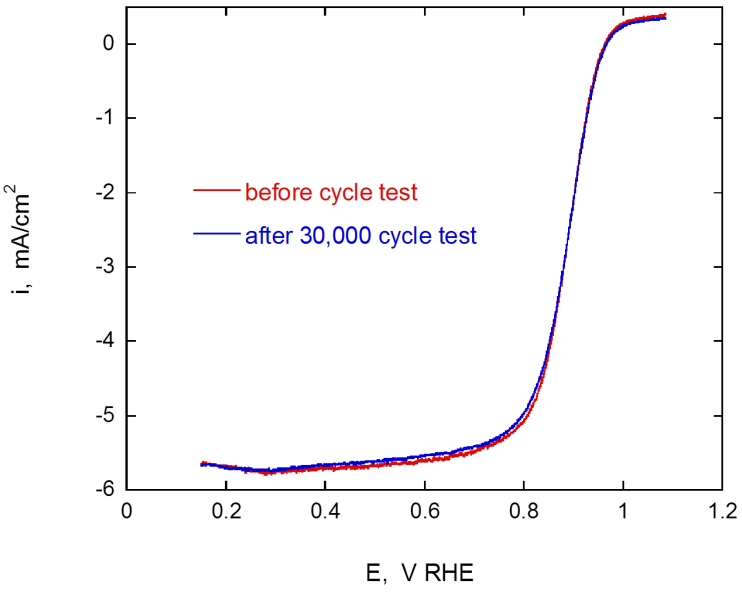

Figure 6.9 Accelerated stability test for $Pt_{ML}/Pd_{ML}/Ir_2Re_1$: the ORR polarization curves on a RDE in oxygen saturated 0.1 M $HClO_4$ at 1600 rpm before and after 30,000 potential cycles from 0.6 to 1.0 V.

6.4 Conclusions

New compositions of core-shell ORR catalysts were prepared by depositing palladium and platinum monolayers on various molar compositions of iridium and rhenium mixed core nanoparticles supported by Vulcan carbon. These catalysts are durable, acid resistant and exhibit electrocatalytic activity for oxygen reduction comparable to platinum. In the case of $Pt_{ML}/Pd_{ML}/Ir_2Re_1$, $Pt_{ML}/Pd_{2layers}/Ir_2Re_1$, and $Pt_{ML}/Pd_{2layers}/Ir_7Re_3$ catalysts, the ORR kinetics were, in fact, better than that of monometallic platinum and mass activities exceeded the 2015 US Department of Energy target level (0.44 A/mg). Applying the Pt and Pd monolayer on the core metals using the Cu-UPD technique requires the use of much less platinum. According to our DFT calculations, Ir and Re mixed metal cores contribute to decreasing OH poisoning on Pt. The catalyst with an Ir_2Re_1 core composition showed the highest ORR kinetics of those tested. When the mole ratio of Ir to Re at the core deviated from ~2:1, the ORR efficiency decreased. The Pd

interlayer in the shell enhanced catalyst activity. These factors appear to affect the OH binding energy such that an intermediate OH binding energy corresponding to a maximum in the catalyst activity could be achieved. The accelerated test involving 30,000 potential cycles shows the remarkable stability of these catalysts. The results show that $Pt_{ML}/Pd_{ML}/Ir_2Re_1$ catalysts are promising alternative to pure Pt ORR catalysts in low temperature fuel cells.

Chapter 7 Density Functional Theory Calculations and Analysis of Reaction Pathways for Reduction of Nitric Oxide by Hydrogen on Pt(111)[i]

7.1 Introduction

The catalytic conversion of nitric oxide, an unwanted byproduct of the combustion of hydrocarbons in air, to N_2 is an interesting reaction due to its fundamental and practical importance.[13, 14, 205-207] Platinum catalysts are active for the reduction of NO by H_2, but at low temperatures these catalysts demonstrate low selectivity toward N_2 and unfavorable production of side-products, namely N_2O and NH_3.[208-210] The relative selectivity to N_2O versus NH_3 is, among other factors, dependent on the NO to H_2 ratio. Thus, at high NO to H_2 ratios, improved selectivity for NO reduction by H_2 requires identification of materials for which the reaction kinetics favor N_2 formation over N_2O. Previous studies of NO reduction by H_2 on Pt catalysts have generally assumed that the reaction mechanism begins with N-O activation by (i) direct dissociation of NO or (ii) hydrogenation followed by N-O bond cleavage.[209, 211, 212]

$$\text{(i)}\quad NO^* + * \rightarrow N^* + O^*$$

$$\text{(ii)}\quad NO^* + H^* \rightarrow NOH^* + *$$

[i] Farberow, C. A.; Dumesic, J. A..; Mavrikakis, M., *ACS Catalysis* 2014 (submitted). Contributions by C. A. Farberow: 100% of DFT calculations and manuscript writing.

$$NOH^* + * \rightarrow N^* + OH^*$$

The major products are then formed through subsequent hydrogenation or N-N bond formation steps.

In this chapter, we report the results of a theoretical investigation, using electronic structure calculations based on planewave density functional theory (DFT-GGA), probing the role of hydrogen in N-O activation. We begin this study by predicting the surface coverage of nitric oxide under low temperature reaction conditions, and by directly investigating the impact that NO coverage has on the reaction energetics. In addition to the H-assisted pathway for N-O activation via NOH* suggested in the literature, we consider the possibility of an alternative HNO* intermediate and the addition of additional H* to NO* prior to N-O bond cleavage.

Typically, to rigorously probe the mechanistic pathway of a reaction under realistic conditions from first principles calculations, it is useful to construct a microkinetic model to describe experimental kinetic data.[35, 36] Because of the time and effort required by this approach, we suggest here a simplified approach, denoted as maximum rate analysis, to identify the most likely pathway(s) in complicated reaction schemes, making it possible to reduce the number of steps considered in more detailed kinetic models. We illustrate this approach to address various pathways for low temperature NO reduction by H_2 on Pt(111).

7.2 Methods

Density functional theory calculations were performed using the Vienna ab-initio Simulation Package (VASP).[31, 59] The exchange-correlation functional was described by the generalized gradient approximation (GGA-PW91).[30] The electron-ion interactions were described by

projector augmented wave (PAW) potentials.[63, 64] The electron wave function was expanded using plane waves with an energy cut-off of 400 eV.

The Pt(111) surface was modeled by a (2 x 2) unit cell, periodically repeated in a super cell geometry with successive 4-layer slabs separated by six equivalent layers of vacuum. The bottom two layers of the metal slab were fixed in their bulk truncated positions whereas the top two layers were allowed to relax. The surface Brillouin zone was sampled with a 6 x 6 x 1 Monkhorst-Pack k point grid.[213] Adsorption was allowed on only one of the two exposed metal surfaces per slab, and the electrostatic potential was adjusted accordingly.[155, 156] Structures were fully relaxed until the Hellmann–Feynman forces acting on the atoms were smaller than 0.05 eV/Å. The optimized lattice parameter of bulk Pt was calculated to be 3.98 Å, in agreement with the experimental value of 3.92 Å.[65]

The reported binding energies (BE) of adsorbates were calculated with respect to a clean relaxed Pt(111) slab ($E_{Pt(111)}$) and the respective adsorbate in the gas phase (E_{gas}).

$$BE = E_{total} - E_{Pt(111)} - E_{gas}$$

E_{total} is the total energy of the slab with the adsorbate on it. Minimum energy pathways and activation energy barriers for all elementary steps were calculated using the climbing-image nudged elastic band (CI-NEB) method.[33, 34] At least seven intermediate images were interpolated between reactant and product states for each elementary step. The transition state of the minimum energy pathway for each elementary step was confirmed by vibrational frequency calculations yielding a single imaginary frequency along the reaction coordinate.[157]

The phase diagram for NO/Pt(111) was generated by calculating the grand potential (Ω) at discrete coverages of 0.25 ML, 0.50 ML, 0.75 ML and 1.00 ML. The grand potential is defined as

$$\Omega = E_{NO/Pt} - E_{Pt} - N_{NO} * \mu_{NO} - T * S$$

where $E_{NO/Pt}$ is the total energy of the Pt(111) slab with N_{NO} NO molecules adsorbed, E_{Pt} is the total energy of the clean Pt(111) slab, μ_{NO} is the chemical potential of NO, T is the absolute temperature, and S is the entropy of the Pt(111) slab with N_{NO} NO molecules adsorbed. The chemical potential of NO was calculated by

$$\mu_{NO} = k_B * T * ln\frac{P}{P^o} + E_{NO} - T * S_{NO}$$

where k_B is the Boltzmann constant, P is the NO pressure, P^o is the reference pressure of 1 atm, E_{NO} is the total energy of NO in the gas phase, and S_{NO} is the entropy of gas phase NO.

To model a high NO-coverage environment in the DFT calculations, we completed DFT calculations which included 0.5 ML NO 'spectators' in the periodic unit cell. For the 2 x 2 unit cell used in this study, 0.5 ML NO spectators corresponds to two NO adsorbates in addition to the adsorbate(s) studied for a thermochemistry calculation or participating in the elementary step for the respective CI-NEB calculation. The NO spectator species are relaxed during the calculation. The reported binding energies of adsorbates on Pt(111) with 0.5 ML co-adsorbed NO spectators were calculated with respect to a relaxed Pt(111) slab with 0.5 ML adsorbed NO ($E_{0.5ML\ NO/Pt(111)}$) and the respective adsorbate in the gas phase (E_{gas}).

$$BE = E_{total} - E_{0.5\ ML\ NO/Pt(111)} - E_{gas}$$

E_{total} is the total energy of the slab with the adsorbate and 0.5 ML co-adsorbed NO. The calculations which include two NO spectator molecules will be referred to throughout this chapter as the 'high-coverage' calculations. DFT calculations completed on the clean Pt(111) surface will be referred to throughout this chapter as the 'low-coverage' calculations.

7.3 Results

7.3.1 Nitric Oxide Surface Coverage

The minimum energy configurations for NO adsorption at coverages of 0.25 ML, 0.50 ML, 0.75 ML and 1.00 ML on Pt(111), shown in Figure 7.1, are in agreement with the preferred adsorption sites reported in the literature, including those determined in high resolution x-ray photoelectron spectroscopy experiments conducted by Zhu et al.[214, 215] At 0.25 ML coverage, NO occupies the fcc site, oriented perpendicular to the Pt(111) surface, with a binding energy of -1.88 eV. This behavior is in agreement with previous theoretical studies[216-218] as well as the experimentally determined binding energy of -1.65 eV found by Wartnaby et al. using single-crystal microcalorimetry on Pt(110).[219] The additional NO adsorbate present at 0.5 ML NO-coverage occupies the top site, and is oriented at an angle of 39.5° relative to the surface. The differential binding energy of the second NO molecule in the unit cell is -1.42 eV. A third NO molecule adsorbed in the unit cell, corresponding to a total NO-coverage of 0.75 ML, occupies the hcp site with a binding energy of -1.05 eV. At 0.75 ML NO-coverage, the NO adsorbed in the top site is tilted at an angle of 44.4° relative to the surface, whereas the NO molecules adsorbed in the hcp and fcc sites are oriented perpendicular to the surface. At 1 ML NO coverage all adsorbed NO molecules occupy top sites, and are oriented at angles of ~59-60° relative to the

surface. The differential binding energy of the fourth NO molecule (at a total of 1 ML NO coverage) is mildly endothermic (BE = 0.03 eV).

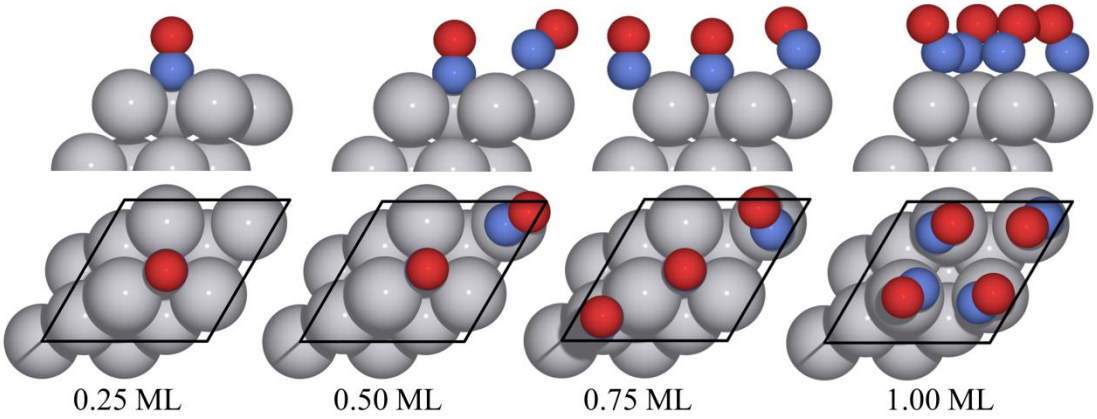

Figure 7.1 Minimum energy geometries for NO adsorption at varying coverages on the 2 x 2 unit cell of Pt(111); cross-section and top views shown in upper and lower panels, respectively. The periodic unit cell in the x and y direction is indicated by the black line. Red, blue and gray spheres represent O, N, and Pt, respectively.

Phase diagrams for NO adsorption, derived from the DFT-calculated minimum energy states are shown in Figure 7.2 at varying NO coverage.[157, 220] Figure 7.2a, depicting NO adsorption as a function of NO pressure at 400 K, shows that 0.75 ML NO is thermodynamically stable on Pt(111) at NO pressures up to 1 atm. The phase diagram for NO adsorption as a function of temperature at an NO pressure of 0.005 atm (Figure 7.2b) shows that 0.75 ML NO coverage remains the most thermodynamically stable state at temperatures from 300 to 1000 K. The choice of temperature and NO partial pressure in the phase diagrams are set based on typical experimental conditions. The predicted coverage found from the phase diagram motivated the choice of two NO spectators for the high coverage DFT calculations on Pt(111), because this corresponds to a total NO coverage of 0.75 ML at the initial state for direct NO dissociation.

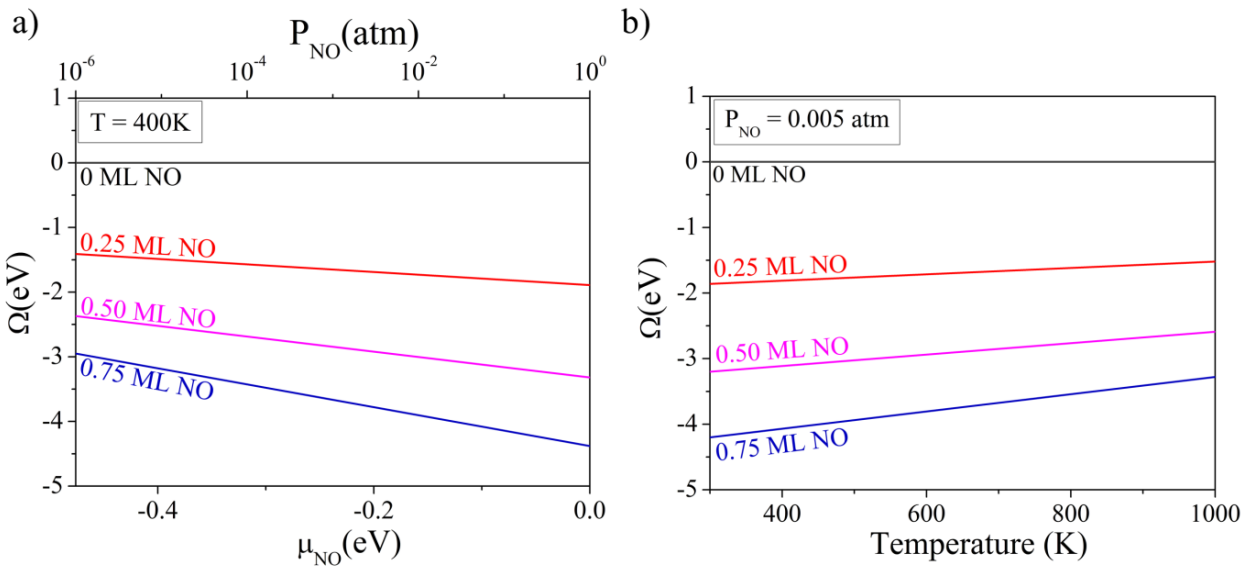

Figure 7.2 Phase diagram for NO coverage on Pt(111) (a) as a function of NO pressure at 400 K and (b) as a function of temperature at an NO pressure of 0.005 atm. The most stable state at a given pressure corresponds to the NO coverage with the most negative value for the grand potential, Ω.

7.3.2 Adsorption

The results of the thermochemistry calculations at high (0.5 ML NO spectators) and low NO coverage are shown in Figure 7.3. Throughout this chapter,'*' refers to an empty surface site and 'A*' indicates adsorbed intermediate A. The DFT-calculated binding energies on clean Pt(111) are in agreement with previous work by Ford et al.[216] All adsorbates, excluding NH_3*, are destabilized by the 0.5 ML co-adsorbed NO. NH_3 is characterized by very similar binding energy on the low coverage and the high coverage surface. The degree of destabilization of adsorbates is most significant for species that bind strongly to the surface (N*, NH*, O*) and least significant for the closed-shell adsorbates that are weakly bound to the surface (H_2O*, N_2*). The binding energy for N_2 is reduced from -0.12 eV on clean Pt(111) to 0 eV (does not adsorb) on the high coverage surface. N_2O and molecular H_2 do not adsorb on the clean Pt(111) surface or the high coverage surface. A majority of the adsorbates studied (nine of fourteen), which adsorb on the low and high coverage surfaces, retain their low coverage site preference on the high coverage

surface (Figure 7.3). The preferred adsorption site for H*, OH* and HNNO* at low coverage changes on the high coverage surface. However, the difference in the stability of the sites at low coverage is less than 0.06 eV. HNO* prefers to adsorb at the br-top site on the low coverage surface. In this configuration, the N in HNO* is coordinated to two Pt surface atoms at a bridge site and the O in HNO* binds to one Pt atom at a top site (Figure 7.3). In contrast, on the high coverage surface, HNO* binds at a top site through its N atom. ONNOH* adsorbs through both N atoms on neighboring top sites (top-top) on the high coverage surface, whereas on the low coverage surface it adsorbs through only one of its N atoms at a top site. In all systems, the spectator NO molecules occupy the remaining available fcc, hcp and/or top sites which maximize the distance between all of the co-adsorbates in the unit cell studied.

Adsorbate	$\theta_{NO} = 0$ BE (eV) Site		$\theta_{NO} = 0.5$ BE (eV) Site; NO sites		Adsorbate	$\theta_{NO} = 0$ BE (eV) Site		$\theta_{NO} = 0.5$ BE (eV) Site; NO sites	
NOH	-2.87 fcc	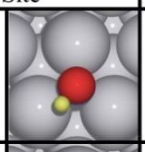	-2.00 fcc; hcp, top	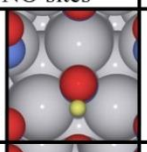	NH	-4.13 fcc	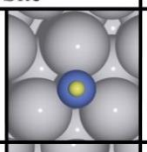	-3.12 fcc; hcp, top	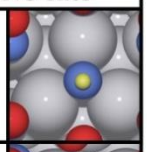
HNO	-1.75 br-top	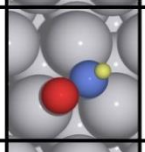	-1.00 top; fcc, hcp	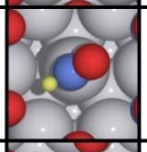	NH_2	-2.44 br	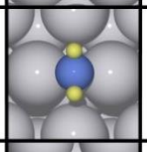	-1.82 br; fcc, top	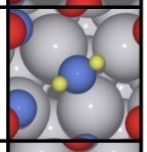
HNOH	-1.69 br	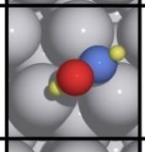	-0.90 br; fcc, top	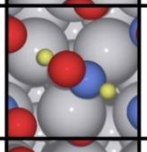	NH_3	-0.66 top	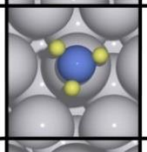	-0.66 top; fcc, hcp	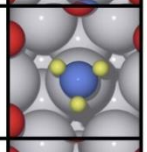
N	-4.76 fcc	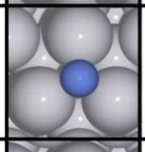	-3.55 fcc; hcp, top	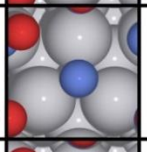	OH	-2.32 br	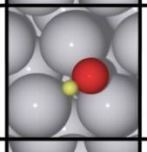	-2.06 top; fcc, hcp	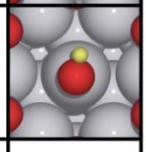
O	-4.31 fcc	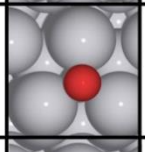	-3.39 fcc; hcp, top	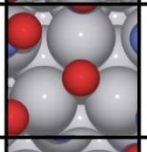	H_2O	-0.23 top	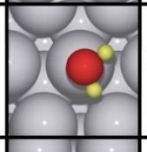	does not adsorb	--
H	-76 fcc	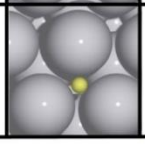	-2.44 br; fcc, top	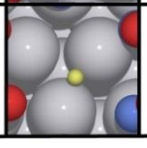	N_2	-0.12 top	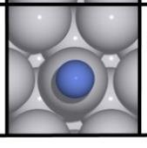	does not adsorb	--

Figure 7.3 Binding energies, site preference and top views of the minimum energy adsorption modes for the adsorbates on clean Pt(111) (low coverage) and on Pt(111) with 0.5 ML NO co-adsorbed (high coverage). For the high NO coverage systems, the site of the adsorbate is reported first, followed by the preferred sites of the two co-adsorbed NO molecules, all in the minimum energy configuration. All results are calculated in a 2 x 2 surface unit cell. Yellow, red, blue and gray spheres represent H, O, N, and Pt, respectively.

7.3.3 Elementary Steps: Reaction Energies and Activation Energy Barriers

The activation energy barriers (E_A) and reaction energies (ΔE) of all elementary steps studied at high and low coverage are reported in Table 7.1.

$$H_2 + 2* \rightarrow 2H*$$

The dissociative adsorption of H_2 is spontaneous on the clean surface, but has an activation energy barrier of 0.65 eV on the high NO coverage surface. On the clean surface, the reaction is exothermic with a reaction energy of -0.87 eV, whereas on the high coverage surface the reaction

is thermoneutral with a reaction energy of 0.01 eV. On both surfaces, the transition state lies above a Pt bridge site (Figure 7.4). On the high coverage surface, the H-H bond distance at the transition state is 0.85 Å. Similarly, the bond distance is 0.86 Å at the transition state on the low coverage surface.

$$NO^* + * \rightarrow N^* + O^*$$

The NO-coverage has the largest effect on the activation energy barrier for direct NO dissociation (NO* + * → N* + O*), where the barrier increases from 2.32 eV on the clean surface to 3.52 eV on the high NO coverage surface. These large activation energy barriers are in agreement with experimental studies showing that NO does not decompose on Pt(111) at low temperatures.[221, 222] Direct NO dissociation is significantly more endothermic on the high NO-coverage surface (2.02 eV) compared to the clean surface (0.79 eV). The transition states on the two surfaces are the same, with the O and N atoms at neighboring bridge sites (Figure 7.4). On the high coverage surface, at the transition state, the NO spectators are at neighboring top sites.

$$NO^* + H^* \rightarrow HNO^* + *$$

The formation of HNO* from NO* and H* is endothermic on the low coverage surface (ΔE = 0.40 eV) and exothermic (ΔE = -0.51 eV) on the high coverage surface. The activation energy barrier is significantly lower than the direct NO dissociation activation energy barrier on both the low coverage and high coverage surfaces, suggesting that a H-assisted pathway is likely on Pt(111) regardless of the NO surface coverage. The barrier for this hydrogenation step is 0.65 eV lower on the high coverage surface (E_A = 0.36 eV) than on the low coverage surface (E_A = 1.01 eV). On clean Pt(111) and high NO-coverage Pt(111), the N-H bond in HNO* at the transition state lies above a bridge site (Figure 7.4).

NO* + H* → NOH* + *

Whereas NO* can alternatively be hydrogenated to form NOH* on the low coverage surface, a direct pathway for this elementary step was not identified on the high coverage surface. The activation energy barrier on clean Pt(111) (E_A = 1.32 eV) is higher by ~0.3 eV than the barrier to form HNO*. On the clean Pt(111) surface at the transition state, the adsorbed NO is at an fcc site tilted at an angle of 56° relative to the surface and the H is at the edge of a Pt top site (Figure 7.4). The reaction energy on clean Pt(111) is 0.30 eV.

HNO* → NOH*

An alternative pathway to form NOH* on the high coverage surface was investigated, via an elementary step involving the transfer of the hydrogen in HNO* to a neighboring NO*. This step has a low barrier of 0.21 eV, and HNO* and NOH* are approximately isoenergetic (HNO* is more stable by 0.03 eV) on the high coverage surface. At the transition state, the H-NO* is at a top site and the N-OH* is at an fcc site (Figure 7.4). The H atom is 1.32 Å from the N in the HNO* reactant and 1.23 Å from the O in the NOH* product.

NOH* + * → N* + OH*

The activation energy barrier for breaking the N-O bond in NOH* at high NO-coverage is 1.81 eV, and the elementary step is endothermic with a reaction energy of 0.83 eV. On clean Pt(111) the activation energy barrier is lower (E_A = 1.07 eV) and the elementary step is exothermic with a reaction energy of -0.24 eV. At the transition state on the clean surface, the N is at an fcc site and the OH is at a neighboring top site. On the high coverage surface, at the transition state, the N is at bridge site and the OH is nearest to a top site directly across from the N (Figure 7.4).

HNO* + * → NH* + O*

The activation energy barrier for cleavage of the N-O bond in HNO* at high NO coverage is 2.26 eV and the reaction is endothermic with a reaction energy of 0.98 eV. On clean Pt(111), the activation energy barrier is 1.47 eV and the reaction is exothermic with a reaction energy of -0.19 eV. At the transition state on the clean surface, the O is nearest to a top site and the NH is nearest to a bridge site. On the high coverage surface, the transition state is similar to that found for direct NO dissociation: the O and the NH are located in neighboring bridge sites (Figure 7.4).

HNO* + H* → HNOH* + *

At high and low NO-coverage, the activation energy barrier for adding H* to HNO* is lower than the respective barriers for breaking the N-O bond in HNO*. In the presence of 0.5 ML of spectator NO, the activation energy barrier is 0.43 eV, and on the clean Pt(111) surface the barrier is 0.36 eV. This elementary step is exothermic on the high and low coverage surfaces, with a reaction energy of -0.74 eV and -0.15 eV, respectively. The H atom is at a top site and the HNO is at a bridge site, tilted toward the H atom at an angle of 42.5° relative to the surface, at the transition state for this elementary step at low coverage. At high NO-coverage, the H atom is also near a top site at the transition state, but the HNO is at a top site tilted at an angle of 30.3° relative to the surface (Figure 7.4).

NOH* + H* → HNOH* + *

On the low coverage surface the activation energy barrier for adding H* to NOH* (E_A = 1.09 eV) is approximately equal to the barrier for breaking the N-O bond in NOH* (E_A = 1.07 eV). In the case of the high coverage surface, the activation energy barrier for adding H* to NOH* is lower (E_A = 1.24 eV) than the barrier for breaking the N-O bond in NOH* (E_A = 1.81 eV). At the

transition state on the high coverage surface, the NOH is oriented perpendicular to the surface nearest to an fcc site, and the H is nearest to the neighboring hcp site. At the transition state on the low coverage surface, the NOH is at a bridge site, tilted at an angle of 49.4° relative to the surface, and the H is nearest to a top site across from the N end of the NOH (Figure 7.4). The elementary step is approximately thermoneutral on the low coverage surface (ΔE = -0.02 eV) and exothermic (ΔE = -0.86 eV) on the high coverage surface.

$$\boldsymbol{HNOH^* + * \rightarrow NH^* + OH^*}$$

The activation energy for N-O bond breaking in HNOH* at low coverage is 0.70 eV, and the reaction is exothermic with a reaction energy of -0.83 eV. At the transition state, the OH is nearest to a top site and the NH is nearest to a bridge site (Figure 7.4). On the high coverage surface, the activation energy barrier is higher (E_A = 1.67 eV) and the elementary step is slightly endothermic (ΔE = 0.09 eV). At the transition state at both low and high NO coverage, the OH is nearest to a top site and the NH is nearest to a bridge site (Figure 7.4). The N-O distance at the transition state is the same at high and low coverage: 1.84 Å. On the high coverage surface at the transition state, the OH is approximately 0.35 Å further above the top site, compared with the low coverage transition state.

$$\boldsymbol{HNOH^* \rightarrow N^* + H_2O_{(g)}}$$

The elementary step HNOH* → N* + $H_2O_{(g)}$ is a concerted step involving both N-O bond cleavage and O-H bond formation. This step does not occur directly on the low coverage surface. On the high coverage surface, this elementary step is exothermic with a reaction energy of -0.67 eV, and the activation energy barrier is 1.36 eV. At the transition state, the N-O bond

distance is 2.04 Å and the OH is rotated approximately 90° relative to the orientation of the OH in HNOH* (Figure 7.4).

$$\boldsymbol{HNOH^* + H^* \rightarrow NH^* + H_2O_{(g)} + *}$$

The elementary step HNOH* + H* → NH* + $H_2O_{(g)}$ is a concerted step, and involves both N-O bond cleavage and O-H bond formation. This step was not studied on the low coverage surface, because it is unlikely that it would occur directly. On the high coverage surface, this elementary step is exothermic with a reaction energy of -1.52 eV, and the activation energy barrier is 0.69 eV. At the transition state, the N-O bond distance is 1.52 Å (Figure 7.4).

$$\boldsymbol{2N^* \rightarrow N_2^* + *}$$

The activation energy barriers for N_2 formation from atomic nitrogen are high and this step is exothermic on the high coverage (E_A = 1.60 eV, ΔE = -2.28 eV) and low coverage (E_A = 1.55 eV, ΔE = -1.94 eV) surfaces. The transition states are similar on both surfaces with the N atoms in neighboring bridge sites (Figure 7.4).

$$\boldsymbol{NO^* + N^* \rightarrow N_2O_{(g)} + 2^*}$$

N_2O formation via NO* + N* → $N_2O_{(g)}$ + 2* has a significantly higher barrier on the low coverage (E_A = 1.18 eV) surface than on the high coverage (E_A = 0.08 eV) surface. This step is slightly endothermic (ΔE = 0.17 eV) on the low coverage surface and highly exothermic (ΔE = -2.50 eV) on the high coverage surface. On the high coverage surface, at the transition state, N is at an fcc site and NO is at a bridge site with an N-N distance of 2.28 Å. At the transition state on the low coverage surface, the N-N distance of 1.94 Å is shorter. At the transition state on the low coverage surface, the N atom is at an hcp site and the NO is nearest to a top site (Figure 7.4).

NO* + NH* → HNNO* + *

The formation of HNNO*, via N-N bond formation between NH* and NO*, has an activation energy barrier of 0.69 eV on the high NO coverage Pt(111) surface and is exothermic with a reaction energy of -0.90 eV. The activation energy barrier on clean Pt(111) is higher and the reaction step is thermoneutral (E_A = 1.09 eV, ΔE = 0.03 eV). At the transition state (Figure 7.4) on the high coverage surface, the NH* and the NO* are at neighboring bridge sites and the N-N bond distance is 1.55 Å. On the clean surface at the transition state, the NH is at a bridge site and the NO is nearest to a top site. The N-N bond distance is 1.83 Å.

HNNO* → $N_2O_{(g)}$ + H*

On the high NO coverage Pt(111) surface, the activation energy barrier for breaking the N-H bond in HNNO* to produce N_2O in the gas phase is 0.72 eV. On clean Pt(111), the barrier is 1.46 eV. This step is exothermic on the high coverage surface (ΔE = -0.81 eV) and endothermic on clean Pt(111) (ΔE = 0.48 eV). The transition state is similar on the two surfaces (Figure 7.4). The N-N-O lies approximately parallel to the surface above a bridge site, with the O end tilted away from the surface, and the H is nearest to a top site. The N-H bond distance is 1.04 Å and 1.30 Å, on the high NO coverage surface and on clean Pt(111), respectively. The H atom cannot be seen in Figure 7.4 because it lies directly below the N end.

NH_3 formation

The three hydrogen addition steps required to form NH_3 through hydrogenation of an adsorbed N atom have lower activation energy barriers and are more exothermic on the high coverage surface compared to the low coverage surface. The first hydrogenation step, to form NH* from N*, has a barrier of 0.80 eV and a reaction energy of -0.54 eV on the low coverage

surface. On the high coverage surface, the activation energy barrier is 0.54 eV and the reaction energy is -1.32 eV. The transition states are similar on both surfaces: the N atom is at an fcc site and the H atom is nearest to a top site (Figure 7.4). On both surfaces, the addition of the second H atom to form NH_2* from NH* has the highest barrier of the three hydrogenation steps. The activation energy barrier for NH* + H* → NH_2* + * is 1.27 eV at low coverage and 0.95 eV at high NO-coverage. This elementary step is exothermic on both surfaces with a reaction energy of -0.09 eV at low coverage and -0.88 eV at high NO-coverage. At the transition state on the high and low coverage surfaces, the H atom is nearest to a top site. On the low coverage surface, the NH is at a bridge site at the transition state, whereas on the high NO-coverage surface at the transition state the NH is at an fcc site (Figure 7.4). The third hydrogenation step, leading to adsorbed NH_3, has an activation energy barrier of 0.54 eV and 0.31 eV and a reaction energy of -0.63 eV and -1.68 eV on the low coverage and high NO-coverage surfaces, respectively. The transition state for this third hydrogenation step is similar on the two surfaces, with the NH_2 and the H atom located nearest to neighboring top sites (Figure 7.4).

H_2O formation

The activation energy barrier for hydrogenation of O* to form OH* is 0.91 eV on the clean Pt(111) and 0.22 eV on the high NO-coverage Pt(111) surface. The elementary step is more exothermic on the high coverage (ΔE = -1.71 eV) surface compared to the low coverage (ΔE = -0.17 eV) surface. At the transition state on the low coverage surface, the O is at a bridge site and the H is at a top site. On the high coverage surface at the transition state, both O and H are at neighboring bridge sites (Figure 7.4).

The formation of H_2O from OH* has a similar activation energy barrier on the two surfaces: 0.17 eV at low coverage and 0.15 eV at high NO-coverage. This elementary step is more exothermic on the high coverage surface, with a reaction energy of -1.50 eV compared to a reaction energy of -0.73 eV on the low coverage surface.

Table 7.1 Activation energy barriers (E_A) and reaction energies (ΔE) for elementary steps on clean Pt(111) (low coverage) and on Pt(111) with 0.5 ML NO co-adsorbates (high coverage).[a]

Elementary Step	**Low coverage**		**High Coverage**	
	E_A**(eV)**	**ΔE (eV)**	E_A**(eV)**	**ΔE (eV)**
NO* + * → N* + O*	2.32	0.79	3.52	2.02
NO* + H* → HNO*	1.01	0.40	0.36	-0.51
NO* + H* → NOH* + *	1.32	0.30	--	--
NOH* + * → N* + OH*	1.07	-0.24	1.81	0.83
HNO* + * → O* + NH*	1.47	-0.19	2.26	0.98
HNO* + NO* → NOH* + NO*	NS	NS	0.21	0.03
NOH* + H* → HNOH* + *	1.09	-0.02	1.24	-0.86
HNO* + H* → HNOH* + *	0.36	-0.15	0.43	-0.74
HNOH* + * → NH* + OH*	0.70	-0.83	1.67	0.09
HNOH* → N* + H_2O	--	--	1.36	-0.67
HNOH* + H* → NH* + H_2O + *	NS	NS	0.69	-1.52
N* + N* → N_2*	1.55	-1.94	1.60	-2.28
NO* + N* → N_2O + 2*	1.18	0.17	0.07	-2.50
N* + H* → NH* + *	0.80	-0.54	0.54	-1.32
NH* + H* → NH_2* + *	1.27	-0.09	0.95	-0.88
NH_2* + H* → NH_3* + *	0.54	-0.63	0.31	-1.98
O* + H* → OH* + *	0.91	-0.17	0.22	-1.71
OH* + H* → H_2O* + *	0.17	-0.73	0.15	-1.50
H_2 + 2* → H* + H*	0.00	-0.87	0.65	0.08
HNOH* + H*→ NH_2OH* + *	NS	NS	0.65	-0.93
NO* + NH* → HNNO* + *	1.09	0.03	0.69	-0.90
HNNO* → N_2O + H*	1.46	0.48	0.72	-0.81
HNNO* + NO* → NOH* + N_2O + *	NS	NS	0.61	0.60
NH* + NO* → N* + HNO*	NS	NS	0.62	0.62
2NH* → H_2N_2* + *	NS	NS	2.83	-0.46
N_2O* + *→ N_2* + O*	0.61	-1.43	--	--
NO* + NOH* → ONNOH* + *	0.98	0.16	NS	NS

[a]'NS' indicates an elementary step that was not studied on the listed surface and '—' indicates a step which has been studied, but a direct path for the elementary step was not found on the listed surface.

Elementary Step	TS $\theta_{NO} = 0$	TS $\theta_{NO} = 0.5$	Elementary Step	TS $\theta_{NO} = 0$	TS $\theta_{NO} = 0.5$	Elementary Step	TS $\theta_{NO} = 0$	TS $\theta_{NO} = 0.5$
$H_2 + 2^* \rightarrow 2H^*$	$E_A = 0$ eV	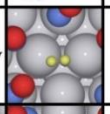	$HNOH^* + ^* \rightarrow NH^* + OH^*$	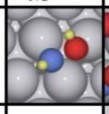	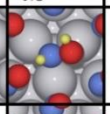	$HNOH^* + H^* \rightarrow NH^* + H_2O_{(g)} + ^*$	NS	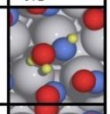
$NO^* + ^* \rightarrow N^* + O^*$	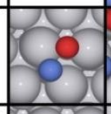	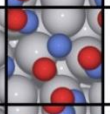	$HNOH^* \rightarrow N^* + H_2O_{(g)}$	--	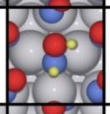	$HNOH^* + H^* \rightarrow NH_2OH^* + ^*$	NS	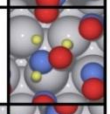
$NO^* + H^* \rightarrow HNO^* + ^*$	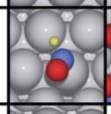	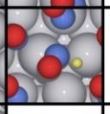	$2N^* \rightarrow N_2^* + ^*$	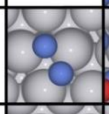	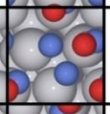	$NO^* + NH^* \rightarrow HNNO^* + ^*$	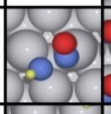	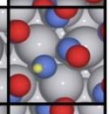
$NO^* + H^* \rightarrow NOH^* + ^*$	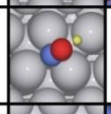	--	$NO^* + N^* \rightarrow N_2O_{(g)} + 2^*$	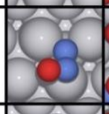	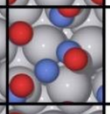	$HNNO^* \rightarrow N_2O_{(g)} + H^*$	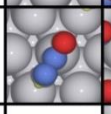	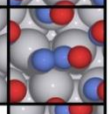
$HNO^* + ^* \rightarrow NH^* + O^*$	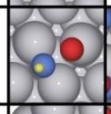	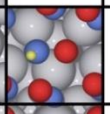	$N^* + H^* \rightarrow NH^* + ^*$	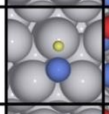	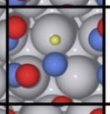	$HNNO^* + NO^* \rightarrow NOH^* + N_2O_{(g)} + ^*$	NS	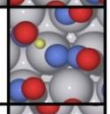
$NOH^* + ^* \rightarrow N^* + OH^*$	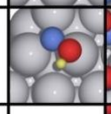	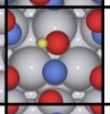	$NH^* + H^* \rightarrow NH_2^* + ^*$	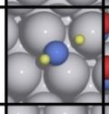	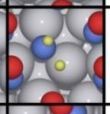	$NH^* + NO^* \rightarrow N^* + HNO^*$	NS	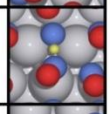
$HNO^* \rightarrow NOH^*$	NS	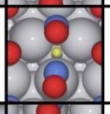	$NH_2^* + H^* \rightarrow NH_3^* + ^*$	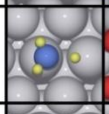	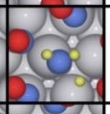	$2NH^* \rightarrow N_2H_2^* + ^*$	NS	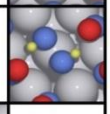
$HNO^* + H^* \rightarrow HNOH^* + ^*$	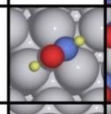	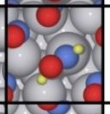	$O^* + H^* \rightarrow OH^* + ^*$	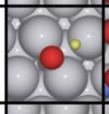	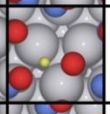	$N_2O^* + ^* \rightarrow N_2^* + O^*$	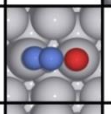	--
$NOH^* + H^* \rightarrow HNOH^* + ^*$	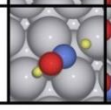	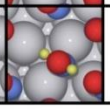	$OH^* + H^* \rightarrow H_2O^* + ^*$	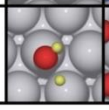	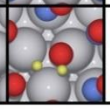	$NO^* + NOH^* \rightarrow ONNOH^* + ^*$	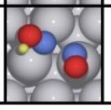	NS

Figure 7.4 Transition state (TS) configurations of elementary steps on clean Pt(111) (low coverage) and on Pt(111) with 0.5 ML NO co-adsorbates (high coverage). 'NS' indicates an elementary step that was not studied on the listed surface and '—' indicates a step for which a direct path was not found on the listed surface. Yellow, red, blue and gray spheres represent H, O, N, and Pt, respectively.

In general, the activation energy barriers for the bond-making steps *decrease* at higher NO coverage, and the activation energy barriers for the bond-breaking steps *increase* with increasing coverage. This general trend is observed because a significant component of the activation energy barrier is related to the binding energy of reactants and products of elementary steps. For instance, on the high coverage surface, the individual reactants of a bond-making step are bound more weakly compared to adsorption on the clean surface. As a result, it is easier for them to

reach the transition state for the bond making step, relative to the clean surface, which gives rise to a smaller barrier for a bond-making step on the high coverage surface. Analogous arguments explain the general trend observed for the bond-breaking steps: a smaller barrier on the clean surface. The hydrogenation of NOH* and HNO*, and the formation of N_2 via the combination of two N* species ($2N^* \rightarrow N_2$) do not follow this general principle; these bond-making steps have higher activation energy barriers at the higher NO coverage. However, the difference between the calculated activation energy barrier at high and low coverage is less than 0.15 eV for all three of these steps. The bond-breaking step $HNNO^* \rightarrow N_2O + H^*$ does not follow the general trend: the activation energy barrier is lower on the high coverage surface. Because this step produces N_2O in the gas phase, it significantly reduces the repulsive interactions on the high coverage surface and is therefore exothermic on the high coverage surface. In contrast, it is an endothermic step on the low coverage surface.

7.3.4 Maximum Rate Analysis

From the elementary steps outlined above, multiple pathways are possible for cleavage of the N-O bond, shown schematically in Figure 7.5.[i] The N-O bond activation mechanisms considered all lead to either N* or NH*. In the case of NH*, adsorbed atomic nitrogen could then be formed by N-H dissociation such that all pathways lead to N_2O via $N^* + NO^* \rightarrow N_2O + 2^*$. The most commonly utilized and simplest procedure for assessing which of multiple competing reaction pathways may carry the flux in an overall reaction involves identifying the minimum energy pathway by plotting the energy or enthalpy versus the reaction coordinate for the various

[i] Because the elementary step involving N-O bond breaking in NH_2OH^* was not included in this study, NH_2OH^* was not included as a possible intermediate in N-O activation

pathways. This approach, while informative, fails to consider potentially significant entropic effects. Therefore, a more detailed analysis involves constructing plots of the Gibbs free energy versus the reaction coordinate. Still, these plots of energy or Gibbs free energy versus reaction coordinate approaches can be misleading, because the location of the highest transition state energy can depend on the order in which the steps are plotted. For example, by changing the order of the elementary steps, specifically the adsorption steps, in direct NO dissociation (mechanism 1) on clean Pt(111), the location of the maximum transition state energy in the Gibbs free energy surface can change (see Figure 7.6). For this reason, the most rigorous procedure to predict the reaction flux through a specific pathway is generation of a full microkinetic model,[35, 36] which requires significant time and effort, particularly for reactions with multiple products and many possible pathways. Accordingly, prior to conducting detailed microkinetic analyses (which is the subject of Chapter 8), we suggest a maximum rate analysis to probe the viability of various possible reaction pathways. This systematic analysis alleviates the issue with the ordering of elementary steps in kinetic analyses using plots of energy versus reaction coordinate, because all transition state energies are calculated relative to gas phase reactants and products. In addition, the maximum rate analysis, outlined below, can be particularly useful for reducing the complexity of a subsequent microkinetic model by justifying the elimination of those elementary steps with very slow maximum rates.

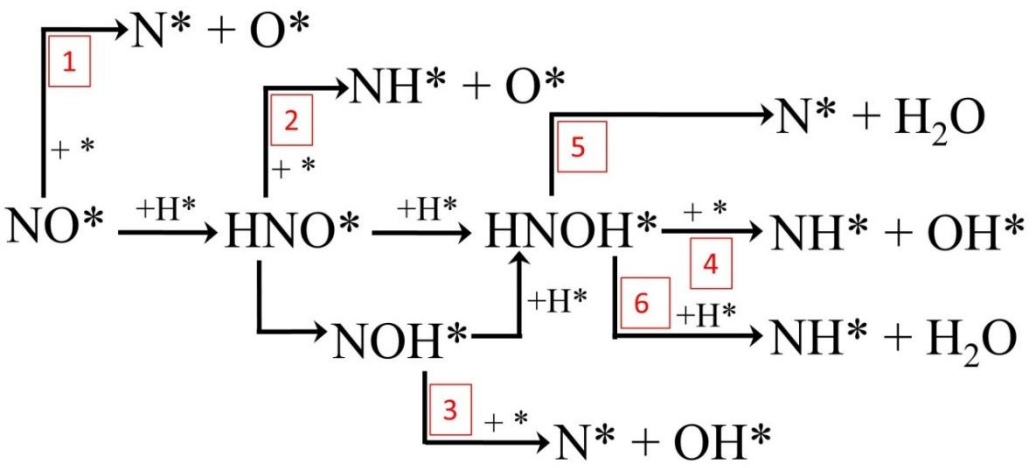

Figure 7.5 Reaction mechanisms for N-O bond activation in NO reduction by H_2. Labels with red numbers correspond to mechanisms in Table 2. DFT calculations showed that NO* + H* → NOH* + * does not occur as an elementary step on Pt(111) at high NO coverage. Mechanisms 4, 5 and 6 could all occur via step (i) HNO* + H* → HNOH* + * or step (ii) HNO* + H* → NOH* + H* → HNOH*. Because the maximum rates for the elementary steps in (i) are larger than those in (ii), we only consider path (i) in the analysis of mechanisms 4-6, although we do not exclude the possibility that NOH* could participate.

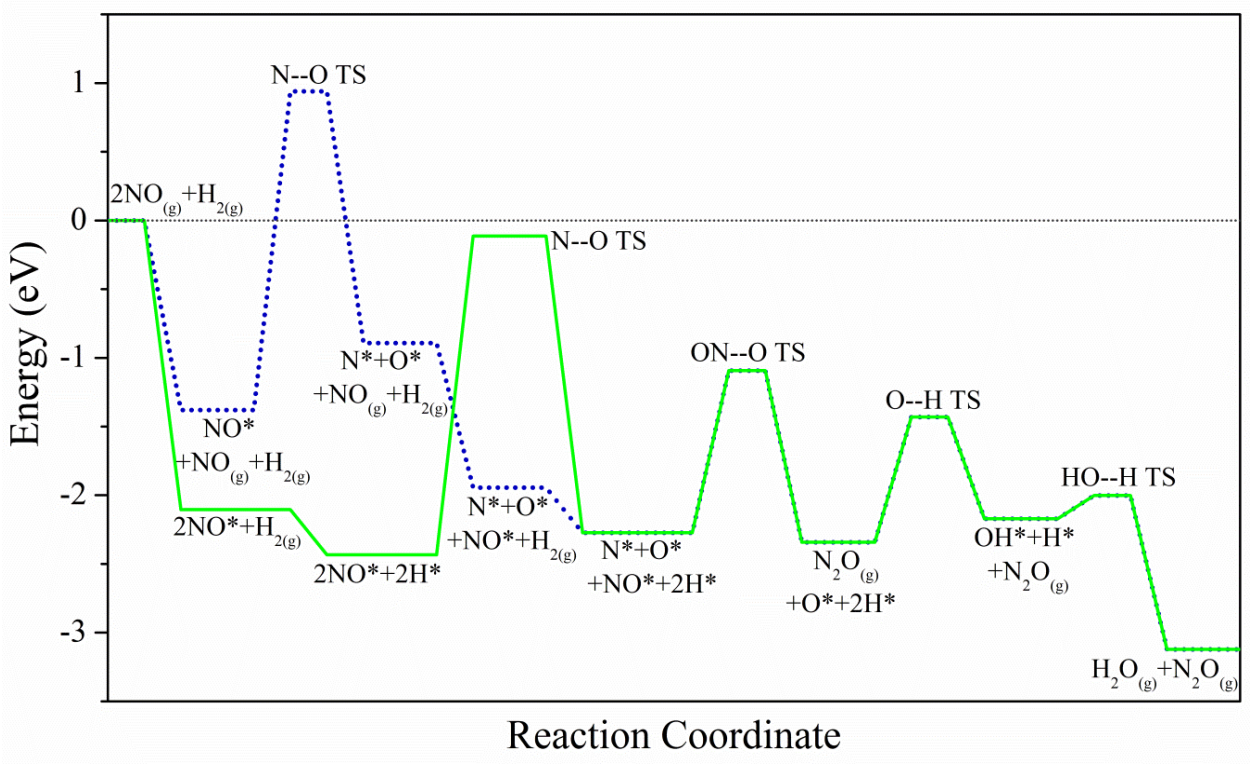

Figure 7.6 Free energy surface for N_2O formation via direct NO dissociation (mechanism 1) on clean Pt(111). The solid green line shows the PES constructed with all adsorption steps occurring along the reaction coordinate before the N-O bond-breaking step. The dotted blue line shows the PES constructed with the second NO adsorption step and H_2 dissociative adsorption occurring in the reaction coordinate after N-O bond-breaking.

To determine the most likely pathways via the maximum rate analysis, we first calculate the maximum rate of each elementary step in each mechanism based on the assumption that this step is the rate-determining step and that all other elementary steps in the mechanism are equilibrated. The rate of an elementary step involving a vacant site term is maximized when there is no site-blocking and therefore θ_*, the fraction of vacant surface sites, is equal to one. Partial pressures of gas phase reactants and products and the reaction temperature are set based on the conditions of experimental studies. In this case, we use a typical set of experimental conditions for this reaction, namely: temperature of 400 K and NO, H_2, N_2O and H_2O partial pressures of 0.005 atm, 0.050 atm, 0.0002 atm and 0.0002 atm, respectively. Once the maximum rate of each elementary step has been calculated, the values for the slowest maximum rate in the competing mechanisms are compared and discussed. The most likely reaction mechanisms are identified as those mechanisms with the largest calculated maximum rate for the slowest elementary step in the mechanism.

To illustrate the maximum rate analysis procedure, we derive the maximum rate equation for elementary steps in two example reaction mechanisms of differing complexity. We start with a simple reaction mechanism for the overall reaction A + B → AB:

Elementary Step 1. A + * → A*

Elementary Step 2. B + * → B*

Elementary Step 3. A* + B* → AB* + *

Elementary Step 4. AB* → AB + *

We now calculate the maximum rate of any individual step, assuming all of the other steps are in equilibrium. Based on transition state theory, the rate of reaction 1, (r_1), in units of molecules per area per time, is equal to the concentration of the activated complex times a frequency factor equal to k_BT/h, where k_B is the Boltzmann constant, T is the temperature and h is Planck's constant. For surface reactions, r_1 can be written as a turnover frequency, in units of s^{-1}, by dividing by the total concentration of surface sites, S_0, in units of sites per area.

$$r_1 = \frac{k_B T}{h S_0} [A^{*\ddagger}]$$

The equilibrium constant, $K_1^{\ddagger}$, for production of the activated complex $A^{*\ddagger}$ from gas phase A is

$$K_1^{\ddagger} = e^{\frac{-\Delta G_1^{\ddagger}}{k_B T}} = \frac{\alpha_{A^{*\ddagger}}}{\alpha_A \alpha_*}$$

where $\Delta G_1^{\ddagger}$ is the Gibbs Free energy change for formation of the activated complex from gas phase A and α_i is the activity of species i. The activity of gas phase species A is the partial pressure of A, P_A, divided by the standard state pressure, P^0, of 1 atm. The activity of a surface adsorbate is the concentration of the adsorbate, in units of molecules per area, divided by the standard state which is the total concentration of surface sites (S_0). This normalization gives the fractional surface coverage of surface adsorbate i, θ_i. Likewise, the activity term for vacant sites is the fractional coverage of empty sites, θ_*. $K_1^{\ddagger}$ can now be written as:

$$K_1^{\ddagger} = e^{\frac{-\Delta G_1^{\ddagger}}{k_B T}} = \frac{\frac{[A^{*\ddagger}]}{S_0}}{\frac{P_A}{P^0}\frac{[*]}{S_0}} = \frac{\theta_{A^{*\ddagger}}}{p_A \theta_*}$$

where p_i is the partial pressure of *i* divided by the standard state pressure. The Gibbs free energy change of step *j* is calculated from the change in enthalpy and entropy

$$\Delta G_j^{\ddagger} = \Delta H_j^{\ddagger} - T * \Delta S_j^{\ddagger}$$

The enthalpy and entropy of gas phase species are found from the energy and vibrational frequency calculations, and their temperature dependence is described using the Shomate equation. The procedure for calculating the thermodynamic parameters for gas phase species has been described in detail elsewhere.[20, 36] For adsorbed species, the enthalpy is calculated by adding the DFT-derived binding energy to the enthalpy of the species in the gas phase. The entropy of an adsorbate is approximated as its local entropy, where the local entropy is the entropy of the species in the gas phase minus its 3D translational entropy. This choice for the entropy approximation is adequate due to the approximate nature of the maximum rate analysis, whereas more rigorous methods based on DFT calculations of the frustrated vibrational and rotational modes of adsorbed species could be used later, in a full microkinetic model. The entropy at the transition state is set equal to the final state entropy for bond-making steps and the initial state entropy for bond-breaking steps. The enthalpy at the transition state is equal to the initial state enthalpy plus the DFT-calculated activation energy barrier.

The reaction rate is maximized when there is no site-blocking, such that θ_* is equal to unity. Thus, the maximum value of r_1, $r_{1,max}$, is given by:

$$r_{1,max} = \frac{k_B T}{h} e^{\frac{-\Delta G_1^{\ddagger}}{k_B T}} p_A$$

Similar analysis leads to the analogous expression for $r_{2,max}$.

$$r_{2,max} = \frac{k_B T}{h} e^{\frac{-\Delta G_2^{\ddagger}}{k_B T}} p_B$$

The rate of reaction 3, r_3, and the equilibrium constant for production of the activated complex $AB^{**\ddagger}$ from adsorbed A and B are:

$$r_3 = \frac{k_B T}{h} \theta_{AB^{**\ddagger}} \qquad K_3^{\ddagger} = e^{\frac{-\Delta G_3^{\ddagger}}{k_B T}} = \frac{\theta_{AB^{**\ddagger}}}{\theta_A \theta_B}$$

To derive the rate expression for step 3 in terms of gas phase reactants and products, we use the equilibrium constant equations for elementary steps 1 and 2, because these steps are assumed to be equilibrated, to express θ_A and θ_B in terms of p_A and p_B.

$$K_3^{\ddagger} = e^{\frac{-\Delta G_3^{\ddagger}}{k_B T}} = \frac{\theta_{AB^{**\ddagger}}}{e^{\frac{-\Delta G_1}{k_B T}} e^{\frac{-\Delta G_2}{k_B T}} p_A p_B \theta_*^2}$$

The expression for $r_{3,max}$ thus becomes

$$r_{3,max} = \frac{k_B T}{h} e^{\frac{-\Delta G_3^{\ddagger} - \Delta G_1 - \Delta G_2}{k_B T}} p_A p_B$$

Importantly, this expression for $r_{3,max}$ could alternatively be derived by adding the elementary steps to generate an overall reaction, 3^{sum}, for the formation of the activated complex AB**‡ directly from gas phase A and B.

A + * ↔ A*

B + * ↔ B*

<u>A* + B* ↔ AB**‡</u>

(3^{sum}) A + B + 2* ↔ AB**‡

The equilibrium constant for production of the activated complex $AB^{**‡}$ from *gas phase* A and B can then be used to derive an expression for the coverage of the activated complex $\theta_{AB^{**‡}}$. The equilibrium constant is calculated as:

$$K_{3,sum}^{‡} = K_3^{‡} K_1 K_2 = e^{\frac{-\Delta G_3^{‡}}{k_B T}} e^{\frac{-\Delta G_1}{k_B T}} e^{\frac{-\Delta G_2}{k_B T}} = \frac{\theta_{AB^{**‡}}}{p_A p_B \theta_*^2}$$

where K_1 and K_2 are the equilibrium constants for elementary step 1 and 2, respectively. We can then add the three free energy change terms to determine $\Delta G_{3,sum}^{‡}$, the change in Gibbs free energy for the formation of the activated complex from gas phase A and B. This lumping results in the elimination of all of the free energy terms for A* and B*.

$$-\Delta G_{3,sum}^{‡} = -\Delta G_3^{‡} - \Delta G_1 - \Delta G_2 = -\left(G_{AB^{**‡}} - G_{A^*} - G_{B^*}\right) - \left(G_{A^*} - G_A\right) - \left(G_{B^*} - G_B\right)$$

$$= -\left(G_{AB^{**‡}} - G_A - G_B\right)$$

$$r_{3,max} = \frac{k_B T}{h} e^{\frac{-\Delta G_{3,sum}^{‡}}{k_B T}} p_A p_B$$

Lastly, the maximum rate expression for elementary step 4 is

$$r_{4,max} = \frac{k_B T}{h} e^{\frac{-\Delta G^{\ddagger}_{4,sum}}{k_B T}} p_A p_B$$

The approach of adding all of the elementary steps to generate an overall equation involving only the activated complex in the assumed rate-determining step and gas phase reactants and products is particularly useful when calculating maximum rates of elementary steps in more complicated reaction mechanisms. For example, below is one possible reaction mechanism for the overall reaction 4A + 2CB → $2A_2C + B_2$.

Elementary Step 1. A + * → A*

Elementary Step 2. CB + * → CB*

Elementary Step 3. A* + CB* → ACB* + *

Elementary Step 4. ACB* + * → AC* + B*

Elementary Step 5. AC* + A* → A_2C* + *

Elementary Step 6. 2B* → B_2 +2*

Elementary Step 7. A_2C* → A_2C + *

For this example, we will only derive the equation for calculating the maximum rate of elementary step 5.

$$r_5 = \frac{k_B T}{h S_0} [A_2 C^{**\ddagger}]$$

Assuming all other reactions are equilibrated and step 5 is rate-determining, the following elementary steps can be added to express the overall reaction for forming the activated complex $A_2C^{**‡}$ from *gas phase* reactants and products.

2 (A + * → A*)

CB + * → CB*

A* + CB* → ACB* + *

ACB* + * → AC* + B*

AC* + A* ↔ $A_2C^{**‡}$

(1/2) 2B* → B_2 +2*

(5^{sum}) 2A + CB + 2* ↔ $A_2C^{**‡}$ + 1/2B_2

The equilibrium constant is now written for the total reaction giving the production of the activated complex, $A_2C^{**‡}$, from gas phase A, CB and B_2, where all energy terms related to adsorbed intermediates cancel, leaving $\Delta G^{‡}_{5,sum}$.

$$K^{‡}_{5,sum} = K^{‡}_5 K_1^2 K_2 K_3 K_4 K_6^{\frac{1}{2}} = e^{\frac{-\Delta G^{‡}_5}{k_B T}}\left[e^{\frac{-\Delta G_1}{k_B T}}\right]^2 e^{\frac{-\Delta G_2}{k_B T}} e^{\frac{-\Delta G_3}{k_B T}} e^{\frac{-\Delta G_4}{k_B T}}\left[e^{\frac{-\Delta G_6}{k_B T}}\right]^{1/2} = \frac{\theta_{A_2C^{**‡}} p_{B_2}^{1/2}}{p_A^2 p_{CB} \theta_*^2}$$

$$\theta_{A_2C^{**‡}} = e^{\frac{-\Delta G^{‡}_{5,sum}}{k_B T}} \frac{p_A^2 p_{CB} \theta_*^2}{p_{B_2}^{1/2}}$$

Then we can use the expression for $\theta_{A_2C^{**‡}}$ to calculate $r_{5,max}$.

$$r_{5,max} = \frac{k_B T}{h} e^{\frac{-\Delta G^{‡}_{5,sum}}{k_B T}} \frac{p_A^2 p_{CB}}{p_{B_2}^{1/2}}$$

Once the maximum rates of all of the elementary steps in a reaction mechanism have been calculated, the minimum of these rates can be compared with the minimum rates of competing mechanisms to determine which mechanisms are most likely to carry the majority of the flux from reactants to products.

The maximum rate analysis was applied to determine the most likely mechanism(s) for N-O bond activation leading to formation of the major product observed experimentally, N_2O, in low temperature NO reduction by H_2 on Pt catalysts.[209, 210] The analysis was first conducted using the data from DFT calculations at high NO-coverage (0.5 ML NO spectators), as this surface environment is expected to be more representative of realistic experimental conditions (see 7.3.1 Nitric Oxide Surface Coverage). The calculated maximum rates are shown in Table 7.2 for the individual elementary steps in all N-O activation mechanisms outlined schematically in Figure 7.5. Table 7.2 also shows the overall reaction for forming the activated complex in each elementary step from gas phase reactants and products, and the resulting rate constant for the overall reaction. For each mechanism, the elementary step with the minimum value of its maximum rate is reported in bold print below the mechanism in Table 7.2 and reported in the bar graph in Figure 7.7.

To account for an estimated error in the DFT calculated activation energy barriers of ±0.2 eV, we calculated the upper and lower bounds of the maximum rates for the slowest elementary step in each mechanism, shown as error bars in Figure 7.7. For simplicity, we increased or decreased the activation energy barriers of all of the elementary steps so that the slowest step would not change throughout the uncertainty analysis. In mechanism 1 the slowest step is direct NO dissociation. The maximum rate for this step is low (2×10^{-29} sec^{-1}) which is more than twelve

orders of magnitude slower than the slowest step in all other mechanisms. Therefore, we eliminate the direct NO dissociation mechanism (mechanism 1) as a possible mechanism for the overall reaction. The slowest steps in mechanisms 2 and 3 are cleavage of the N-O bond in HNO* and NOH*, respectively. Based on the maximum rate calculations, these elementary steps are expected to be slower than the slowest steps in mechanisms 4-6. Additionally, the elementary step involving cleavage of the N-O bond in either HNO* or NOH* competes with the elementary steps involving hydrogenation of these intermediates leading to HNOH*, which occur in mechanisms 4-6. Comparison of the maximum rate for HNO* + * → NH* + O* (r_{max} = 5 x 10^{-16} sec^{-1}) with the maximum rate for HNO* + H* → HNOH* + H* (r_{max} = 5 x 10^{5} sec^{-1}) suggests that the hydrogenation step should be more favorable, and thus mechanism 2 is unlikely to occur. This comparison is closer for NOH*, with maximum rates of 1 x 10^{-10} and 1 x 10^{-5} sec^{-1} for NOH* + * → N* + OH* and NOH* + H* → HNOH* + *, respectively. However, based on this difference of 5 orders of magnitude, we suggest that mechanism 3 is also an unlikely overall reaction mechanism.

Mechanisms 4, 5 and 6 can all occur via step (i) HNO* + H* → HNOH* + * or step (ii) HNO* + H* → NOH* + H* → HNOH*. Because the maximum rates for the elementary steps in (i) are larger than those in (ii), we only consider path (i) in the subsequent analysis of mechanisms 4-6, although we do not exclude the possibility that NOH* could participate. The maximum rate for the slowest step in mechanism 4 (HNOH* + * → NH* + OH*) is 5 x 10^{-7} sec^{-1}. The maximum rate for the slowest steps in mechanisms 5 (HNOH* → N* + $H_2O_{(g)}$, r_{max} = 4 x 10^{-3} sec^{-1}) and 6 (H_2 + 2* → 2H*, r_{max} = 3 x 10^{3} sec^{-1}) are similar, particularly when one accounts for the assumed error in the DFT-calculated activation energy barriers by comparing the upper and lower limits of the maximum rates. Importantly, the barrier for the slowest

elementary step in mechanism 4 (HNOH* + * → NH* + OH*) was found to be highly dependent on the NO surface coverage. The barrier for the elementary step HNOH* + * → NH* + OH* increases from 0.70 eV at low coverage to 1.67 eV at high NO coverage. Furthermore, HNOH* is a large intermediate, which could result in an overestimation of the DFT-calculated high NO-coverage barrier due to repulsive interactions. The concerted step HNOH* → N* + H_2O (mechanism 5) does not occur directly on the low coverage surface. Likewise, the N-O bond breaking step required for mechanism 6, although it is not the slowest step in the mechanism, is also a concerted step that may not occur directly on the low coverage surface. Additional theoretical studies of the coverage dependence of these steps as well as experimental studies of the NO surface coverage under realistic reaction conditions are necessary to conclusively state which of mechanisms 4-6 are most likely.

In summary, based on the maximum rate analysis, mechanisms 1, 2 and 3 are determined to be unlikely for the formation N_2O in NO reduction by H_2 on Pt(111) with 0.5 ML NO spectators. Mechanism 1 occurs via direct NO dissociation and mechanisms 2 and 3 occur via the addition of a single H atom to NO followed by N-O bond scission (in either HNO* or NOH*). The more energetically favorable pathways are suggested to be mechanisms that involve the addition of at least two hydrogen atoms prior to cleavage of the N-O bond. The results of this analysis suggest that HNO* and HNOH* are likely to be important reaction intermediates in NO reduction by H_2.

To further illustrate the importance of considering the most relevant surface coverage, we conducted maximum rate analyses using the DFT-derived data on clean Pt(111) and the same reaction conditions described above for high NO-coverage Pt(111). The maximum rate for the slowest step in mechanism 1, NO* + * → N* + O*, is 8×10^{-4} sec^{-1}. For mechanism 2, the

slowest step is N-O bond-breaking in HNO* (HNO* + * → NH* + O*, r_{max} = 2 x 10^4 sec^{-1}). For all other mechanisms considered on clean Pt(111) the slowest step is NO adsorption, which has a maximum rate of 5 x 10^{10} sec^{-1}. The mechanisms involving concerted elementary steps for N-O bond-breaking in HNOH*, mechanisms 5 and 6, were not considered, because these steps are unlikely to occur directly at low NO coverage. Based on the maximum rates calculated, the direct NO dissociation mechanism (mechanism 1) and N-O bond scission via HNO* (mechanism 2) are unlikely to occur even at low NO coverage. Mechanism 3, however, which proceeds via NOH* dissociation, may be more competitive on clean Pt(111), compared to the high NO coverage system.

The results of our maximum rate analysis are insensitive to the specific conditions used. For example, the conclusions reported do not change if the partial pressures of gas phase NO, H_2, H_2O or N_2O used in the analysis are modified by one order of magnitude, because the conclusions are derived from a comparison of rates that differ by multiple orders of magnitude. The most sensitive parameter in this study is, in fact, the NO surface coverage utilized in the DFT calculations. Therefore one must ensure that the reaction conditions used in the maximum rate analysis are consistent with the surface coverages predicted by the DFT-derived phase diagram and that subsequent DFT calculations are performed on the appropriately modified (by adsorbates) clean surfaces.

Table 7.2 N_2O production in NO reduction by H_2: Maximum rates of elementary steps in competing reaction mechanisms, outlined in Figure 7.5, as calculated from DFT-derived data on Pt(111) with 0.5 ML NO spectators.[a]

Mechanism 1

Step		**Overall Reaction**	**Rate Constant**	$\mathbf{r_{max}}$
1)	$NO + * \rightarrow NO*$	$NO + * \leftrightarrow NO*^{\ddagger}$	$K_1^{\ddagger}$	5×10^{10}
2)	$H_2 + 2* \rightarrow 2H*$	$H_2 + 2* \leftrightarrow 2H*^{\ddagger}$	$K_2^{\ddagger}$	3×10^{3}
3)	**$NO* + * \rightarrow N* + O*$**	**$NO + 2* \leftrightarrow [N*+O*]^{\ddagger}$**	**$K_3^{\ddagger}K_1$**	**2×10^{-29}**
4)	$N* + NO* \rightarrow N_2O + 2*$	$2NO + H_2 + 2* \leftrightarrow [N_2O+2*]^{\ddagger} - H_2O$	$K_4^{\ddagger}K_1^2K_2K_3K_5K_6$	8×10^{32}
5)	$O* + H* \rightarrow OH* + *$	$2NO + 1/2H_2 + 2* \leftrightarrow [OH*+*]^{\ddagger} - N_2O$	$K_5^{\ddagger}K_1^2K_2^{1/2}K_3K_4$	8×10^{27}
6)	$OH* + H* \rightarrow H_2O + 2*$	$2NO + H_2 + 2* \leftrightarrow [H_2O+2*]^{\ddagger} - N_2O$	$K_6^{\ddagger}K_1^2K_2K_3K_4K_5$	7×10^{43}
$\mathbf{min(r_{max})}$				**$\mathbf{2 \times 10^{-29}}$**

Mechanism 2

Step		**Overall Reaction**	**Rate Constant**	$\mathbf{r_{max}}$
1)	$NO + * \rightarrow NO*$	$NO + * \leftrightarrow NO*^{\ddagger}$	$K_1^{\ddagger}$	5×10^{10}
2)	$H_2 + 2* \rightarrow 2H*$	$H_2 + 2* \leftrightarrow 2H*^{\ddagger}$	$K_2^{\ddagger}$	3×10^{3}
3)	$NO* + H* \rightarrow HNO* + *$	$NO + 1/2H_2 + * \leftrightarrow [HNO* + *]^{\ddagger}$	$K_3^{\ddagger}K_1K_2^{1/2}$	6×10^{9}
4)	**$HNO* + * \rightarrow NH* + O*$**	**$NO + 1/2H_2 + 2* \leftrightarrow [NH* + O*]^{\ddagger}$**	**$K_4^{\ddagger}K_1K_2^{1/2}K_3$**	**5×10^{-16}**
5)	$NH* + * \rightarrow N* + H*$	$NO + 3/2H_2 + 2* \leftrightarrow [N* + H*]^{\ddagger} + H_2O$	$K_5^{\ddagger}K_1K_2^{3/2}K_3K_4K_7K_8$	2×10^{22}
6)	$N* + NO* \rightarrow N_2O + 2*$	$2NO + H_2 + 2* \leftrightarrow [N_2O+2*]^{\ddagger} - H_2O$	$K_6^{\ddagger}K_1^2K_2K_3K_4K_5K_7K_8$	8×10^{32}
7)	$O* + H* \rightarrow OH* + *$	$2NO + 1/2H_2 + 2* \leftrightarrow [OH*+*]^{\ddagger} - N_2O$	$K_7^{\ddagger}K_1^2K_2^{1/2}K_3K_4K_5K_6K_8$	8×10^{27}
8)	$OH* + H* \rightarrow H_2O + 2*$	$2NO + H_2 + 2* \leftrightarrow [H_2O+2*]^{\ddagger} - N_2O$	$K_8^{\ddagger}K_1^2K_2K_3K_4K_5K_6K_8$	7×10^{43}
$\mathbf{min(r_{max})}$				**$\mathbf{5 \times 10^{-16}}$**

Mechanism 3

Step		**Overall Reaction**	**Rate Constant**	$\mathbf{r_{max}}$
1)	$NO + * \rightarrow NO*$	$NO + * \leftrightarrow NO*^{\ddagger}$	$K_1^{\ddagger}$	5×10^{10}
2)	$H_2 + 2* \rightarrow 2H*$	$H_2 + 2* \leftrightarrow 2H*^{\ddagger}$	$K_2^{\ddagger}$	3×10^{3}
3)	$NO* + H* \rightarrow HNO* + *$	$NO + 1/2H_2 + * \leftrightarrow [HNO* + *]^{\ddagger}$	$K_3^{\ddagger}K_1K_2^{1/2}$	6×10^{9}
4)	$HNO* \rightarrow NOH*$	$NO + 1/2H_2 + * \leftrightarrow [NOH*]^{\ddagger}$	$K_4^{\ddagger}K_1K_2^{1/2}K_3$	3×10^{10}
5)	**$NOH* + * \rightarrow N* + OH*$**	**$NO + 1/2H_2 + 2* \leftrightarrow [N* + OH*]^{\ddagger}$**	**$K_5^{\ddagger}K_1K_2^{1/2}K_3K_4$**	**1×10^{-10}**
6)	$N* + NO* \rightarrow N_2O + 2*$	$2NO + H_2 + 2* \leftrightarrow [N_2O+2*]^{\ddagger} + H_2O$	$K_6^{\ddagger}K_1^2K_2K_3K_4K_5K_7$	8×10^{32}
7)	$OH* + H* \rightarrow H_2O + 2*$	$2NO + H_2 + 2* \leftrightarrow [H_2O+2*]^{\ddagger} + N_2O$	$K_7^{\ddagger}K_1^2K_2K_3K_4K_5K_6$	7×10^{43}
$\mathbf{min(r_{max})}$				**$\mathbf{1 \times 10^{-10}}$**

Mechanism 4

Step		Overall Reaction	Rate Constant	r_{max}
1)	$NO + * \rightarrow NO*$	$NO + * \leftrightarrow NO*^{\ddagger}$	$K_1^{\ddagger}$	5×10^{10}
2)	$H_2 + 2* \rightarrow 2H*$	$H_2 + 2* \leftrightarrow 2H*^{\ddagger}$	$K_2^{\ddagger}$	3×10^{3}
3)	$NO* + H* \rightarrow HNO* + *$	$NO + 1/2H_2 + * \leftrightarrow [HNO*+*]^{\ddagger}$	$K_3^{\ddagger}K_1K_2^{1/2}$	6×10^{9}
4)	$HNO* + H* \rightarrow HNOH* + *$	$NO + H_2 + 2* \leftrightarrow [HNOH* + *]^{\ddagger}$	$K_4^{\ddagger}K_1K_2K_3$	5×10^{5}
5)	**$HNOH* + * \rightarrow NH* + OH*$**	**$NO + H_2 + 2* \leftrightarrow [NH* + OH*]^{\ddagger}$**	**$K_5^{\ddagger}K_1K_2K_3K_4$**	**5×10^{-7}**
6)	$NH* + * \rightarrow N* + H*$	$NO + 3/2H_2 + 2* \leftrightarrow [N* + H*]^{\ddagger} + H_2O$	$K_6^{\ddagger}K_1K_2^{3/2}K_3K_4K_5K_8$	2×10^{22}
7)	$N* + NO* \rightarrow N_2O + 2*$	$2NO + H_2 + 2* \leftrightarrow [N_2O+2*]^{\ddagger} + H_2O$	$K_7^{\ddagger}K_1^2K_2K_3K_4K_5K_6K_8$	8×10^{32}
8)	$OH* + H* \rightarrow H_2O + 2*$	$2NO + H_2 + 2* \leftrightarrow [H_2O+2*]^{\ddagger} + N_2O$	$K_8^{\ddagger}K_1^2K_2K_3K_4K_5K_6K_7$	7×10^{43}
$min(r_{max})$				**5×10^{-7}**

Mechanism 5

Step		Overall Reaction	Rate Constant	r_{max}
1)	$NO + * \rightarrow NO*$	$NO + * \leftrightarrow NO*^{\ddagger}$	$K_1^{\ddagger}$	5×10^{10}
2)	$H_2 + 2* \rightarrow 2H*$	$H_2 + 2* \leftrightarrow 2H*^{\ddagger}$	$K_2^{\ddagger}$	3×10^{3}
3)	$NO* + H* \rightarrow HNO* + *$	$NO + 1/2H_2 + * \leftrightarrow [HNO*+*]^{\ddagger}$	$K_3^{\ddagger}K_1K_2^{1/2}$	5×10^{9}
4)	$HNO* + H* \rightarrow HNOH* + *$	$NO + H_2 + 2* \leftrightarrow [HNOH* + *]^{\ddagger}$	$K_4^{\ddagger}K_1K_2K_3$	5×10^{5}
5)	**$HNOH* \rightarrow N* + H_2O$**	**$NO + H_2 + * \leftrightarrow [N* + H_2O]^{\ddagger}$**	**$K_5^{\ddagger}K_1K_2K_3K_4$**	**4×10^{-3}**
6)	$N* + NO* \rightarrow N_2O + 2*$	$2NO + H_2 + 2* \leftrightarrow [N_2O+2*]^{\ddagger} + H_2O$	$K_6^{\ddagger}K_1^2K_2K_3K_4K_5$	6×10^{32}
$min(r_{max})$				**4×10^{-03}**

Mechanism 6

Step		Overall Reaction	Rate Constant	r_{max}
1)	$NO + * \rightarrow NO*$	$NO + * \leftrightarrow NO*^{\ddagger}$	$K_1^{\ddagger}$	5×10^{10}
2)	$H_2 + 2* \rightarrow 2H*$	$H_2 + 2* \leftrightarrow 2H*^{\ddagger}$	$K_2^{\ddagger}$	3×10^{3}
3)	$NO* + H* \rightarrow HNO* + *$	$NO + 1/2H_2 + * \leftrightarrow [HNO**]^{\ddagger}$	$K_3^{\ddagger}K_1K_2^{1/2}$	5×10^{9}
4)	**$HNO* + H* \rightarrow HNOH* + *$**	**$NO + H_2 + 2* \leftrightarrow [HNOH**]^{\ddagger}$**	**$K_4^{\ddagger}K_1K_2K_3$**	**5×10^{5}**
5)	$HNOH* + H* \rightarrow NH* + H_2O + *$	$NO + 3/2H_2 + 2* \leftrightarrow [NH* + H_2O*]^{\ddagger}$	$K_5^{\ddagger}K_1K_2^{3/2}K_3K_4$	8×10^{7}
6)	$NH* + * \rightarrow N* + H*$	$NO + 3/2H_2 + 2* \leftrightarrow [N* + H*]^{\ddagger} + H_2O$	$K_6^{\ddagger}K_1K_2^{3/2}K_3K_4K_5$	2×10^{22}
7)	$N* + NO* \rightarrow N_2O + 2*$	$2NO + H_2 + 2* \leftrightarrow [N_2O+2*]^{\ddagger} + H_2O$	$K_7^{\ddagger}K_1^2K_2K_3K_4K_5K_6$	6×10^{32}
$min(r_{max})$				**3×10^{3}**

[a]Rates are calculated at a temperature of 400 K and NO, H_2, H_2O and N_2O partial pressures of 0.005 atm, 0.050 atm, 0.0002 atm and 0.0002 atm, respectively. In each mechanism the slowest step is indicated in bold face.

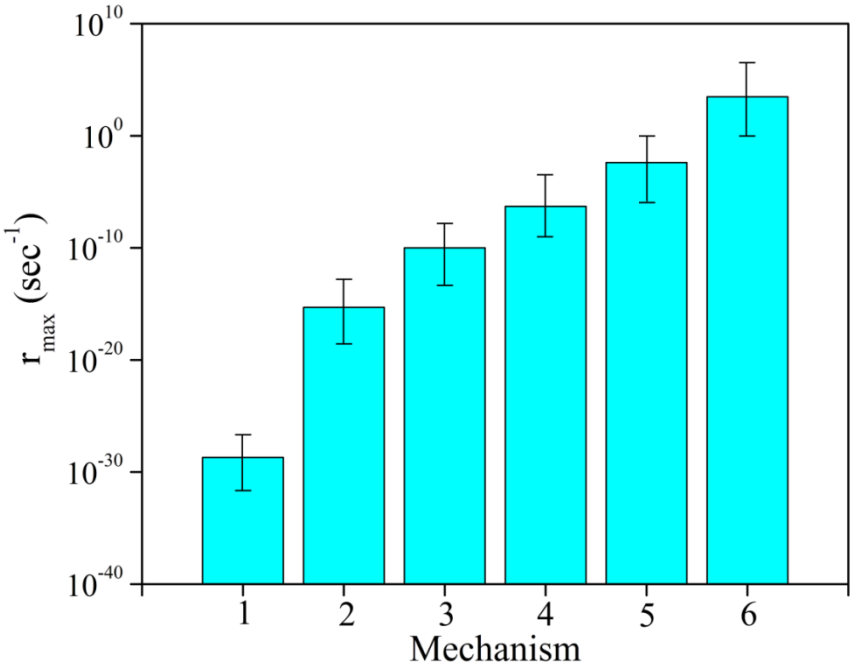

Figure 7.7 Maximum rates of the slowest step in each mechanism, shown in Figure 7.5, on Pt(111) with 0.5 ML NO spectators, calculated using DFT-derived data. The error bars are calculated by reducing (-) and increasing (+) the DFT-derived activation energy barriers of all steps in the mechanism by 0.2 eV. Rates are calculated at a temperature of 400 K and NO, H_2, H_2O and N_2O partial pressures of 0.005 atm, 0.050, 0.0002 atm and 0.0002 atm, respectively.

Importantly, the elementary step for N_2O formation invoked throughout this study (N* + NO* → N_2O + 2*) may be overly simplistic. Because two of the three proposed reaction mechanisms (mechanisms 4 and 6) on high NO coverage Pt(111) require breaking the N-H bond in NH* to form N*, an elementary step with a high activation energy barrier (E_A = 1.86 eV), we investigated alternative routes leading to N_2O from NH*. One possible step is formation of an N-N bond with a neighboring NO* to produce the intermediate HNNO*, which may be particularly relevant because NO* is expected to be present at high coverage on Pt(111). The HNNO* can then undergo N-H bond scission to produce $N_2O_{(g)}$ and an adsorbed H atom. Interestingly, the calculated maximum rate for forming HNNO* (3 x 10^{35} sec^{-1}) is more than 10 orders of magnitude greater than the maximum rate calculated for NH* + * → N* + H* (2 x 10^{22} sec^{-1}). A detailed analysis of product formation mechanisms through a DFT-based full

microkinetic model, and comparison with experimentally determined trends, is presented in the next chapter (Chapter 8) to determine the most likely steps involved in N_2O formation following the initial N-O bond scission.

Lastly, we note that combining this theoretical study with experiments probing the effect of the Pt particle size on the activity and selectivity of the reaction, would provide insight into the role of various types of surface sites in the reaction. The Pt(111) facet is the most stable and therefore most abundant facet of a Pt nanoparticle, but may not be the active site for the overall reaction. If a significant particle size effect is found, additional theoretical studies analogous to the one presented here should be conducted for a Pt slab with defect sites, such as steps and kinks. These sites are likely to display very different reaction energetics, compared to Pt(111), and consequently may provide alternative reaction pathways to those predicted here.

7.4 Conclusions

In this chapter, we showed that Pt(111) is mostly covered by adsorbed NO during NO reduction by H_2 at low temperatures (e.g., 400 K) and typical pressures. The high NO coverage destabilizes adsorbed intermediates. In general, high coverage causes the activation energy barriers for bond-breaking steps to increase and the activation energy barriers for bond-making steps to decrease, relative to the respective barriers on clean Pt(111). A maximum rate analysis, a procedure for assessing the most likely reaction pathway(s) from DFT-derived kinetic and thermodynamic data, is performed to probe the reaction mechanisms leading to N_2O formation at low temperatures in NO reduction by H_2. The results of this analysis suggest that the addition of at least two H atoms is required prior to cleavage of the N-O bond. The intermediates HNO*

and HNOH* are likely important intermediates in the pathway to N_2O formation from NO and H_2 at low temperatures.

Chapter 8 Microkinetic Analysis of Nitric Oxide Reduction by Hydrogen on Platinum[i]

8.1 Introduction

As described in the previous chapter, supported Pt catalysts utilized for the low temperature reduction of NO by H_2 demonstrate high conversion of NO but low selectivity toward N_2 and undesirable production of N_2O and NH_3.[208-210] The reaction selectivity is dependent on the reaction temperature and the NO to H_2 ratio. At typical low temperature experimental conditions (e.g., 400 K and an NO:H_2 ratio of ~1:2), N_2 and NH_3 are the most thermodynamically favorable products, whereas N_2O is the major product observed. Therefore, low temperature selectivity toward N_2 is kinetically limited. Elucidating the origin of the kinetically-limited selectivity requires a detailed understanding of the reaction pathways.

Under low temperature reaction conditions, the Pt(111) surface is expected to be highly covered with adsorbed NO. In Chapter 7, we showed that this high NO coverage impacts the reaction energetics on Pt(111) in a number of ways. Specifically, and relative to the low coverage surface, on the high NO-coverage surface adsorbed intermediates tend to be destabilized, activation energy barriers for bond-breaking steps are generally increased, and

[i] Farberow, C. A.; Dumesic, J. A..; Mavrikakis, M. (in preparation). Contributions by C. A. Farberow: 100% of DFT calculations, microkinetic modeling, experiments and manuscript writing.

activation energy barriers for bond-making steps are generally decreased. Based on this behavior, we predicted that the reaction mechanism for NO reduction by H_2 on Pt(111) at high NO coverage likely occurs through a H-assisted path, beginning with the addition of at least two hydrogen atoms to NO followed by N-O bond scission.

In this chapter, we expand the study of NO reduction by H_2 on Pt to include a DFT-based microkinetic model and comparison with experimentally determined reaction kinetics and trends. In addition to describing the H-assisted path leading to N-O activation, this study includes an analysis of possible reaction mechanisms governing the experimentally observed selectivity. Previous reports of NO reduction by H_2 on Pt catalysts have generally assumed that the products, N_2O, N_2 and NH_3, are formed from adsorbed atomic N via hydrogenation and N-N bond formation steps.[211, 212, 223, 224] We consider these paths, as well as alternative mechanisms going through an NH* intermediate (instead of N*) and involving an HNNO* intermediate as a precursor to N_2O and N_2. The selectivity trends for the various mechanisms and reaction orders are compared with those observed experimentally.

8.2 Methods

8.2.1 Density Functional Theory Calculations

Density functional theory calculations were performed using the Vienna ab-initio Simulation Package (VASP).[31, 59] Details of the DFT-GGA calculation methods and results, beyond those described here, can be found in Chapter 7 (see 7.2 Methods). To model a high NO-coverage environment in the DFT calculations, we carried out DFT calculations (PW91-GGA) which included 0.5 ML NO 'spectators' in the periodic unit cell. Except where indicated otherwise, for

the 2 x 2 unit cell used in this study, 0.5 ML NO spectators corresponds to two NO adsorbates in addition to the adsorbate(s) studied for a thermochemistry calculation or participating in the elementary step for the respective CI-NEB calculation. The NO spectator species were relaxed during the calculation. The reported binding energies of adsorbates on Pt(111) with 0.5 ML co-adsorbed NO spectators were calculated with respect to a relaxed Pt(111) slab with 0.5 ML adsorbed NO ($E_{0.5ML\ NO/Pt(111)}$) and the respective adsorbate in the gas phase (E_{gas}).

$$BE = E_{total} - E_{0.5\ ML\ NO/Pt(111)} - E_{gas}$$

where E_{total} is the total energy of the slab with the adsorbate and 0.5 ML co-adsorbed NO. Minimum energy pathways and activation energy barriers for all elementary steps were calculated using the climbing-image nudged elastic band (CI-NEB) method.[33, 34] The calculations which include two NO spectator molecules will be referred to throughout this chapter as high NO coverage calculations.

8.2.2 Experiments

The alumina-supported platinum catalyst ($Pt/\gamma\text{-}Al_2O_3$) used in this study was prepared by incipient wetness impregnation of $\gamma\text{-}Al_2O_3$ with $Pt(NH_3)_4(NO_3)_2$ dissolved in water. The catalyst composition was prepared to yield 0.3 wt % Pt. Following wet impregnation, the catalyst was dried at 383 K for 1 h, calcined in flowing air at 773 K for 2 h, reduced in flowing H_2 at 623 K for 2 h, and then passivated with flowing 1% O_2 in He at 298 K. CO chemisorption, performed using a Micromeritics ASAP 2020, was used to determine the number of surface metallic platinum atoms per gram of catalyst. The number of catalytic Pt sites was taken to be equal to 3/2 times the total irreversible CO uptake based on the saturation coverage of CO on Pt(111) (15.5 μmol Pt sites/g).[225, 226]

Reaction kinetic experiments were carried out using a quarter-inch stainless steel tube flow reactor at 413 K. Prior to reaction kinetics experiments, the catalyst was reduced *in situ* at 623 K (2 h). Reaction kinetics data were collected at atmospheric pressure (101.3 kPa). The flow rates of all gases were fixed using calibrated mass flow controllers. Inlet compositions between 0.20 and 1.35% NO and 1.50 and 13.10% H_2 were used with the balance gas of He. The mass of catalyst used and total flow rate were varied in each experiment such that all experimental data were collected at similar low conversions (8 - 21%). Reactant and product gas analyses for NO, N_2 and N_2O were carried out using a gas chromatograph (Shimadzu 2014) with a HayeSep DB 100/120 column (Alltech) and a thermal conductivity detector. Analysis of the NH_3 composition was carried out using an FTIR (Nicolet 6700) with a flow-through cell. The kinetic data were free of mass transfer limitations, as verified by the Madon-Boudart test.[227] All overall turnover frequencies (TOF) in this study are reported with respect to nitric oxide consumption (TOF_{NO}).

8.2.3 Microkinetic Model

A mean-field microkinetic model was used to describe the experimentally measured NO turnover frequencies and selectivities to N_2O, NH_3 and N_2. Details of the microkinetic modelling procedure implemented have been described previously.[36, 228] The reactor was modeled as a transient continuous stirred tank reactor (CSTR), because the numerical methods used are robust when solving a system of simultaneous differential equations rather than the system of algebraic and differential equations required to solve a plug flow reactor (PFR). This approach is adequate for probing the reaction mechanism in this study, as all experimental kinetic data were collected at low conversion of NO (< ~20%).

The microkinetic model was composed of 24 surface elementary reaction steps (Table 8.1) and 4 adsorption/desorption steps, involving 17 reaction intermediates. The input to the model was the total inlet molar gas flow rate per Pt surface site, in units of s^{-1}, inlet mole fractions of NO, H_2 and He, reaction temperature and pressure. The DFT-derived activation energy barriers of elementary steps and the enthalpies and entropies of gas phase species and adsorbates were used as initial guesses for the model. For adsorbed species, the enthalpy was calculated by adding the DFT-derived binding energy to the DFT-calculated enthalpy of the species in the gas phase. The entropy of an adsorbate was approximated as its local entropy: the DFT-calculated entropy of the species in the gas phase minus its 3D translational entropy. The gas phase entropy was calculated from the DFT-derived vibrational frequencies of the respective states and used to fit the parameters of the Shomate equation, using the procedure suggested by Grabow and Mavrikakis.[20] The Shomate parameters were subsequently used to calculate the temperature correction to the enthalpies. The maximum surface coverage in the microkinetic model was restricted to 1 ML and multilayer adsorption was not considered. We assumed that all adsorbates occupy one surface site. The pre-exponential factor for surface reactions was set to 1 x 10^{13} sec^{-1} ($\sim \frac{k_B T}{h}$), which assumes that the entropy change to form the transition state is negligible. The pre-exponential factor for the adsorption steps was set to 1 x 10^{7} sec^{-1}, based on the calculated probability of a collision between a gas molecule and a surface and assuming a sticking coefficient equal to one. The units of all partial pressures were in atmospheres (based on the choice of the standard state for the entropy calculations). The activation energy barriers used as initial guesses in the model are the results of the CI-NEB DFT-GGA, PW91 calculations. The enthalpies and activation energy barriers used in the model do not include corrections for zero point energy.

In the microkinetic model, we simultaneously solve six differential equations for the gaseous (NO, H_2, N_2O, N_2, NH_3 and H_2O) molar flow rates together with 16 differential equations for the fractional surface coverage of adsorbed intermediates, and a site balance equation. Because the binding energy of an NO molecule on Pt(111) is strongly dependent on its own coverage, which is predicted to be high, we incorporated the coverage dependence of the NO binding energy into the model. The functional dependence is generated from a polynomial fit of the DFT-calculated differential binding energy of NO at coverages of 0.25, 0.50, 0.75 and 1.00 ML NO. The zero coverage NO binding energy (y-intercept) is set equal to the value calculated at 0.25 ML NO binding energy, assuming that a coverage of 0.25 ML NO is a good approximation of the low coverage limit.

$$BE_{NO}(\theta_{NO}) = 1.338 * \theta_{NO}^3 + 0.347 * \theta_{NO}^2 + 0.224 * \theta_{NO} - 1.899$$

All other adsorbate binding energies used in the model, as well as the activation energy barriers for elementary steps, were calculated with 0.5 ML NO spectators, as described above.

The solution to the microkinetic model gives the exit molar flow rates of NO, H_2, N_2O, N_2, NH_3 and H_2O and the coverages of the 16 intermediates. The binding energies and activation energy barriers are adjusted to minimize the difference between the model predicted and experimentally measured TOFs of NO, N_2O, N_2 and NH_3 and the reaction orders for NO and H_2, From this microkinetic analysis, information is obtained about possible reaction mechanisms and the coverage of the surface intermediates under the conditions utilized in our experiments. Importantly, the model predicts a surface with high NO coverage, in agreement with the explicit incorporation of spectator NO molecules in the DFT calculations.

Table 8.1 Binding energies (BE) with respect to the respective gas phase species and activation energy barriers (E_A) for elementary steps considered, all calculated with DFT-PW91 on Pt(111) with 0.5 ML NO spectators. These values were used as the initial parameters in the microkinetic model.

Parameters

Step Number	*Surface Reaction*	*E_A (eV)*
1	$H_2 + 2* \rightarrow 2H*$	0.65
2	$NO* + * \rightarrow N* + O*$	3.52
3	$NO* + H* \rightarrow HNO*$	0.36
4	$NOH* + * \rightarrow N* + OH*$	1.81
5	$HNO* + * \rightarrow O* + NH*$	2.26
6	$HNO* + NO* \rightarrow NOH* + NO*$	0.21
7	$NOH* + H* \rightarrow HNOH* + *$	1.24
8	$HNO* + H* \rightarrow HNOH* + *$	0.43
9	$HNOH* + * \rightarrow NH* + OH*$	1.67
10	$HNOH* \rightarrow N* + H_2O$	1.36
11	$HNOH* + H* \rightarrow NH* + H_2O + *$	0.69
12	$N* + N* \rightarrow N_2*$	1.60
13	$NO* + N* \rightarrow N_2O + 2*$	0.07
14	$N* + H* \rightarrow NH* + *$	0.54
15	$NH* + H* \rightarrow NH_2* + *$	0.95
16	$NH_2* + H* \rightarrow NH_3* + *$	0.31
17	$NO* + NH* \rightarrow HNNO* + *$	0.69
18[a]	$HNNO* \rightarrow N_2O + H*$	1.13
19	$HNNO* + NO* \rightarrow NOH* + N_2O + *$	0.61
20[a]	$HNNO* + * \rightarrow NNH* + O*$	1.32
21	$NNH* \rightarrow N_2 + H*$	0.44
22	$NNH* + NO* \rightarrow N_2 + NOH* + *$	0.40
23	$O* + H* \rightarrow OH* + *$	0.22
24	$OH* + H* \rightarrow H_2O* + *$	0.15

Intermediate	*BE (eV)*
NO	-1.05
NOH	-2.00
HNO	-1.00
HNOH	-0.90
N	-3.55
O	-3.39
H	-2.44
NH	-3.12
NH_2	-1.82
NH_3	-0.66
OH	-2.06
H_2O	0.00
N_2	0.00
N_2O	0.00
H_2	0.00
HNNO	-0.26
NNH	-0.73

[a]Because HNNO is a large intermediate, the 'high-coverage' calculations for these steps only include one additional NO spectator in the unit cell.

8.3 Results

The conditions used in the reaction kinetics experiments and the resulting NO turnover frequencies and selectivities are reported in Table 8.2. The reaction orders with respect to NO at H_2 pressures of 3 kPa to 12.5 kPa are between 0.07 – 0.20 (see Table 8.3). The reaction orders with respect to H_2 at NO pressures of 0.3 kPa to 0.7 kPa are between 0.67 – 0.72. The experimentally determined selectivity trends for the ratio of the NH_3 turnover frequency to the N_2O turnover frequency ($\frac{TOF_{NH_3}}{TOF_{N_2O}}$) increase with increasing H_2 pressure and decrease with increasing NO pressure. The experimental data for the ratio of the N_2 turnover frequency to the N_2O turnover frequency ($\frac{TOF_{N_2}}{TOF_{N_2O}}$), although somewhat scattered due to the low levels of N_2 produced in the experiments, indicate that the trend for $\frac{TOF_{N_2}}{TOF_{N_2O}}$ either slightly decreases or remains nearly constant as the H_2 pressure increases. Over the range of experimental conditions used in this study, there is no discernable trend for $\frac{TOF_{N_2}}{TOF_{N_2O}}$ with changing NO pressure.

Table 8.2 Reaction conditions, turnover frequencies (TOF) and selectivities obtained from kinetics experiments on Pt/γ-Al_2O_3 at 413 K and 101.3 kPa. All rates and selectivities are the steady-state values; 'y' denotes mole fraction at the reactor inlet.

						Selectivity	
				Total Flow	TOF_{NO}	$\frac{TOF_{N_2}}{TOF_{N_2O}}$	$\frac{TOF_{NH_3}}{TOF_{N_2O}}$
Experiment	y(NO)	y(H2)	y(He)	s^{-1}	min^{-1}		
1	0.0019	0.0147	0.9833	155	3.07	0.092	0.232
2	0.0029	0.0293	0.9678	132	4.73	0.077	0.177
3	0.0029	0.0297	0.9675	296	4.05	0.091	0.162
4	0.0028	0.0486	0.9486	187	5.12	0.062	0.258
5	0.0029	0.0708	0.9262	227	7.89	0.067	0.250
6	0.0030	0.1055	0.8916	298	9.35	0.080	0.311
7	0.0029	0.1182	0.8789	339	11.42	0.056	0.299
8	0.0048	0.0278	0.9673	100	4.13	0.098	0.187
9	0.0038	0.0298	0.9664	118	4.76	0.080	0.197
10	0.0048	0.0524	0.9428	137	7.18	0.057	0.177
11	0.0049	0.0974	0.8977	221	13.15	0.084	0.232
12	0.0050	0.1258	0.8692	218	10.73	0.067	0.241
13	0.0057	0.0286	0.9658	99	4.28	0.062	0.084
14	0.0069	0.0305	0.9625	85	5.44	0.070	0.098
15	0.0069	0.0308	0.9623	56	4.98	0.071	0.102
16	0.0068	0.0481	0.9452	110	7.27	0.062	0.125
17	0.0069	0.1251	0.8681	289	13.88	0.053	0.113
18	0.0134	0.0420	0.9446	68	5.87	0.083	0.065
19	0.0133	0.0842	0.9025	67	8.73	0.053	0.123
20	0.0135	0.1308	0.8557	90	14.78	0.054	0.140

8.3.1 Optimized Reaction Mechanism on High NO Coverage Pt(111)

Without any adjustment to the DFT-derived parameters, the microkinetic model predicts NO turnover frequencies that are up to an order of magnitude higher than the NO turnover frequencies measured experimentally. The model predicts that N_2O is produced along the pathway shown in Figure 8.1, and the predicted rate of NH_3 or N_2 production is negligible. The

predicted path for N-O activation, via step 11 (HNOH* + H* → NH* + H_2O + *) is in agreement with our previous conclusions, reported in Chapter 7, from a maximum rate analysis. The predicted surface coverage is ~0.72 – 0.74 ML NO, ~0.001 ML H, and ~0.24 – 0.27 ML vacant sites.

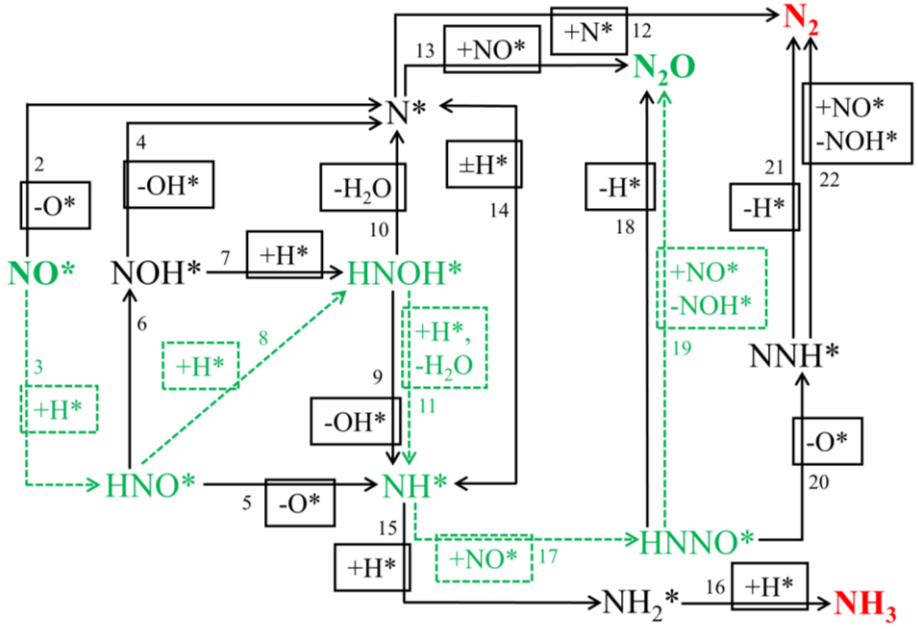

Figure 8.1 Reaction network for NO reduction by H_2 on Pt catalysts. The green dashed lines indicate the predicted predominant mechanism without any changes to the DFT parameters, whereas the solid black lines indicate possible paths in the model that do not contribute to the flux. Products written in red are not predicted to be produced by the model, but are observed experimentally. Step numbers refer to the step numbers provided in Table 8.1.

To generate a model that more closely predicts the experimentally observed NO turnover frequencies and formation of N_2 and NH_3 as minor products, adjustments to the DFT-derived parameters are necessary. Sensitivity analyses show that the most sensitive parameters for the overall rate of NO consumption, TOF_{NO}, are the binding energy of H* and HNOH* and the activation energy barrier for step 11 (HNOH* + H* → NH* + H_2O + *). Increasing the activation energy barrier for step 11 by 0.08 eV results in model-predicted turnover frequencies for NO consumption of the same order of magnitude as those found experimentally. However,

the model-predicted reaction order with respect to NO, (0.40 - 0.27) and reaction order with respect to H_2 (1.11 - 0.81) are both inconsistent with the experimentally determined reaction orders reported in Table 8.3. Therefore, further adjustments to the DFT-calculated parameters are required.

To obtain the reaction orders with respect to NO observed experimentally (0.07-0.20), the surface must be highly covered with NO, such that the site-blocking term in the denominator of the NO consumption rate equation becomes dominant. To achieve this coverage, the binding energy at the limit of zero NO-coverage (i.e., the intercept of the equation for the NO binding energy as a function of the NO coverage) is adjusted in the model from -1.90 eV (calculated at 0.25 ML NO) to -3.00 eV. This adjustment corresponds to a stabilization of NO adsorption at all NO coverages on Pt(111) of 1.10 eV. The large adjustment may be partially attributed to uncertainty in the polynomial equation for the coverage dependence of the NO binding energy, particularly at high NO coverages, but nevertheless provides a first indication that the active site might be a facet more reactive than Pt(111). Additional modifications to the DFT-calculated parameters required to generate a model that predicts the experimentally determined H_2 order and overall TOF_{NO} include the binding energy of H* and the activation energy barriers for step 8 ($HNO^* + H^* \rightarrow HNOH^* + *$) and step 11 ($HNOH^* + H^* \rightarrow NH^* + H_2O + *$). The H* binding energy is increased from -2.44 eV to -2.66 eV. The activation energy barrier for $HNO^* + H^* \rightarrow HNOH^* + *$ is increased from 0.43 eV to 0.61 eV, and the activation energy barrier for the step $HNOH^* + H^* \rightarrow NH^* + H_2O + *$ is lowered from 0.69 eV to 0.49 eV. The modification to the two activation energy barriers causes the second hydrogen addition to become rate-controlling, rather than the third H addition, thus reducing the model-predicted reaction order with respect to

H_2. A parity plot showing the agreement between the experimental and model-predicted TOF_{NO}, following the described changes to the DFT-derived parameters, is shown in Figure 8.2.

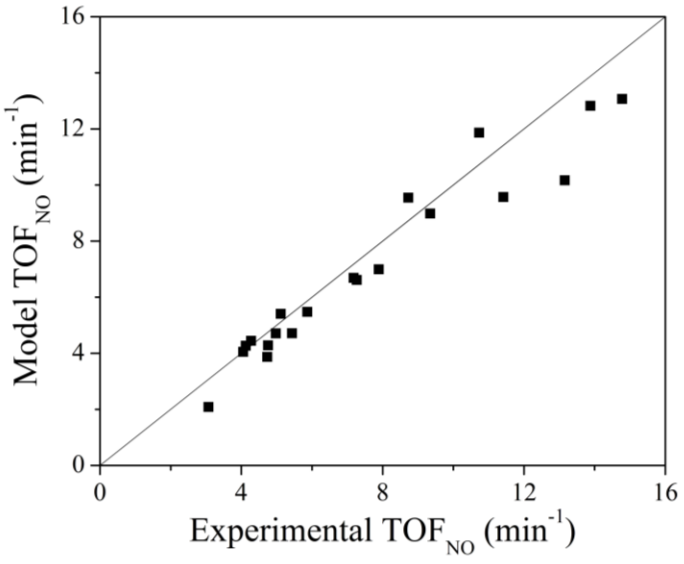

Figure 8.2 Parity plot of experimental and microkinetic model calculated NO turnover frequencies. Experimental data from Table 8.2. Quality of fit: $R^2 = 0.90$.

Table 8.3 Experimental ($Pt/\gamma\text{-}Al_2O_3$) and microkinetic model-predicted (high NO coverage Pt(111)) reaction orders at 413 K and a total pressure of 101.3 kPa. The microkinetic model results are obtained after adjustment of the DFT-derived parameters for Pt(111), as explained in the text.

	H_2 reaction order			**NO reaction order**	
NO Pressure (kPa)	*Expt.*	*Model*	*H_2 Pressure (kPa)*	*Expt.*	*Model*
0.3	0.67 ± 0.08	0.64	3.0	0.14 ± 0.11	0.19
0.5	0.72 ± 0.17	0.68	5.0	0.07 ± 0.18	0.00
0.7	0.70 ± 0.04	0.71	12.5	0.20 ± 0.09	0.20

Additional adjustments to the DFT-derived parameters are necessary to obtain the experimentally observed TOFs of N_2O, NH_3 and N_2 and the related selectivity trends. With the aforementioned adjusted parameters, all of the NO consumed is converted to N_2O. To increase the predicted rate of N_2 formation to experimental levels, the activation energy barrier for N_2

formation via HNNO* + * → NNH* + O* is decreased by 0.70 eV from 1.32 eV to 0.62 eV, and the activation energy barrier for N_2O formation via HNNO* + NO* → N_2O + NOH* + * is increased by 0.09 eV from 0.61 eV to 0.70 eV. To increase the predicted TOF_{NH3}, the activation energy barrier for the step NH* + H* → NH_2* + * is lowered by 0.26 eV from 0.95 eV to 0.69 eV. The resulting pathways for the formation of N_2O, N_2 and NH_3 are shown schematically in Figure 8.3.

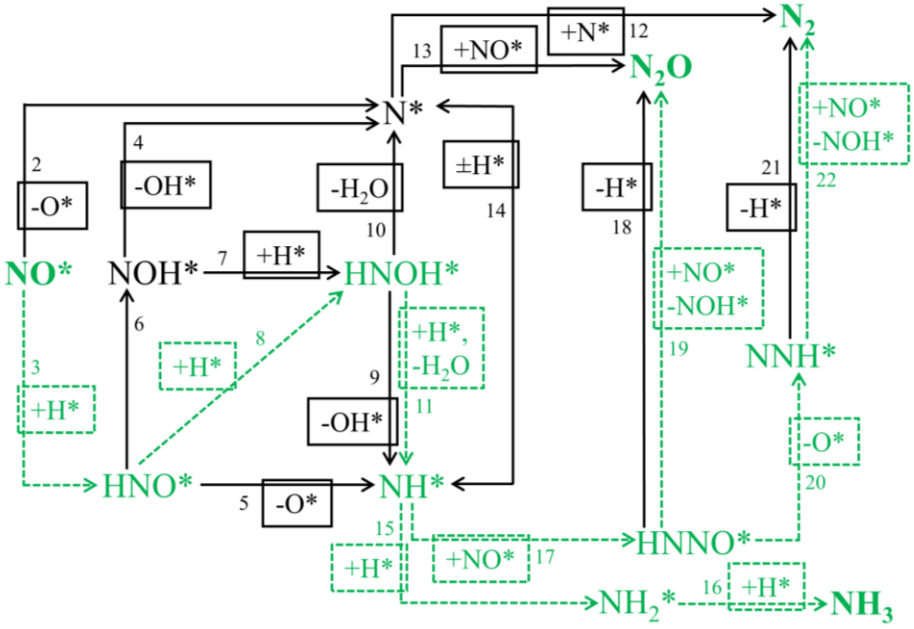

Figure 8.3 Reaction network for NO reduction by H_2 on Pt catalysts. The green dashed lines indicate the predicted mechanism from the microkinetic model with the DFT parameters optimized (see Table 8.4) to obtain the best description of the experimental kinetics, whereas the solid black lines indicate possible paths in the model that do not contribute to the flux. The elementary step numbering shown on the arrows refers to the elementary step numbers provided in Table 8.1.

A summary of all of the changes to the DFT-derived parameters required to describe the experimental trends is reported in Table 8.4. Comparisons between the experimental and model predicted selectivity trends, specifically the ratio of N_2 to N_2O turnover frequencies ($\frac{TOF_{N_2}}{TOF_{N_2O}}$) and the ratio of NH_3 to N_2O turnover frequencies ($\frac{TOF_{NH_3}}{TOF_{N_2O}}$), are shown in Figure 8.4. As described

above, the experimental data for $\frac{TOF_{N_2}}{TOF_{N_2O}}$ is somewhat scattered, but still shows that the trend for $\frac{TOF_{N_2}}{TOF_{N_2O}}$ either slightly decreases or remains nearly constant as the H_2 pressure increases. This trend is in general agreement with the slight decrease in $\frac{TOF_{N_2}}{TOF_{N_2O}}$ predicted by the model. The model also predicts that $\frac{TOF_{N_2}}{TOF_{N_2O}}$ decreases with increasing NO pressure, but this trend is not clearly discernable from the experimental data. The trend for $\frac{TOF_{NH_3}}{TOF_{N_2O}}$ shows even better agreement between the experimental data and the model: $\frac{TOF_{NH_3}}{TOF_{N_2O}}$ increases with increasing H_2 pressure and decreases with increasing NO pressure in both the experiments and in the model predictions. The model slightly over-predicts $\frac{TOF_{NH_3}}{TOF_{N_2O}}$ at the lowest NO pressure of 0.30 kPa and slightly under-predicts the ratio at higher NO pressures, but the experimental trends are captured well by the model.

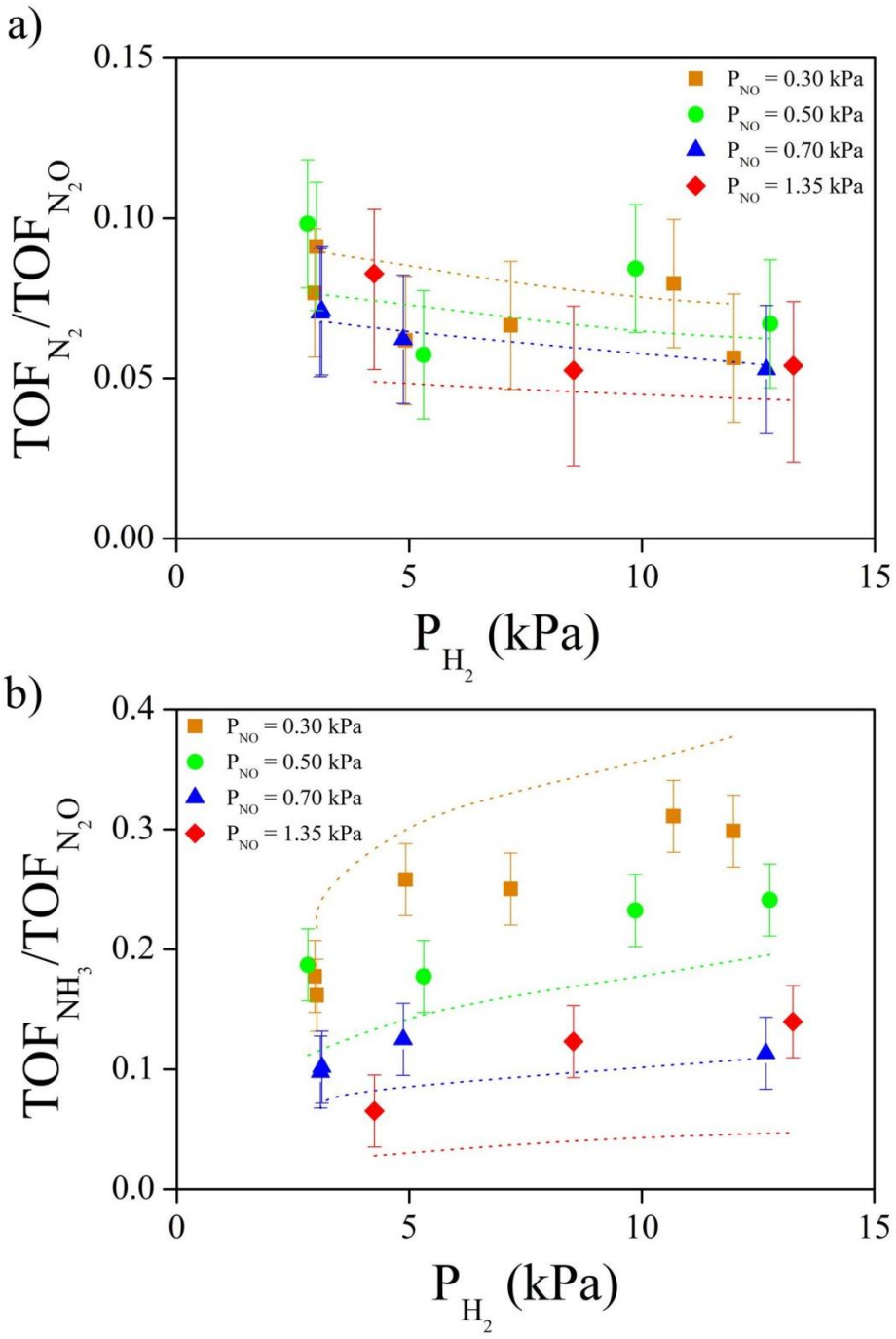

Figure 8.4 Selectivity (a) N_2/N_2O and (b) NH_3/N_2O in NO reduction by H_2 on Pt/γ-Al_2O_3 at 413 K and 101.3 kPa. Points indicate experimental data and dotted lines are predictions from the microkinetic model with the optimized DFT-derived parameters reported in Table 8.4.

Table 8.4 DFT-derived parameter values on high NO coverage Pt(111) and the respective parameter values required to generate a microkinetic model that describes the experimental trends for NO reduction by H_2 on Pt/γ-Al_2O_3 at 413 K and 101.3 kPa (see Figure 8.4).

		E_A (eV)	
Step Number	*Surface Reaction*	*DFT*	*Model*
8	HNO* + H* → HNOH* + *	0.43	0.61
11	HNOH* + H* → NH* + H_2O + *	0.69	0.49
15	NH* + H* → NH_2* + *	0.95	0.69
19	HNNO* + NO* → NOH* + N_2O + *	0.61	0.70
20	HNNO* + * → NNH* + O*	1.32	0.62

		BE (eV)	
	Intermediate	*DFT*	*Model*
	H	-2.44	-2.66
	NO		Stabilized BE at all NO coverages by 1.10 eV

8.3.2 Alternative Mechanism I: N-O Activation via HNOH* + * → NH* + OH*

Alternative H-assisted N-O activation mechanisms in which the rate-controlling step is preceded by the addition of no more than two hydrogen atoms to NO can predict the experimentally-determined reaction order with respect to H_2 (ie, the addition of a third hydrogen atom in or before the rate-controlling step causes the H_2 order to become too large at high NO coverage) (see Table 8.3). Therefore, we also considered adjusting the activation energy barrier for elementary step 9 (HNOH* + * → NH* + OH*) such that it would become the overall rate-controlling step. This option required a decrease in the activation energy barrier for this step by 0.97 eV to 0.70 eV. This modification to the DFT-derived value is more significant than all of the changes already described. In fact, the resulting activation energy barrier is equivalent to the value calculated at low NO coverage for this step (see 7.3.3 Elementary Steps: Reaction Energies

and Activation Energy Barriers). Therefore, based on the DFT results, it is unlikely that this elementary step plays a role in the overall reaction at low temperatures on Pt(111), although we note that a mechanism going through this elementary step can produce the experimentally-determined reaction orders.

8.3.3 Alternative Mechanism II: Product Formation via N*

We also investigated the selectivity trends and changes to the DFT-derived parameters required if the NO conversion pathways proceed through N*, as suggested in the literature on various transition metals for NO reduction by H_2.[211, 212, 223, 224] Because the N-O activation mechanism predicted proceeds through HNOH* to give NH* via step 11, the most straightforward way to produce N* is the reverse of step 14 (NH* + * → N* + H*). Obtaining N* from NH* via this path requires modification of a variety of DFT-derived parameters: stabilization of adsorbed N* by ~0.3 eV (to a BE of -3.85 eV), destabilization of NH* by ~0.2 eV (to a BE of -2.92 eV), lowering of the activation energy barrier for step 14 by ~0.3 eV, and increasing the activation energy barrier of step 17 (NH* + NO* → HNNO* + *) by ~0.2 eV. These changes to the binding energies and to the activation energy barrier for step 14 are required because step 14, in the reverse direction, is endothermic by 1.32 eV and has an activation energy barrier of 1.86 eV on Pt(111) at high NO coverage. The activation energy barrier for step 17 must be increased because the high coverage of NO makes this step favorable, even though it has a relatively high activation energy barrier.

Because significant changes to numerous DFT-derived parameters are required to generate a model that predicts flux through the step NH* + * → N* + H*, we considered N-O activation via Step 10 (HNOH* → N* + H_2O) as an alternative path for production of N* as the precursor to

product formation. To obtain NO turnover frequencies that are the same order of magnitude as those observed experimentally, the DFT-derived activation energy barrier for this step was decreased by 0.50 eV to 0.86 eV. In addition, the activation energy barrier for step 11 (HNOH* + H* → NH* + H_2O + *) was increased by 0.27 eV to 0.93 eV to prevent significant flux through that elementary step which would then produce NH*. In addition to these changes, the NO* binding energy at 0 coverage is adjusted to -3.01 eV and the H* binding energy is adjusted to -2.68 eV. These changes to the binding energies are similar to those in the first optimized mechanism, and are necessary to predict the experimentally observed TOFs and to obtain good agreement with the NO and H_2 reaction orders. Without any additional adjustments to the DFT derived parameters for product formation, all of the NO converted would form N_2O via step 13 (N* + NO* → N_2O + 2*). This step is favorable because the DFT-derived activation energy barrier is only 0.08 eV and the NO coverage is high. To generate a model that predicts the amount of N_2 observed experimentally from adsorbed N*, the activation energy barrier for step 13 was increased by ~0.5 eV and the activation energy barrier for step 12 (2N* → N_2 + 2*) was lowered by ~1.5 eV. Additional adjustments required to predict values of TOF_{NH3} in agreement with those observed experimentally included decreasing the barrier of step 14 (N* + H* → NH* + *), decreasing the barrier of step 15 (NH* + H* → NH_2* + *) and increasing the barrier of step 17 (NH* + NO* → HNNO* + *) by ~0.1 eV, ~0.3 eV and ~0.3 eV, respectively.

This model predicts that the $\frac{TOF_{N_2}}{TOF_{N_2O}}$ should increase with increasing hydrogen pressure (Figure 8.5). In contrast, the experimental data for $\frac{TOF_{N_2}}{TOF_{N_2O}}$ either slightly decreases or remains nearly constant as the H_2 pressure increases. Therefore, mechanisms in which N_2 and N_2O are produced via N* (step 12 and step 13, respectively), in addition to requiring large changes (~1.5

eV) to the DFT-derived parameters, do not agree with the experimental selectivity trends. This discrepancy is a result of the use of hydrogen atoms in the elementary steps required to form N*, as described above for the various hydrogen-assisted N-O activation pathways. If instead, N_2 is formed via HNNO* in step 20 (HNNO* + * → NNH* + O*), the higher fraction of vacant sites on the catalyst surface at lower H_2 pressures favor N_2 formation over N_2O. Thus, the model that produces N_2 via HNNO predicts that $\frac{TOF_{N_2}}{TOF_{N_2O}}$ decreases with increasing H_2 pressure (Figure 8.4a), in general agreement with the experimental trend.

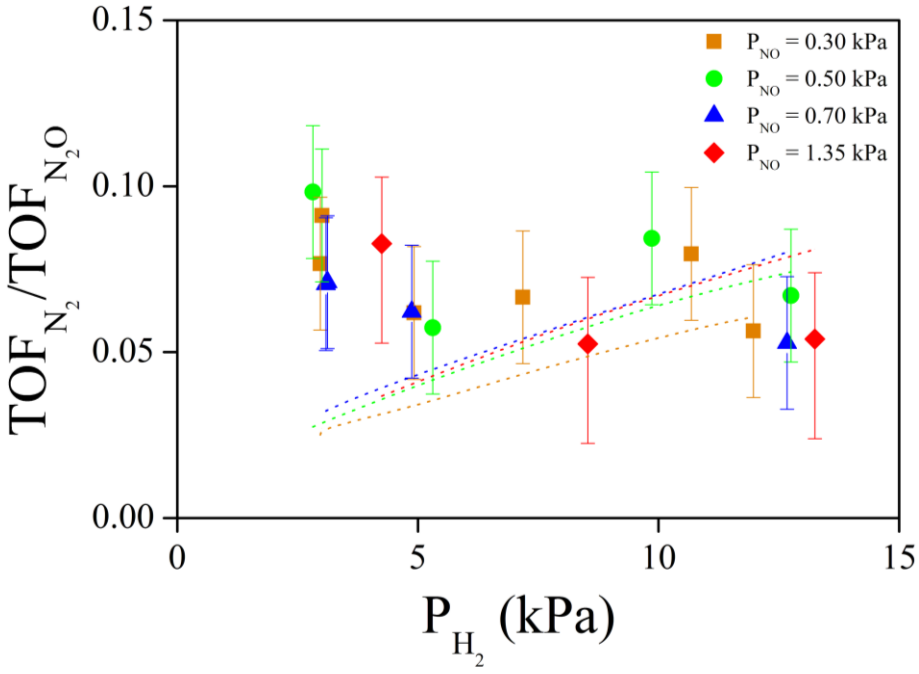

Figure 8.5 N_2 selectivity (N_2/N_2O) in NO reduction by H_2 on Pt/γ-Al_2O_3 at 413 K and 101.3 kPa. Points indicate experimental data and dotted lines are predictions from the microkinetic model with all products formed through N* (Alternative mechanism II). The lack of agreement between the experimental and model-predicted selectivity trend for N_2/N_2O suggests that the N* pathways considered do not contribute significantly.

8.3.4 Rate Determining and Selectivity Determining Steps

To identify the rate-controlling step(s) in the overall reaction, based on the reaction pathways which best described the experimental data (see Figure 8.3 and Table 8.4), we calculated

Campbell's degree of rate control.[229] This quantifies the relative change in the overall rate of a reaction upon changing the forward and reverse rate constants for one step while holding the equilibrium constant of that step and the rate constants of all other elementary steps constant. Campbell's degree of rate control, $X_{RC,i}$ for an elementary step i, is defined as

$$X_{RC,i} = \frac{k_i}{TOF_{NO}}\left(\frac{\delta TOF_{NO}}{\delta k_i}\right)_{K_{i,eq},k_{j\neq i}}$$

where k_i is the rate constant for step (i) and $K_{i,eq}$ is the equilibrium constant for step (i). We calculated $X_{RC,i}$ for each step (i), for each experimental condition and subsequently averaged $X_{RC,i}$ from all experimental conditions. An analogous analysis was applied to identify the steps that control the selectivity trends. We define the degree of N_2 ($X_{N_2,i}$) and NH_3 ($X_{NH_3,i}$) selectivity control as:

$$X_{N_2,i} = \frac{k_i}{\frac{TOF_{N_2}}{TOF_{N_2O}}}\left(\frac{\delta \frac{TOF_{N_2}}{TOF_{N_2O}}}{\delta k_i}\right)_{K_{i,eq},k_{j\neq i}} \qquad X_{NH_3,i} = \frac{k_i}{\frac{TOF_{NH_3}}{TOF_{N_2O}}}\left(\frac{\delta \frac{TOF_{NH_3}}{TOF_{N_2O}}}{\delta k_i}\right)_{K_{i,eq},k_{j\neq i}}$$

The results of this analysis, reported in Table 8.5, show that step 8 (HNO* + H* → HNOH* + *) is the rate-controlling step for NO consumption, though the rate of H_2 dissociative adsorption also effects the overall rate. The selectivity to N_2 versus N_2O is controlled by step 20 (HNNO* + * → NNH* + O*) and step 19 (HNNO* + NO* → N_2O + NOH* + *). The selectivity to NH_3 versus N_2O is primarily controlled by step 15 (NH* + H* → NH_2* + *) and step 19 (HNNO* + NO* → N_2O + NOH* + *).

Table 8.5 Campbell's degree of rate control (X_{RC}) and the degree of selectivity control for elementary steps (X_{N2} and X_{NH3}), averaged over all experimental conditions reported in Table 8.1. This analysis was conducted using the DFT-derived data with the changes reported in Table 8.4, such that the flux proceeds through the pathways shown in Figure 8.3.

Step Number	Surface Reaction	X_{RC}	X_{N_2}	X_{NH_3}
1	$H_2 + 2^* \rightarrow 2H^*$	0.16	-0.02	0.13
8	$HNO^* + H^* \rightarrow HNOH^* + *$	0.81	0.08	0.10
15	$NH^* + H^* \rightarrow NH_2^* + *$	-0.08	0.00	0.97
19	$HNNO^* + NO^* \rightarrow NOH^* + N_2O + *$	0.07	-0.98	-0.90
20	$HNNO^* + * \rightarrow NNH^* + O^*$	0.00	1.00	0.00

8.3.5 On the Nature of the Active Site

The large stabilization of NO* and H* required on Pt(111) combined with the significant changes to some of the DFT-derived parameters indicate that the high NO coverage Pt(111) surface may not be an appropriate model of the active sites for NO reduction by H_2 on Pt/γ-Al_2O_3. The Pt(111) surface is the most thermodynamically stable facet of Pt, but it is less reactive than more open facets and defect sites. A more open surface, such as Pt(100) or Pt(211) may be a better representation of where the surface chemistry occurs on a Pt nanoparticle under realistic reaction conditions. In fact, and for example, at 1 ML NO coverage the differential binding energy for the fourth NO on a (2x2) unit cell of Pt(100) is -0.84 eV, whereas NO does not bind (endothermic differential binding energy) on Pt(111) at 1 ML coverage. Importantly, the key conclusions described above for the product formation pathways based on the selectivity trends for $\frac{TOF_{N_2}}{TOF_{N_2O}}$ should be relevant to these alternative active sites.

8.4 Conclusions

A DFT-derived mean-field microkinetic model was used to explore the reaction pathways responsible for describing the experimental reaction kinetics data, collected at atmospheric pressure and 413 K, for NO reduction by H_2 on Pt/γ-Al_2O_3. To be consistent with the model's prediction that NO is dominating the surface coverage under reaction conditions, the DFT-PW91 derived parameters used in the model were calculated at high NO coverage Pt(111). Our analysis suggests that the reaction pathway capturing the experimentally-measured NO turnover frequencies and reaction orders with respect to NO and H_2 proceeds through a H-assisted mechanism involving the addition of three hydrogen atoms prior to N-O bond cleavage. The elementary step involving the addition of the second hydrogen atom to adsorbed NO is the overall rate-controlling step. Reaction pathways involving the formation of N_2 and N_2O via an adsorbed nitrogen atom, which are generally suggested in the literature, predict a trend for the N_2 to N_2O ratio with increasing H_2 pressure that does not agree with our experimental observations. In contrast, formation of N_2 and N_2O via an HNNO intermediate leads to selectivity trends for all three products that are in agreement with experimental observations. To summarize, in the pathway that best describes the experimental kinetics data, N_2O is formed via NO* → HNO* → HNOH* → NH* → HNNO* → N_2O, N_2 is formed via NO* → HNO* → HNOH* → HNNO* → NNH* → N_2 and NH_3 is produced via NO* → HNO* → HNOH* → NH* → NH_2* → NH_3. The DFT-derived value of the activation energy barrier for N_2 formation from HNNO on high NO coverage Pt(111) had to be lowered by 0.70 eV to predict the experimental values of the N_2 TOFs. In addition, the extent of stabilization of adsorbed NO (by 1.10 eV) required to generate a model that predicts the experimentally determined reaction orders with respect to NO and H_2,

indicates that a more open and reactive facet of Pt may provide a better model for the active site on the γ-Al_2O_3 supported Pt catalyst.

Chapter 9 References

1. International Energy Agency, *World Energy Outlook 2013*. 2013

2. National Academy of Sciences, *Climate Change: Evidence & Causes*. The National Academies Press: Washington DC, 2014.

3. Alonso, D. M.; Bond, J. Q.; Dumesic, J. A. *Green Chemistry* **2010,** 12, 1493-1513.

4. Huber, G. W.; Iborra, S.; Corma, A. *Chemical Reviews* **2006,** 106, 4044-4098.

5. Corma, A.; Iborra, S.; Velty, A. *Chemical Reviews* **2007,** 107, 2411-2502.

6. Cusumano, J. A.; Dalla Betta, R. A.; Levy, R. B., *Catalysis in Coal Conversion*. Academic Press, Inc.: New York, 1978.

7. Lunsford, J. H. *Catalysis Today* **2000,** 63, 165-174.

8. Besenbacher, F.; Chorkendorff, I.; Clausen, B. S.; Hammer, B.; Molenbroek, A. M.; Nørskov, J. K.; Stensgaard, I. *Science* **1998,** 279, 1913-1915.

9. Song, C. S. *Catalysis Today* **2006,** 115, 2-32.

10. Wang, W.; Wang, S.; Ma, X.; Gong, J. *Chemical Society Reviews* **2011,** 40, 3703-3727.

11. Adzic, R. R., Electrocatalysis. In *Frontiers in Electrochemistry*, Lipkowski, J.; Ross, P. N., Eds. Wiley-VCH: New York, 1998; Vol. 5, pp 197-242.

12. Song, C. S. *Catalysis Today* **2002,** 77, 17-49.

13. Heck, R. M.; Farrauto, S. T.; Gulati, S. T., *Catalytic Air Pollution Control: Commercial Technology*. Wiley: New Jersey, 2009.

14. Roy, S.; Hegde, M. S.; Madras, G. *Applied Energy* **2009,** 86, 2283-2297.

15. Nørskov, J. K.; Bligaard, T.; Rossmeisl, J.; Christensen, C. H. *Nature Chemistry* **2009,** 1, 37-46.

16. Mavrikakis, M. *Nature Materials* **2006,** 5, 847-848.

17. Behrens, M.; Studt, F.; Kasatkin, I.; Kuhl, S.; Havecker, M.; Abild-Pedersen, F.; Zander, S.; Girgsdies, F.; Kurr, P.; Kniep, B. L.; Tovar, M.; Fischer, R. W.; Nørskov, J. K.; Schlogl, R. *Science* **2012,** 336, 893-897.

18. Gokhale, A. A.; Dumesic, J. A.; Mavrikakis, M. *Journal of the American Chemical Society* **2008,** 130, 1402-1414.

19. Alayoglu, S.; Nilekar, A. U.; Mavrikakis, M.; Eichhorn, B. *Nature Materials* **2008,** 7, 333-338.

20. Grabow, L. C.; Mavrikakis, M. *ACS Catalysis* **2011,** 1, 365-384.

21. Honkala, K.; Hellman, A.; Remediakis, I. N.; Logadottir, A.; Carlsson, A.; Dahl, S.; Christensen, C. H.; Nørskov, J. K. *Science* **2005,** 307, 555-558.

22. Mavrikakis, M.; Hammer, B.; Nørskov, J. K. *Physical Review Letters* **1998,** 81, 2819-2822.

23. Van Santen, R. A. *Accounts of Chemical Research* **2009,** 42, 57-66.

24. Liu, Z.-P.; Hu, P. *Journal of the American Chemical Society* **2001,** 123, 12596-12604.

25. Greeley, J.; Stephens, I. E. L.; Bondarenko, A. S.; Johansson, T. P.; Hansen, H. A.; Jaramillo, T. F.; Rossmeisl, J.; Chorkendorff, I.; Nørskov, J. K. *Nature Chemistry* **2009,** 1, 552-556.

26. Sholl, D. S.; Steckel, J. A., *Density Functional Theory: A Practical Introduction*. John Wiley & Sons, Inc.: Hoboken, New Jersey, 2009.

27. Asthagiri, A.; Janik, M. J., *Computational Catalysis*. The Royal Society of Chemistry: Cambridge, UK, 2014.

28. Hammer, B.; Nørskov, J. K. *Advances in Catalysis* **2000,** 45, 71-129.

29. Greeley, J.; Nørskov, J. K.; Mavrikakis, M. *Annual Review of Physical Chemistry* **2002,** 53, 319-348.

30. Perdew, J. P.; Wang, Y. *Physical Review B* **1992,** 45, 13244-13249.

31. Kresse, G.; Furthmüller, J. *Computational Materials Science* **1996,** 6, 15-50.

32. Morgan, D., Introduction to Atomistic Modeling course notes. University of Wisconsin-Madison, 2009.

33. Henkelman, G.; Jonsson, H. *Journal of Chemical Physics* **2000,** 113, 9978-9985.

34. Henkelman, G.; Uberuaga, B. P.; Jonsson, H. *Journal of Chemical Physics* **2000,** 113, 9901-9904.

35. Dumesic, J. A.; Rudd, D. F.; Aparicio, L. M.; Rekoske, J. E.; Trevino, A. A., *The Microkinetics of Heterogeneous Catalysis*. American Chemical Society: Washington D.C., 1993.

36. Gokhale, A. A.; Kandoi, S.; Greeley, J. P.; Mavrikakis, M.; Dumesic, J. A. *Chemical Engineering Science* **2004,** 59, 4679-4691.

37. Conner, W. C.; Falconer, J. L. *Chemical Reviews* **1995,** 95, 759-788.

38. Rozanov, V. V.; Krylov, O. V. *Russian Chemical Reviews* **1997,** 66, 107-119.

39. Cortright, R. D.; Davda, R. R.; Dumesic, J. A. *Nature* **2002,** 418, 964.

40. Ait-Ichou, I.; Formenti, M.; Pommier, B.; Teichner, S. J. *Journal of Catalysis* **1985,** 91, 293-307.

41. Hilmen, A. M.; Schanke, D.; Holmen, A. *Catalysis Letters* **1996,** 38, 143-147.

42. Cheng, H.; Chen, L.; Cooper, A. C.; Sha, X.; Pez, G. P. *Energy & Environmental Science* **2008,** 1, 338.

43. Jung, K.-D.; Bell, A. T. *Journal of Catalysis* **2000,** 193, 207-223.

44. Ioannides, T.; Verykios, X. E. *Journal of Catalysis* **1993,** 143, 175-186.

45. Levy, R. B.; Boudart, M. *Journal of Catalysis* **1974,** 32, 304-314.

46. Higazy, A.; Kassem, M.; Sayed, M. *Journal of Physics and Chemistry of Solids* **1992,** 53, 549-554.

47. Kanellopoulos, J.; Gottert, C.; Schneider, D.; Knorr, B.; Prager, D.; Ernst, H.; Freude, D. *Journal of Catalysis* **2008,** 255, 68-78.

48. Ertl, G. *Angewandte Chemie International Edition* **2008,** 47, 3524-3535.

49. Li, S.-C.; Chu, L.-N.; Gong, X.-Q.; Diebold, U. *Science* **2010,** 328, 882-4.

50. Li, S.-C.; Zhang, Z.; Sheppard, D.; Kay, B. D.; White, J. M.; Du, Y.; Lyubinetsky, I.; Henkelman, G.; Dohnálek, Z. *Journal of the American Chemical Society* **2008,** 130, 9080-9088.

51. Wendt, S.; Matthiesen, J.; Schaub, R.; Vestergaard, E.; L{\ae}gsgaard, E.; Besenbacher, F.; Hammer, B. *Physical Review Letters* **2006,** 96, 066107.

52. Vurens, G. H.; Salmeron, M.; Somorjai, G. A. *Surface Science* **1988,** 201, 129-144.

53. Weiss, W.; Somorjai, G. A. *Journal of Vacuum Science & Technology A* **1993,** 11, 2138-2144.

54. Knudsen, J.; Merte, L. R.; Grabow, L. C.; Eichhorn, F. M.; Porsgaard, S.; Zeuthen, H.; Vang, R. T.; Laegsgaard, E.; Mavrikakis, M.; Besenbacher, F. *Surface Science* **2010,** 604, 11-20.

55. Merte, L. R.; Knudsen, J.; Grabow, L. C.; Vang, R. T.; Laegsgaard, E.; Mavrikakis, M.; Besenbacher, F. *Surface Science* **2009,** 603, L15-L18.

56. Lægsgaard, E.; Besenbacher, F.; Mortensen, K.; Stensgaard, I. *Journal of Microscopy-Oxford* **1988,** 152, 663-669.

57. Nie, S.; Feibelman, P. J.; Bartelt, N. C.; Thürmer, K. *Physical Review Letters* **2010,** 105, 026102.

58. Dudarev, S. L.; Botton, G. A.; Savrasov, S. Y.; Humphreys, C. J.; Sutton, A. P. *Physical Review B* **1998,** 57, 1505-1509.

59. Kresse, G.; Furthmüller, J. *Physical Review B* **1996,** 54, 11169-11186.

60. Giordano, L.; Pacchioni, G.; Goniakowski, J.; Nilius, N.; Rienks, E. D. L.; Freund, H.-J. *Physical Review B* **2007,** 76, 75416.

61. Merte, L. R.; Grabow, L. C.; Peng, G.; Knudsen, J.; Zeuthen, H.; Kudernatsch, W.; Porsgaard, S.; Lægsgaard, E.; Mavrikakis, M.; Besenbacher, F. *Journal of Physical Chemistry C* **2011,** 115, 2089-2099.

62. Zhang, W.; Li, Z.; Luo, Y.; Yang, J. *Journal of Physical Chemistry C* **2009,** 113, 8302-8305.

63. Blochl, P. E. *Physical Review B* **1994,** 50, 17953-17979.

64. Kresse, G.; Joubert, D. *Physical Review B* **1999,** 59, 1758-1775.

65. CRC Handbook of Chemistry and Physics. 95 ed.; CRC Press: Boca Raton, FL, 2014; pp 4-150.

66. Galloway, H. C.; Benitez, J. J.; Salmeron, M. *Surface Science* **1993,** 298, 127-133.

67. Daschbach, J. L.; Dohnálek, Z.; Liu, S.-R.; Smith, R. S.; Kay, B. D. *Journal of Physical Chemistry B* **2005,** 109, 10362-10370.

68. Joseph, Y.; Kuhrs, C.; Ranke, W.; Ritter, M.; Weiss, W. *Chemical Physics Letters* **1999,** 314, 195-202.

69. Leist, U.; Ranke, W.; Al-Shamery, K. *Physical Chemistry Chemical Physics* **2003,** 5, 2435-2441.

70. Henderson, M. A. *Surface Science Reports* **2002,** 46, 1-308.

71. Huang, W. X.; Ranke, W. *Surface Science* **2006,** 600, 793-802.

72. Daiguji, H. *Nature Nanotechnology* **2010,** 5, 831-832.

73. Whitesides, G. M. *Nature* **2006,** 442, 368-373.

74. Verdaguer, A.; Sacha, G. M.; Bluhm, H.; Salmeron, M. *Chemical Reviews* **2006,** 106, 1478-510.

75. Thiel, P. A.; Madey, T. E. *Surface Science Reports* **1987,** 7, 211-385.

76. Hodgson, A.; Haq, S. *Surface Science Reports* **2009,** 64, 381-451.

77. Carrasco, J.; Hodgson, A.; Michaelides, A. *Nature Materials* **2012,** 11, 667-674.

78. Carrasco, J.; Michaelides, A.; Forster, M.; Haq, S.; Raval, R.; Hodgson, A. *Nature Materials* **2009,** 8, 427-31.

79. Cerdá, J.; Michaelides, A.; Bocquet, M.-L.; Feibelman, P.; Mitsui, T.; Rose, M.; Fomin, E.; Salmeron, M. *Physical Review Letters* **2004,** 93, 116101.

80. Xie, X.; Li, Y.; Liu, Z.-Q.; Haruta, M.; Shen, W. *Nature* **2009,** 458, 746-749.

81. Brown, G. E.; Henrich, V. E.; Casey, W. H.; Clark, D. L.; Eggleston, C.; Felmy, A.; Goodman, D. W.; Grätzel, M.; Maciel, G.; McCarthy, M. I.; Nealson, K. H.; Sverjensky, D. a.; Toney, M. F.; Zachara, J. M. *Chemical Reviews* **1999,** 99, 77-174.

82. Salmeron, M.; Bluhm, H.; Tatarkhanov, M.; Ketteler, G.; Shimizu, T. K.; Mugarza, A.; Deng, X.; Herranz, T.; Yamamoto, S.; Nilsson, A. *Faraday Discuss.* **2009,** 141, 221-229.

83. Joseph, Y.; Ranke, W.; Weiss, W. *Journal of Physical Chemistry B* **2000,** 104, 3224-3236.

84. Xu, L.; Wu, Z.; Zhang, W.; Jin, Y.; Yuan, Q.; Ma, Y.; Huang, W. *Journal of Physical Chemistry C* **2012,** 116, 22921-22929.

85. Meyer, B.; Marx, D.; Dulub, O.; Diebold, U.; Kunat, M.; Langenberg, D.; Wöll, C. *Angewandte Chemie International Edition* **2004,** 43, 6642-5.

86. Parkinson, G. S.; Novotný, Z.; Jacobson, P.; Schmid, M.; Diebold, U. *Journal of the American Chemical Society* **2011,** 133, 12650-5.

87. Rim, K. T.; Eom, D.; Chan, S.-W.; Flytzani-Stephanopoulos, M.; Flynn, G. W.; Wen, X.-D.; Batista, E. R. *Journal of the American Chemical Society* **2012,** 134, 18979-18985.

88. Matthiesen, J.; Hansen, J.; Wendt, S.; Lira, E.; Schaub, R.; Lægsgaard, E.; Besenbacher, F.; Hammer, B. *Physical Review Letters* **2009,** 102, 2-5.

89. Ma, H.; Brugger, T.; Berner, S.; Ding, Y.; Iannuzzi, M.; Hutter, J.; Osterwalder, J.; Greber, T. *ChemPhysChem* **2010,** 11, 399-403.

90. Picolin, A.; Busse, C.; Redinger, A.; Morgenstern, M.; Michely, T.; Picolin, A.; Busse, C.; Redinger, A.; Morgenstern, M.; Michely, T. *Journal of Physical Chemistry C* **2009,** 113, 691-697.

91. Rienks, E. D. L.; Nilius, N.; Rust, H.-P.; Freund, H.-J. *Physical Review B* **2005,** 71, 241404.

92. Nilius, N.; Rienks, E. D. L.; Rust, H. P.; Freund, H.-J. *Physical Review Letters* **2005,** 95, 66101.

93. Lin, X.; Nilius, N. *Journal of Physical Chemistry C* **2008,** 112, 15325-15328.

94. Merte, L. R.; Peng, G.; Bechstein, R.; Rieboldt, F.; Farberow, C. A.; Grabow, L. C.; Kudernatsch, W.; Wendt, S.; Laegsgaard, E.; Mavrikakis, M.; Besenbacher, F. *Science* **2012,** 336, 889-893.

95. Giovambattista, N.; Debenedetti, P. G.; Rossky, P. J. *Journal of Physical Chemistry B* **2007,** 111, 9581-9587.

96. Giordano, L.; Pacchioni, G.; Goniakowski, J.; Nilius, N.; Rienks, E. D. L.; Freund, H. J. *Physical Review Letters* **2008,** 101, 026102.

97. Ong, S.; Zhao, X.; Eisenthal, K. B. *Chemical Physics Letters* **1992,** 191, 327-335.

98. Michaelides, A.; Morgenstern, K. *Nature Materials* **2007,** 6, 597-601.

99. Nauta, K.; Miller, R. E. *Science* **2000,** 287, 293-295.

100. Petrenko, V. F.; Whitworth, R. W., *Physics of Ice*. Oxford University Press: Oxford, 2002.

101. Zhao, H.-X.; Kong, X.-J.; Li, H.; Jin, Y.-C.; Long, L.-S.; Zeng, X. C.; Huang, R.-B.; Zheng, L.-S. *Proceedings of the National Academy of Sciences* **2011,** 108, 3481-3486.

102. Buch, V.; Groenzin, H.; Li, I.; Shultz, M. J.; Tosatti, E. *Proceedings of the National Academy of Sciences* **2008,** 105, 5969-5974.

103. Znamenskiy, V. S.; Green, M. E. *Journal of Chemical Theory and Computation* **2007,** 3, 103-114.

104. Albrecht, L.; Chowdhury, S.; Boyd, R. J. *Journal of Physical Chemistry A* **2013,** 117, 10790-10799.

105. Gilli, P.; Pretto, L.; Bertolasi, V.; Gilli, G. *Accounts of Chemical Research* **2009,** 42, 33-44.

106. Giordano, L.; Goniakowski, J.; Suzanne, J. *Physical Review Letters* **1998,** 81, 1271-1273.

107. Cabrera-Sanfelix, P.; Fernández-Serra, M. V.; Arnau, A.; Sánchez-Portal, D. *Physical Review B* **2010,** 82, 125432.

108. Clay, C.; Haq, S.; Hodgson, A. *Physical Review Letters* **2004,** 92, 046102.

109. Michaelides, A.; Hu, P. *Journal of the American Chemical Society* **2001,** 123, 4235-4242.

110. Kimmel, G. A.; Petrik, N. G.; Dohnálek, Z.; Kay, B. D. *Physical Review Letters* **2005,** 95, 166102.

111. Kimmel, G. A.; Matthiesen, J.; Baer, M.; Mundy, C. J.; Petrik, N. G.; Smith, R. S.; Dohnálek, Z.; Kay, B. D. *Journal of the American Chemical Society* **2009,** 131, 12838-44.

112. Hu, X. L.; Michaelides, A. *Surface Science* **2008,** 602, 960-974.

113. Feibelman, P. J. *Journal of Physical Chemistry C* **2013,** 117, 6088-6095.

114. Haria, N. R.; Grest, G. S.; Lorenz, C. D. *Journal of Physical Chemistry C* **2013,** 117, 6096-6104.

115. Döbereiner, J. W.; Schweigg, J. **1923,** 39, 1.

116. Somorjai, G. A.; Li, Y., *Introduction to Surface Chemistry and Catalysis*. 2nd ed.; John Wiley & Sons, Inc.: Hoboken, New Jersy, 2010.

117. Vielstich, W.; Lamm, A.; Gasteiger, H. A., *Handbook of Fuel Cells: Fundamentals, Technology, Applications*. Wiley: West Sussex, 2003.

118. Zhang, J.; Sasaki, K.; Sutter, E.; Adzic, R. R. *Science* **2007,** 315, 220-222.

119. Wang, Y. X.; Balbuena, P. B. *Journal of Physical Chemistry B* **2005,** 109, 18902-18906.

120. Campos-Martin, J. M.; Blanco-Brieva, G.; Fierro, J. L. G. *Angewandte Chemie International Edition* **2006,** 45, 6962-6984.

121. Samanta, C. *Applied Catalysis A-General* **2008,** 350, 133-149.

122. Landon, P.; Collier, P. J.; Papworth, A. J.; Kiely, C. J.; Hutchings, G. J. *Chemical Communications* **2002**, 2058-2059.

123. Henkel, H.; Weber, W. US Pat. 1108752, 1914.

124. Park, S.; Yoo, J.; Lee, W.; Chang, J.; Park, U.; Lee, C. US Pat. 5972305, 1999.

125. Lunsford, J. H. *Journal of Catalysis* **2003,** 216, 455-460.

126. Burch, R.; Ellis, P. R. *Applied Catalysis B-Environmental* **2003,** 42, 203-211.

127. Paparatto, G.; D'Aloisio, R.; Alberti, G. D.; Furlin, P.; Arca, V.; Buzzoni, R.; Meda, L. EP Pat. 0978316 1999.

128. Zhou, B.; Lee, L. US Pat. 6168775, 2001.

129. Choudhary, V. R.; Samanta, C. *Journal of Catalysis* **2006,** 238, 28-38.

130. Liu, Q. S.; Lunsford, J. H. *Journal of Catalysis* **2006,** 239, 237-243.

131. Edwards, J. K.; Solsona, B. E.; Landon, P.; Carley, A. F.; Herzing, A.; Kiely, C. J.; Hutchings, G. J. *Journal of Catalysis* **2005,** 236, 69-79.

132. Edwards, J. K.; Solsona, B.; Ntainjua N, E.; Carley, A. F.; Herzing, A. A.; Kiely, C. J.; Hutchings, G. J. *Science* **2009,** 323, 1037-1041.

133. Rankin, R. B.; Greeley, J. *ACS Catalysis* **2012,** 2, 2664-2672.

134. McIntyre, J. A. US Pat. 5512263, 1996.

135. Melada, S.; Pinna, F.; Strukul, G.; Perathoner, S.; Centi, G. *Journal of Catalysis* **2005,** 235, 241-248.

136. Abate, S.; Centi, G.; Perathoner, S.; Frusteri, F. *Catalysis Today* **2006,** 118, 189-197.

137. Abate, S.; Melada, S.; Centi, G.; Perathoner, S.; Pinna, F.; Strukul, G. *Catalysis Today* **2006,** 117, 193-198.

138. Gao, H.; Lin, Y. S.; Li, Y.; Zhang, B. *Industrial & Engineering Chemistry Research* **2004,** 43, 6920-6930.

139. Mancera, L. A.; Behm, R. J.; Groß, A. *Physical Chemistry Chemical Physics* **2013,** 15, 1497-1508.

140. Nørskov, J. K.; Rossmeisl, J.; Logadottir, A.; Lindqvist, L.; Kitchin, J. R.; Bligaard, T.; Jonsson, H. *Journal of Physical Chemistry B* **2004,** 108, 17886-17892.

141. Ford, D. C.; Nilekar, A. U.; Xu, Y.; Mavrikakis, M. *Surface Science* **2010,** 604, 1565.

142. Nyberg, C.; Tengstal, C. G. *Journal of Chemical Physics* **1984,** 80, 3463-3488.

143. Staykov, A.; Kamachi, T.; Ishihara, T.; Yoshizawa, K. *Journal of Physical Chemistry C* **2008,** 112, 19501-19505.

144. Li, J.; Staykov, A.; Ishihara, T.; Yoshizawa, K. *Journal of Physical Chemistry C* **2011,** 115, 7392-7398.

145. Ham, H. C.; Hwang, G. S.; Han, J.; Nam, S. W.; Lim, T. H. *Journal of Physical Chemistry C* **2009,** 113, 12943-12945.

146. Todorovic, R.; Meyer, R. J. *Catalysis Today* **2011,** 160, 242-248.

147. Zea, H.; Lester, K.; Datye, A. K.; Rightor, E.; Gulotty, R.; Waterman, W.; Smith, M. *Applied Catalysis A-General* **2005,** 282, 237-245.

148. Sales, E. A.; Jove, J.; Mendes, M. J.; Bozon-Verduraz, F. *Journal of Catalysis* **2000,** 195, 88-95.

149. Sheth, P. A.; Neurock, M.; Smith, C. M. *Journal of Physical Chemistry B* **2005,** 109, 12449-12466.

150. Hammer, B.; Hansen, L. B.; Nørskov, J. K. *Physical Review B* **1999,** 59, 7413-7421.

151. Vanderbilt, D. *Physical Review B* **1990,** 41, 7892-7895.

152. Payne, M. C.; Teter, M. P.; Allan, D. C.; Arias, T. A.; Joannopoulos, J. D. *Reviews of Modern Physics* **1992,** 64, 1045-1097.

153. Curtarolo, S.; Morgan, D.; Ceder, G. *Calphad-Computer Coupling of Phase Diagrams and Thermochemistry* **2005,** 29, 163-211.

154. Müller, S.; Zunger, A. *Physical Review Letters* **2001,** 87, 165502.

155. Neugebauer, J.; Scheffler, M. *Physical Review B* **1992,** 46, 16067-16080.

156. Bengtsson, L. *Physical Review B* **1999,** 59, 12301-12304.

157. Greeley, J.; Mavrikakis, M. *Surface Science* **2003,** 540, 215-229.

158. Kubas, G. J. *Accounts of Chemical Research* **1988,** 21, 120-128.

159. Schmidt, P. K.; Christmann, K.; Kresse, G.; Hafner, J.; Lischka, M.; Groß, A. *Physical Review Letters* **2001,** 87, 096103.

160. Khan, N. A.; Shaikhutdinov, S.; Freund, H. J. *Catalysis Letters* **2006,** 108, 159-164.

161. Chen, A. C.; Adams, B. D.; Ostrom, C. K.; Chen, S. A. *Journal of Physical Chemistry C* **2010,** 114, 19875-19882.

162. Xu, Y.; Greeley, J.; Mavrikakis, M. *Journal of the American Chemical Society* **2005,** 127, 12823-12827.

163. Wouda, P. T.; Schmid, M.; Nieuwenhuys, B. E.; Varga, P. *Surface Science* **1999,** 423, L229-L235.

164. Chinta, S.; Lunsford, J. H. *Journal of Catalysis* **2004,** 225, 249-255.

165. Laursen, A. B.; Man, I. C.; Trinhammer, O. L.; Rossmeisl, J.; Dahl, S. *Journal of Chemical Education* **2011,** 88, 1711-1715.

166. Coulthard, I.; Sham, T. K. *Physical Review Letters* **1996,** 77, 4824-4827.

167. Mavrikakis, M.; Stoltze, P.; Nørskov, J. K. *Catalysis Letters* **2000,** 64, 101-106.

168. Chen, M. S.; Kumar, D.; Yi, C. W.; Goodman, D. W. *Science* **2005,** 310, 291-293.

169. Zhong, D. Y.; Franke, J. H.; Podiyanachari, S. K.; Blomker, T.; Zhang, H. M.; Kehr, G.; Erker, G.; Fuchs, H.; Chi, L. F. *Science* **2011,** 334, 213-216.

170. Wouda, P. T.; Schmid, M.; Nieuwenhuys, B. E.; Varga, P. *Surface Science* **1998,** 417, 292-300.

171. Gonzalez, S.; Neyman, K. M.; Shaikhutdinov, S.; Freund, H. J.; Illas, F. *Journal of Physical Chemistry C* **2007,** 111, 6852-6856.

172. Shu, J.; Bongondo, B. E. W.; Grandjean, B. P. A.; Adnot, A.; Kaliaguine, S. *Surface Science* **1993,** 291, 129-138.

173. Greeley, J.; Mavrikakis, M. *Nature Materials* **2004,** 3, 810-815.

174. Kitchin, J. R.; Reuter, K.; Scheffler, M. *Physical Review B* **2008,** 77, 075437.

175. Svenum, I.-H.; Herron, J. A.; Mavrikakis, M.; Venvik, H. J. *Catalysis Today* **2012,** 193, 111-119.

176. Grabow, L. C.; Gokhale, A. A.; Evans, S. T.; Dumesic, J. A.; Mavrikakis, M. *Journal of Physical Chemistry C* **2008,** 112, 4608-4617.

177. Ojeda, M.; Li, A. W.; Nabar, R.; Nilekar, A. U.; Mavrikakis, M.; Iglesia, E. *Journal of Physical Chemistry C* **2010,** 114, 19761-19770.

178. Ojeda, M.; Nabar, R.; Nilekar, A. U.; Ishikawa, A.; Mavrikakis, M.; Iglesia, E. *Journal of Catalysis* **2010,** 272, 287-297.

179. Markovic, N. M.; Schmidt, T. J.; Stamenkovic, V.; Ross, P. N. *Fuel Cells* **2001,** 1, 105-116.

180. Morozan, A.; Jousselme, B.; Palacin, S. *Energy & Environmental Science* **2011,** 4, 1238-1254.

181. Adzic, R. R.; Zhang, J.; Sasaki, K.; Vukmirovic, M. B.; Shao, M.; Wang, J. X.; Nilekar, A. U.; Mavrikakis, M.; Valerio, J. A.; Uribe, F. *Topics in Catalysis* **2007,** 46, 249-262.

182. Zhang, J.; Mo, Y.; Vukmirovic, M. B.; Klie, R.; Sasaki, K.; Adzic, R. R. *Journal of Physical Chemistry B* **2004,** 108, 10955-10964.

183. Zhang, J.; Vukmirovic, M. B.; Sasaki, K.; Nilekar, A. U.; Mavrikakis, M.; Adzic, R. R. *Journal of the American Chemical Society* **2005,** 127, 12480-12481.

184. Zhang, J.; Vukmirovic, M. B.; Xu, Y.; Mavrikakis, M.; Adzic, R. R. *Angewandte Chemie International Edition* **2005,** 44, 2170-2173.

185. Shao, M. H.; Huang, T.; Liu, P.; Zhang, J.; Sasaki, K.; Vukmirovic, M. B.; Adzic, R. R. *Langmuir* **2006,** 22, 10409-10415.

186. Gong, K.; Vukmirovic, M. B.; Ma, C.; Zhu, Y.; Adzic, R. R. *Journal of Electroanalytical Chemistry* **2011,** 662, 213-218.

187. Koenigsmann, C.; Santulli, A. C.; Gong, K.; Vukmirovic, M. B.; Zhou, W.; Sutter, E.; Wong, S. S.; Adzic, R. R. *Journal of the American Chemical Society* **2011,** 133, 9783-9795.

188. Cai, Y.; Ma, C.; Zhu, Y.; Wang, J. X.; Adzic, R. R. *Langmuir* **2011,** 27, 8540-8547.

189. Stamenkovic, V. R.; Fowler, B.; Mun, B. S.; Wang, G. F.; Ross, P. N.; Lucas, C. A.; Markovic, N. M. *Science* **2007,** 315, 493-497.

190. Strasser, P.; Koh, S.; Anniyev, T.; Greeley, J.; More, K.; Yu, C.; Liu, Z.; Kaya, S.; Nordlund, D.; Ogasawara, H.; Toney, M. F.; Nilsson, A. *Nature Chemistry* **2010,** 2, 454-460.

191. Kibler, L. A.; El-Aziz, A. M.; Hoyer, R.; Kolb, D. M. *Angewandte Chemie International Edition* **2005,** 44, 2080-2084.

192. Greeley, J.; Nørskov, J. K.; Kibler, L. A.; El-Aziz, A. M.; Kolb, D. M. *ChemPhysChem* **2006,** 7, 1032-1035.

193. Sasaki, K.; Wang, J. X.; Naohara, H.; Marinkovic, N.; More, K.; Inada, H.; Adzic, R. R. *Electrochimica Acta* **2010,** 55, 2645-2652.

194. Zhang, J.; Lima, F. H. B.; Shao, M. H.; Sasaki, K.; Wang, J. X.; Hanson, J.; Adzic, R. R. *Journal of Physical Chemistry B* **2005,** 109, 22701-22704.

195. Xing, Y.; Cai, Y.; Vukmirovic, M. B.; Zhou, W.; Karan, H.; Wang, J. X.; Adzic, R. R. *Journal of Physical Chemistry Letters* **2010,** 1, 3238-3242.

196. Sasaki, K.; Kuttiyiel, K. A.; Su, D.; Adzic, R. R. *Electrocatalysis* **2011,** 2, 134-140.

197. Brankovic, S. R.; Wang, J. X.; Adzic, R. R. *Electrochemical and Solid State Letters* **2001,** 4, A217-A220.

198. Brankovic, S. R.; Wang, J. X.; Adzic, R. R. *Surface Science Letters* **2001,** 474, L173-L179.

199. Tylkina, M. A.; Tsyganova, I. A.; Savitskii, E. M. *Russian Journal of Inorganic Chemistry* **1962,** 7, 990-996.

200. Okamoto, H., Massalski, T. B., Ed. ASM International: Ohio, 1990; Vol. 3, pp 2345-2346.

201. Wang, J. X.; Inada, H.; Wu, L. J.; Zhu, Y.; Choi, Y.; Liu, P.; Zhou, W.; Adzic, R. R. *Journal of the American Chemical Society* **2009,** 131, 17298-17302.

202. Sasaki, K.; Naohara, H.; Cai, Y.; Choi, Y. M.; Liu, P.; Vukmirovic, M. B.; Wang, J. X.; Adzic, R. R. *Angewandte Chemie International Edition* **2010,** 49, 8602-8607.

203. Anastasijevic, N. A.; Vesovic, V.; Adzic, R. R. *Journal of Electroanalytical Chemistry* **1987,** 229, 305-316.

204. Nilekar, A. U.; Mavrikakis, M. *Surface Science* **2008,** 602, L89-L94.

205. Nieuwenhuys, B. E. *Advances in Catalysis* **1999,** 44, 259-328.

206. Kobylinski, T. P.; Taylor, B. W. *Journal of Catalysis* **1974,** 33, 376-384.

207. Shustorovich, E.; Bell, A. T. *Surface Science* **1993,** 289, 127-138.

208. Burch, R.; Shestov, A. A.; Sullivan, J. A. *Journal of Catalysis* **1999,** 186, 353-361.

209. Stenger, H. G.; Hepburn, J. S. *Energy & Fuels* **1987,** 1, 412-416.

210. Zhou, S.; Varughese, B.; Eichhorn, B.; Jackson, G.; McIlwrath, K. *Angewandte Chemie International Edition* **2005,** 44, 4539-4543.

211. Kumar, A.; Medhekar, V.; Harold, M. P.; Balakotaiah, V. *Applied Catalysis B-Environmental* **2009,** 90, 642-651.

212. Hirano, H.; Yamada, T.; Tanaka, K. I.; Siera, J.; Cobden, P.; Nieuwenhuys, B. E. *Surface Science* **1992,** 262, 97-112.

213. Monkhorst, H. J.; Pack, J. D. *Physical Review B* **1976,** 13, 5188-5192.

214. Zhu, J. F.; Kinne, M.; Fuhrmann, T.; Denecke, R.; Steinruck, H. P. *Surface Science* **2003,** 529, 384-396.

215. Zeng, Z.-H.; Da Silva, J. L. F.; Deng, H.-Q.; Li, W.-X. *Physical Review B* **2009,** 79, 205413.

216. Ford, D. C.; Xu, Y.; Mavrikakis, M. *Surface Science* **2005,** 587, 159-174.

217. Ge, Q.; King, D. A. *Chemical Physics Letters* **1998,** 285, 15-20.

218. Huang, X.; Mason, S. E. *Surface Science* **2014,** 621, 23-30.

219. Wartnaby, C. E.; Stuck, A.; Yeo, Y. Y.; King, D. A. *Journal of Physical Chemistry* **1996,** 100, 12483-12488.

220. Reuter, K.; Scheffler, M. *Physical Review B* **2002,** 65, 035406.

221. Gorte, R. J.; Schmidt, L. D.; Gland, J. L. *Surface Science* **1981,** 109, 367-380.

222. Campbell, C. T.; Ertl, G.; Segner, J. *Surface Science* **1982,** 115, 309-322.

223. Pirug, G.; Bonzel, H. P. *Journal of Catalysis* **1977,** 50, 64-76.

224. Marina, O. A.; Yentekakis, I. V.; Vayenas, C. G.; Palermo, A.; Lambert, R. M. *Journal of Catalysis* **1997,** 166, 218-228.

225. Ertl, G.; Neumann, M.; Streit, K. M. *Surface Science* **1977,** 64, 393-410.

226. Steckel, J. A.; Eichler, A.; Hafner, J. *Physical Review B* **2003,** 68, 085416.

227. Madon, R. J.; Boudart, M. *Industrial & Engineering Chemistry Fundamentals* **1982,** 21, 438-447.

228. Madon, R. J.; Braden, D.; Kandoi, S.; Nagel, P.; Mavrikakis, M.; Dumesic, J. A. *Journal of Catalysis* **2011,** 281, 1-11.

229. Campbell, C. T. *Topics in Catalysis* **1994,** 1, 353-366.